TÉCNICO LISBOA

Valve manoeuvre and wall shear stress characterization: numerical and experimental analyses

João Paulo Borges Coury Cavaleiro de Ferreira

Thesis to obtain the Master of Science Degree in

Civil Engineering

Supervisors:

Professor Dídia Isabel Cameira Covas

Doctor Nuno Miguel da Conceição Martins

Examination Committee

Chairperson: Professor António Alexandre Trigo Teixeira

Supervisor: Professor Dídia Isabel Cameira Covas

Member of the Committee: Professor Helena Margarida Machado da Silva Ramos

Member of the Committee: Professor Nelson Jorge Gaudêncio Carriço

November 2016

Acknowledgments

First, I would like to express my sincere thanks to both my supervisors - Professor Dídia Covas and Doctor Nuno Martins - for their guidance, support, knowledge and motivation throughout the development of this thesis. A special word of gratitude is given to Professor Dídia Covas for the opportunities in the last two years, which have strongly contributed for my growth.

Gratitude is expressed to João Pedro Caetano for the help on the assembly of the experimental facility as well as to Luís Mendes for the data acquisition system improvement. A special thanks to Eng. Fernando Marques da Silva from Laboratório Nacional de Engenharia Civil (LNEC) for lending the miniCTA equipment. To Ana Quaresma, Daniel Conde, Dora Salgueiro, João Delgado, Laura Monteiro and Pedro Sanches for the fellowship and support during this last stage. To Dulce Fernandes for her kindness and administrative support.

To all my friends of Instituto Superior Técnico for the fellowship and turning all the hardworking hours in the last 5 years as enjoyable as they could. Special thanks to Afonso, Daniela, Joana, João, Marta, Mendes, Nuno and Stefano who I became very fond of.

A special thanks to my friends André, Elisa, Filipa Fernandes, Filipa Ferreira, Inês, João, Mariana, Miguel Carreiro, Miguel Pina and Pedro who were there in the good and bad moments and helped me become who I am.

Above all, I would like to thanks my family for the support and patience at all moments. To my parents, Maria and Paulo who provided for my education and gave me priceless advice. To my brothers, Maria, Luís and Pedro who are irreplaceable and life would not have half the love or half the fun without them.

To my grandparents who inspired me with such different life experiences and made me push myself for trying to get and be my best.

Resumo

A presente investigação tem como objetivo contribuir para a caracterização de dissipação de energia durante a ocorrência de transitórios hidráulicos em sistemas de condutas em pressão. Foi desenvolvido um modelo numérico unidimensional (1D) recorrendo ao Método das Características (MOC). O modelo incorpora as formulações mais relevantes de resistência ao escoamento em regime variável, tendo sido calibrado e validado com base em ensaios realizados num circuito experimental construído no Laboratório de Hidráulica e Ambiente no Departamento de Engenharia Civil, Arquitetura e Georrecursos do Instituto Superior Técnico.

Complementarmente, procedeu-se à caracterização e análise experimental do comportamento estático e dinâmico de uma válvula esférica. Observou-se que os coeficientes de perda de carga da válvula dependem do grau de abertura e do regime de escoamento até atingir o fechamento de 94% (i.e., 85° de ângulo de fechamento). A análise do comportamento dinâmico da válvula permitiu a determinação do tempo efetivo de fechamento, assim como a obtenção da lei de fechamento a implementar no modelo numérico como condição de fronteira de jusante.

Foram efetuadas medições de tensão tangencial na parede interior da conduta recorrendo à tecnologia de anemometria de filme quente a temperatura constante durante a ocorrência de regimes transitórios hidráulicos. Utilizaram-se resultados de um modelo *Computational Fluid Dynamics* (CFD) para a discussão das medições efetuadas.

Palavras-chave: regimes transitórios hidráulicos, modelação 1D, resistência ao escoamento em regime variável, tensão tangencial, válvula esférica, anemometria a temperatura constante.

Abstract

The current research aims at contributing to a better understanding in energy dissipation during hydraulic transients in pressurized pipes. A one-dimensional (1D) numerical model was developed based on the Method of Characteristics (MOC). The model incorporates the most relevant unsteady friction models developed in the past years and was calibrated and validated using experimental data collected from a facility installed at the Laboratory of Hydraulics and Environment, in the Department of Civil Engineering, Architecture and Geo-resources (DECivil) at Instituto Superior Técnico.

The static and dynamic behaviour of the spherical valve located at the downstream end was experimentally characterized to better describe this boundary condition in the numerical model. The valve head loss coefficients vary with the closure and with the flow regime for valve closure until 94% (i.e., 85° closure angle). The characterization of the dynamic valve behaviour allowed to determine the effective closure time of the valve as well as closure curves laws, in order to numerically characterize the valve behaviour during transient events.

Wall shear stress measurements were carried out using hot-film constant temperature anemometry technique during transient events. Results from a Computational Fluid Dynamics (CFD) model contributed to the discussion of the measurement uncertainties.

Keywords: hydraulic transients, 1D modelling, unsteady friction, wall shear stress, spherical valve, constant temperature anemometry.

Table of Contents

List of Figures

List of Tables

Nomenclature

Roman characters

a	Pressure wave celerity	(ms^{-1})
A, B	Probe sensor calibration coefficients	(-)
A_i, B_i	Parameters from formulation	(-)
b	First viscosity layer thickness	(m)
B	Experimentally determined constant	(-)
C^*	Reynolds dependent variable from Vardy and Brown (1995) formulation	(-)
C_d	Valve discharge coefficient	(-)
Cr	Courant number	(-)
D	Pipe inner diameter	(m)
e	Pipe wall thickness	(m)
E	Young modulus of elasticity	(Pa)
f	Darcy-Weisbach friction factor	(-)
f_f	Fanning coefficient given by $f_f = f/4$	(-)
g	Gravity acceleration	(ms^{-2})
h_{fs}	Steady-state unit head loss	(m m^{-1})
H	Piezometric-head	(m)
H_0	Initial piezometric-head	(m)
H_d	Piezometric-head at downstream the valve	(m)
H_R	Reservoir head	(m)
H_u	Piezometric-head at upstream the valve	(m)
k , k_3	Experimental decay coefficient	(-)
k_t, k_x	Experimentally determined local and convective coefficients	(-)
K	Water bulk modulus	(Pa)
K_V	Valve head loss coefficient	(-)
L	Pipe total length	(m)
n	Reynolds dependent variable	(-)
r	Radial distance from the pipe axis	(m)
Q	Flow rate	(m^3s^{-1})
Q_0	Steady-state flow rate	(m^3s^{-1})
R	Pipe inner radius	(m)
R^*	Resistance factor	(-)
R_{20}	Probe resistance at 20°C	(Ω)

R_H	Hydraulic radius	(m)
R_L	Leads resistance	(Ω)
R_{sensor}	Sensor resistance	(Ω)
R_W	Wheatstone bridge resistance	(Ω)
Re	Reynolds number	(-)
Re_0	Steady-state Reynolds number	(-)
S	Inner pipe cross section	(m^2)
S_V	Valve cross section	(m^2)
t	Time coordinate	(s)
t_c	Valve closure time	(s)
t_{ch}	System characteristic time	(s)
t_d	Time decay	(s)
t_{ef}	Effective time of valve closure	(s)
T	Pressure wave period	(s)
T_0	Flow temperature	(^{o}C)
T_{sensor}	Sensor temperature	(^{o}C)
u, v	Local velocities according to the axis coordinates	(ms^{-1})
u', v'	Fluctuating velocities component according to the axis coordinates	(ms^{-1})
u_*	Friction velocity	(ms^{-1})
u^+	Non-dimensional velocity	(-)
$u_{\max}$	Maximum local velocity	(ms^{-1})
U, V	Mean velocities component according to the axis coordinates	(ms^{-1})
V_0	Steady-state flow velocity	(ms^{-1})
W	Weighting function	(-)
w	Integration constant	(-)
x	Spatial coordinate	(m)
y	Distance from the wall	(m)
y^+	Non-dimensional distance	(-)
Y_i	Weighting function coefficient	(-)
Z	Geometric head	(m)

Greek characters

α	Pipe restraint coefficient	(-)
α_{20}	Sensor TCR	(% $^{o}C^{-1}$)
α_v	Kinematic viscosity increase rate per meter	(ms^{-1})
δ^*	Viscous sub-layer thickness	(m)
γ	Water weight per unit volume	(Nm^{-3})
ε	Pipe absolute roughness	(m)
θ	Relaxation coefficient	(-)
μ	Water viscosity	(kg $m^{-1}s^{-1}$)
ν	Water kinematic viscosity	(m^2s^{-1})
ν_c	Flow core kinematic viscosity	(m^2s^{-1})
ν_w	Kinematic viscosity around the wall	(m^2s^{-1})
ν_P	Pipe material Poisson coefficient	(-)
ρ	Water density	(kg m^3)
τ	Shear stress	(Pa)
τ_v	Wall shear stress viscous component	(Pa)
τ_t	Wall shear stress turbulent component	(Pa)
τ_w	Wall shear stress	(Pa)
τ_{ws}	Steady-state wall shear stress component	(Pa)
τ_{wu}	Unsteady-state wall shear stress component	(Pa)
Ψ	Non-dimensional time	(-)

Abbreviations

CCA	Constant current anemometry
CFD	Computational fluid dynamics
CFL	Courant-Friedrich-Lewy
CTA	Constant temperature anemometry
CVA	Constant voltage anemometry
DAS	Data acquisition system
DCCS	Digital configurable current source
DECivil	Departamento de Engenharia Civil, Arquitectura e Georrecursos
FSI	Fluid-structure interaction
HART	Highway Addressable Remote Transducer
IST	Instituto Superior Técnico
LHE	Laboratory of Hydraulics and Environment
MOC	Method of characteristics
SIMPLE	Semi-Implicit Method for Pressure-Linked Equation
SVP	Spherical valve positioner
TCR	Temperature coefficient of resistance

Chapter 1 | Introduction

1.1 Motivation

Late XIX century, the industrial revolution was beginning, urban areas were growing and water demand increasing. Water transport was becoming a major concern as pipe systems provided safe water drinking and sanitation, which are associated to populations well-being (Martins, 2016). With the higher complexity of hydraulic systems, hydraulic transients began to be also a major concern. Thus, transient events generated by valve manoeuvres, hydraulic turbo-machines start-up or stoppage, mechanical failures in surge protection devices or even sudden disruptions in the infrastructure started to be studied (Covas, 2003).

The control equipment of pressurized pipe systems should be carefully designed in order to balance efficiency and safety considering the risk factor. A detailed analysis needs to be carried out for both design and operation purposes, as well as for expected expansions or rehabilitation works. In this context, hydraulic transients should be considered since the preliminary design stages to define pipes fittings, materials, wall thicknesses and pressure classes as well as to define equipment technical specifications and for surge protection, bearing in mind that the solution is under safe, reliable and economic conditions (Ramos *et al.*, 2000).

Nowadays, hydraulic transient events in pipes are commonly analysed using one-dimensional (1D) solvers for daily engineering purposes, since extreme pressures are well predicted (in the safe side) when using these tools. However, an adequate characterization of links (pipes) and node-element (e.g., boundary condition) characterization must be performed. If the nodes and links do not have the correct characteristics, the model will not describe properly the expectable real life events and accidents can occur due to improper design. Thus, the correct pipe system characterization must be defined and validated. Only afterwards can transient models be developed and simulations run. This becomes increasingly more important for the diagnosis of operational problems in existing systems.

Moreover, one of the main differences between hydraulic transient events and the obtained results with 1D models, particularly in metal and concrete pipes (i.e., elastic pipes), is the energy dissipation due to the unsteady wall shear stress. This greatly affects the time which the system takes to restore another equilibrium configuration, as well as the amplitude, phase and shape of the pressure wave. Such issue is particularly relevant since the superposition of extreme pressures could compromise the system safety. A well-managed operation is essential to cover energy, water and economical needs. In order to optimize operation procedures, each case must be independently analysed for the system worst case scenario (i.e., the one that compromises the system the most) and operational rules accordingly defined and/or new safety equipment specified (Ghidaoui and Zhao, 2005).

1.2 Objectives

The current thesis aims to contribute to a better understanding and modelling of hydraulic transient events by using 1D numerical models through an extensive experimental data collection programme and the development of a robust hydraulic transient solver.

The developed experimental analysis has two novel components, comparatively to previous researches carried out at IST. The first is the experimental characterization of the static and dynamic behaviour of the spherical valve (i.e., the valve which generates transient events). Several changes have been introduced in the existing experimental facility at the Laboratory of Hydraulic and Environment (LHE) at Instituto Superior Técnico (IST) and an extensive data collection programme was carried out. The second was the measurement of the wall shear stress at the mid-pipe section in transient conditions using constant temperature anemometry (CTA). The wall shear stress measurements during water hammer events are scarce and, when they exist, these are usually carried out indirectly using a velocity profile approach (Brito *et al.*, 2014). Collected data were used for comparison with numerical results in terms of pressure-head and wall shear stress.

The 1D numerical model improvement also included two features. The first was the incorporation of the closure manoeuvre experimentally determined in the first stage of this research in the numerical model. The second was the implementation of different unsteady friction formulations in the 1D model.

Main obtained results are: i) a complete characterization of the spherical valve behaviour both in static and dynamic conditions; ii) lessons learnt from the unsteady wall shear stress measurements using temperature anemometry; and iii) a better understanding of water hammer events and the physical phenomenon associated with energy dissipation.

1.3 Thesis outline

The current master thesis is composed of seven chapters, a reference list and three appendices.

Chapter 1, the current chapter, introduces the thesis scope, the objectives and the followed methodology in the present research.

Chapter 2 presents an overview of the main contributions to water hammer analysis both in terms of numerical formulations and developments. Flow structure is described and a background is given about the law of the wall. An introduction to wall shear stress measurements is given.

Chapter 3 contains the description of the experimental pipe facility, the characterization of the instrumentation used for data collection and the sets of experimental tests carried out.

Chapter 4 comprises the experimental characterization of the static and dynamic behaviour of the valve. The data collection begins with the static experimental tests in which the discharge and the piezometric-heads at upstream and downstream the valve are measured. Afterwards, the dynamic behaviour is characterized and considerations are made about how the discharge varies through the valve with closure

angle. Computational fluid dynamics model results are compared with the collected data and the influence of the pipe system length on the discharge is discussed.

Chapter 5 presents a description of the implemented numerical model as well as of the basic governing equations that describe transient events in pipes. Numerical schemes used for implementing the unsteady friction formulations are presented. The calibration and validation of the developed numerical model is carried out both by theoretically and experimentally estimating the pressure wave celerity, as well as the decay coefficients for each unsteady friction formulation. Conclusions are drawn about the formulations that most accurately describe the transient phenomenon.

Chapter 6 focuses on the wall shear stress measurement using a constant temperature anemometry technique. The calibration process of the hot-film probe is described and a calibration curve is presented. Collected wall shear stress data are compared with results from each UF formulations. CFD modelling results are used to discuss the collected wall shear stress data and to assess if this measurement technique is adequate for the measurements of this parameter during fast transient events.

Chapter 7 presents the main conclusions of this work and recommendations for future research.

The thesis has three appendices with complementary data: the first includes collected data from the static valve behaviour, the second, data from the dynamic valve behaviour and the third, the collected data from wall shear stress tests.

Chapter 2 | Literature review

2.1 Introduction

The current chapter presents a state-of-the-art review on the research carried out in hydraulic transients, unsteady friction formulations used in 1D solvers and wall shear stress measurement techniques. An overview on the evolution of water hammer theory and friction formulations, divided in instantaneous acceleration-based and convolution-based, is presented. This overview is important not only for the numerical model development, but also to establish the necessary modifications in the existing straight copper pipe rig to meet the thesis goals (i.e., valve characterization, unsteady friction modelling and wall shear stress measurements). The background on wall shear stress and on the respective measurement techniques, including their advantages and drawbacks, is important to support the decision on the most adequate technique for the measurement of this parameter.

2.2 Theoretical background

2.2.1 General remarks

Hydraulic transient events in pressurised pipes occur when a flow disturbance arises in time, generating pressure variation; it is called *water-hammer* by the hammering sound of water that is associated to the event (Parmakian, 1955). A common cause of transient events is the valve closure manoeuvre. When such event occurs in a single pipe system, water compresses, a pressure rise is generated and the pipe expands, creating a pressure wave that travels away from the valve, along the pipe. Once reaching a boundary, the pressure wave inverts the direction decompressing the water and contracting the pipe, until reaching the valve; then, the water continues to decompress, generating a lower pressure wave that travels back. The pressure wave continues to propagate until the total flow energy is dissipated and a new steady-state flow is attained.

A hydraulic transient occurs whenever there is a boundary condition change, for instances, a change in valve settings (closure/opening), a pump start-up, shut-down or trip-off, a turbine when accepting or rejecting load, and sudden ruptures in pipes or fittings. In these cases, safety measures must be undertaken during design stage. If hydraulic transients are not properly addressed, column separation may occur, leading to eventual pipe deformation or pipe bursting. Induced leaks, service disruption and water contamination may also occur if low pressures are registered during a water hammer event.

Regardless of safety concerns during systems' design, water hammer interest has been increasing throughout the years and transient-based techniques have been used for the multiple applications, namely: leak detection and location (Brunone, 1999, Covas and Ramos, 1999, 2001, Ferrante and Brunone, 2003, Covas *et al.*, 2005a, Ferrante *et al.*, 2013); partial or total blockage assessment (Duan *et al.*, 2013, Tuck and Lee, 2013, Massari *et al.*, 2014); pipe system characteristics evolution in time (e.g., incrustation; pipe

aging and loss of stiffness; pipe fissure) (Covas, 2003, Stephens *et al.*, 2013, Tuck and Lee, 2013); and real time condition assessment (Brunone *et al.*, 2013, Lee *et al.*, 2015).

2.2.2 Wave celerity, manoeuvre type and simplified formulations

Pressure wave velocity, or wave celerity, a, created by the simultaneous deformation of the pipe and the compression of the fluid, can be calculated by the following theoretical formulation (Chaudhry, 2014):

$$a = \sqrt{\frac{\frac{K}{\rho}}{1 + \frac{\alpha D}{e}\frac{K}{E}}} \tag{2.1}$$

in which D is the pipe inner diameter, K is the bulk modulus of elasticity of the fluid, ρ is the fluid density, e is the pipe wall thickness, E is the pipe Young's modulus of elasticity and α an empirical coefficient that depends on the axial constraints of the pipe. The wave celerity depends on the fluid and the pipe characteristics, as well as on the constraints along the pipe system. These constraints depend on a series of pipe restrictions, being the most common the axial constraints and the pipe thickness as shown in Table 2.1. The pipe wall is considered thin when $D/e \geq 25$ and thick when $D/e < 25$.

Table 2.1. Celerity coefficient for support pipe conditions (Wylie *et al.*, 1993)

Rigid pipe	$\alpha = 0$
Conduit with frequent expansion joints	$\alpha = D/e$
Thin-walled pipe anchored against longitudinal movement throughout its length	$\alpha = D/e\,(1 - \nu_P)$
Thin-walled pipe anchored against longitudinal movement at upper end	$\alpha = D/e\,(1 - 0.5\nu_P)$
Thick-walled pipe with frequent expansion joints	$\alpha = \frac{2e}{D}(1 + \nu_P) + \frac{D}{D + e}$
Thick wall pipe anchored against longitudinal movement throughout its length	$\alpha = \frac{2e}{D}(1 + \nu_P) + \frac{D(1 - \nu^2{}_P)}{D + e}$
Thick wall pipe anchored against longitudinal movement at upper end	$\alpha = \frac{2e}{D}(1 + \nu_P) + \frac{D}{D + e}\left(1 - \frac{\nu_P}{2}\right)$

where ν_P represents the pipe material Poisson coefficient.

The wave celerity is also affected by the non-linear elastic rheological behaviour of the pipe wall, in which the wave celerity becomes time-dependent (Suo and Wylie, 1990, Covas *et al.*, 2005b) or by the presence of free gas in the liquid in which the celerity depends also on the amount of dissolved gas and on pressure, as shown in Figure 2.1.

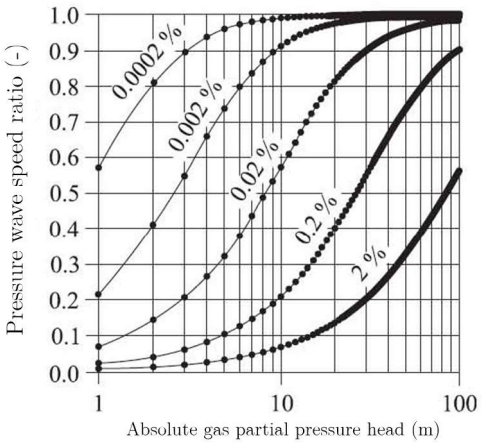

Figure 2.1. Pressure wave celerity ratio with dissolved air percentage with pressure variation (Bergant *et al.*, 2006)

As hydraulic transients are oscillatory events, the pressure wave period, T , is given by:

$$T = \frac{4L}{a} \tag{2.2}$$

in which L is the total length of the pipe.

Formulations to describe extreme transient pressures depend on the duration of the event that generates the transient (e.g., valve manoeuvre). *Slow transients* are the ones generated by a manoeuvre with the time duration higher than the system characteristic time:

$$t_{ch} = \frac{2L}{a} \tag{2.3}$$

Fast transients are generated by manoeuvres with a closure time higher than this value.

Menabrea (1858) was the first to address the estimation of extreme pressure variations. Michaud (1878) studied the effect of air chambers and safety valves to control water hammer events. This researcher proposed formulation to estimate the maximum pressure variation generated by the total closure of a valve without taking into account friction losses, for slow manoeuvres:

$$\Delta H = \pm \frac{2LV_0}{g\, t_{ef}} \tag{2.4}$$

being ΔH the piezometric-head variation, V_0 the steady-state mean velocity (for partial closure, this corresponds to the velocity variation), t_{ef} the effective closure time according to Lescovich (1967) and g the gravitational acceleration.

Several years later, Joukowsky (1900) developed the most commonly used formulation to evaluate the pressure variation in fast transients (for total valve closure), commonly used to easily validate extreme pressures in one-phase flow models.

$$\Delta H = \pm \frac{a V_0}{g} \tag{2.5}$$

Leslie and Tijsseling (2000) developed a formulation to estimate the overpressure taking in account the quasi-steady friction during transient events:

$$\Delta H = \pm a \Delta V_0 \frac{e^{\frac{fV_0 L}{2aD}}}{1 + \frac{(\Delta V)_0}{2V_0}\left[1 - e^{\frac{fV_0 L}{2aD}}\right]} \tag{2.6}$$

in which f is the Darcy-Weisbach friction coefficient further defined in Eq.(2.14). This way, the pressure rise (line packing) due to friction after a transient event is taken in consideration.

2.2.3 Basic equations and assumptions

To determine pressure history with higher detail, a more extensive analysis was carried out by Allievi (1902) that developed the general water hammer theory. This researcher also stated that the convective term of the momentum equation is negligible, since the initial velocity is very small when compared with the pressure wave celerity ($V_0 \ll a$). With his and several other contributions, the steady-state and transient flow in pressurised pipes can be described by the following 1D mass and momentum equations (Chaudhry, 2014):

$$\frac{a^2}{g}\frac{\partial V}{\partial x} + \frac{\partial H}{\partial t} = 0 \tag{2.7}$$

$$\frac{\partial V}{\partial t} + g\frac{\partial H}{\partial x} + \frac{4}{\rho D}\tau_w = 0 \tag{2.8}$$

being x the spatial coordinate, t the time coordinate, H the piezometric-head, V the mean velocity and τ_w the wall shear stress. These equations were developed considering the assumptions presented in Table 2.2.

Table 2.2. Assumptions of water hammer events (Covas, 2003)

Fluid assumptions	
i.	One phase, homogeneous and compressible flow. This compressibility is taken in account in the wave celerity
ii.	Changes in fluid density, temperature, moreover viscosity, are negligible compared with pressure and flow variations during the events
Flow assumptions	
iii.	The flow is one-dimensional with a uniform velocity profile in each cross-section. This leads to unitary momentum and Coriolis coefficients.
iv.	Head-losses during transient events may be calculated as in steady-state by friction formulations. This is not valid for fast transients unless a corrective factor is introduced in the momentum equation
Pipe assumptions	
v.	The pipe has a linear elastic rheological behaviour
vi.	The dynamic fluid-structure is negligible assuming the constraints along the pipe that do not allow axial movement
vii.	The pipe is straight, uniform, with a constant cross section, either with or without flow

2.2.4 Numerical models

Several numerical methods can be used to solve mass and momentum equations, Eqs.(2.7) and (2.8) (Almeida and Koelle, 1992, Chaudhry, 2014). Each numerical method has advantages and drawbacks and depend on the Courant number to ensure the method's convergence and stability, being Cr the Courant number defined by the ratio between the real and the numerical wave celerity (Chaudhry, 2014):

$$Cr = \frac{a}{\frac{\Delta x}{\Delta t}} \tag{2.9}$$

Time (Δt) and space (Δx) steps must be specified in order to verify Courant condition ($Cr \leq 1$), and, preferably, for $Cr = 1$, that is $\Delta x = a\Delta t$, in order to avoid numerical dispersion and dissipation. The most used models are described in the following paragraphs.

Method of characteristics (MOC) | This method is the most widely used approach for modelling one-dimensional transient flows due to the programming simplicity. MOC converts the set of two partial differential equation of mass and momentum equilibrium into two ordinary differential equations, using a finite-differences scheme defined along the characteristic lines. These equations are commonly solved using a rectangular grid, depicted in Figure 2.2. The convergence of the method is guaranteed if Courant-Friedrich-Lewy stability condition is satisfied ($Cr \leq 1$), as in Eq.(2.9). The method independently solves each boundary condition but introduces dispersion and attenuation when interpolations are necessary (i.e., cavitation flows, multiple systems).

Implicit finite-difference | This method solves the equations for the whole system at once and is unconditionally stable regarding the used scheme, as long as Courant-Friedrich-Lewy condition is satisfied ($Cr \leq 1$) (Eq.2.9). This leads to a large number of friction terms once it is non-linear along the hydraulic transient. In addition, if Courant number is not unitary, undesired oscillations may appear (Holloway and Chaudhry, 1985). These limitations made MOC the most used model.

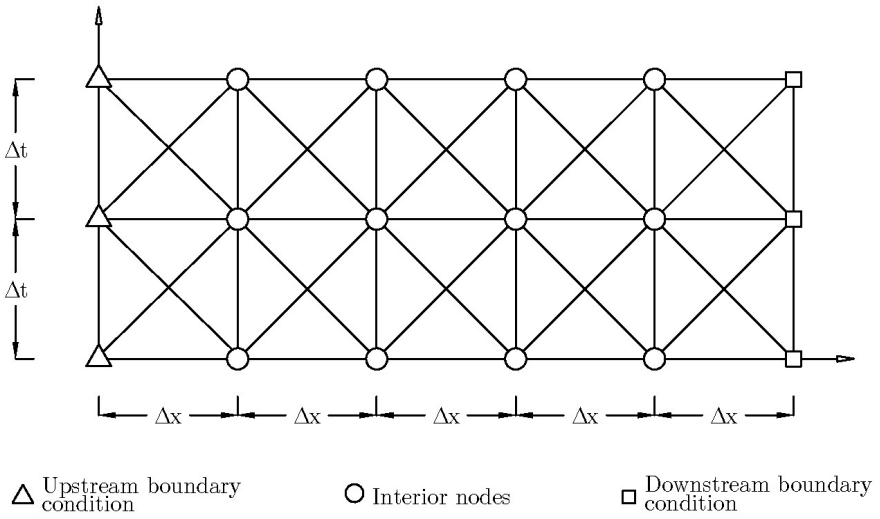

Figure 2.2. Methods of characteristics grid scheme

Several other numerical models can be used to solve the mass and momentum equations, such as finite-difference method and the spectral method. However, none of these offers any advantage over 1D numerical models implemented using MOC.

Computational fluid dynamics (CFD) models are also used to simulate hydraulic transient events. These are commonly used for a more detailed characterization in water column separation (Wang *et al.*, 2016), turbomachinery hydraulic transients (Wu *et al.*, 2015), unsteady friction (Riedelmeier *et al.*, 2014, Martins *et al.*, 2016) and boundary condition behaviour (Yang *et al.*, 2016).

2.2.5 Velocity profiles

In pressurised steady-state flows, flow regimes are determined by Reynolds number, Re. Figure 2.3 depicts different flow regimes, namely: (a) a laminar flow (Re<2000), (b-c) two transitional flows (2000-4000) and (d) a turbulent flows (Re>4000), being possible to observe the difference between the fluctuating velocity components that do not exist in laminar flows, partially exist in transitional flows but become significant in turbulent flows.

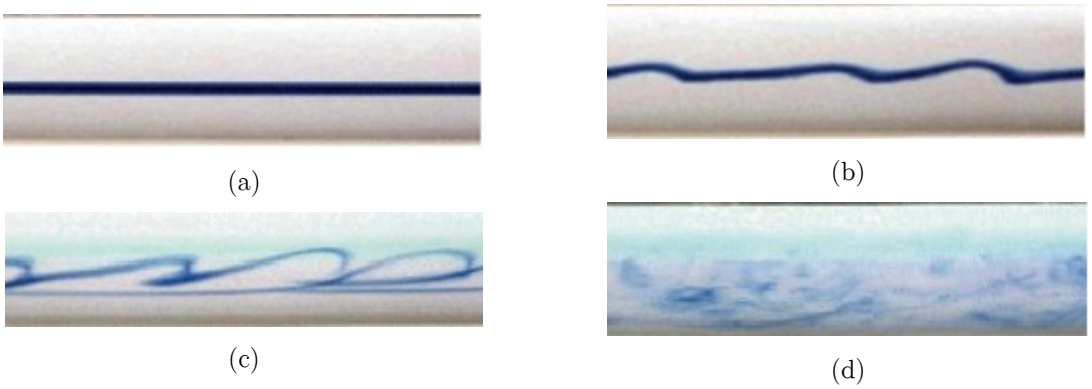

Figure 2.3. Reynolds experiments: (a) laminar, (b) and (c) transitional and (d) turbulent flows (Tsinober, 2009)

For a given flow regime, velocity profiles are reasonably well described in steady-state flow. For laminar flows, the velocity profile takes a parabolic shape described by the Hagen-Poiseuille formulation. However, the assumption of a uniform velocity profile does not remain valid during fast transient events (Bratland, 1986). After a sudden valve closure, the velocity profile changes in time as in Figure 2.4.

In turbulent flows, two main regions may be demarked in the velocity profiles: the *wall region* in which flow changes are faster and with high gradients near the wall, and the *pipe core* that has a higher inertia to changes and has memory of the past time-history of the velocity distribution. These zones behave differently, and answers to different features of the flow: the wall region mostly depends on the viscosity, while the pipe core on fluid inertia. When flow reverses during a water hammer event, a vortex sheet is developed between the core and the reversing flow near the wall (Martins *et al.*, 2016).

As the transient event takes place, until a quarter of the pressure wave period ($t = L / a$), the flow inside the pipe is inverting until it reaches the upstream boundary. Even though the flow later takes the original direction with a similar velocity profile in the core, the initial profile is never attained due to flow diffusion. This velocity profile configuration is the main reason for steady-state formulae not being valid to determine wall shear stress during fast transient events.

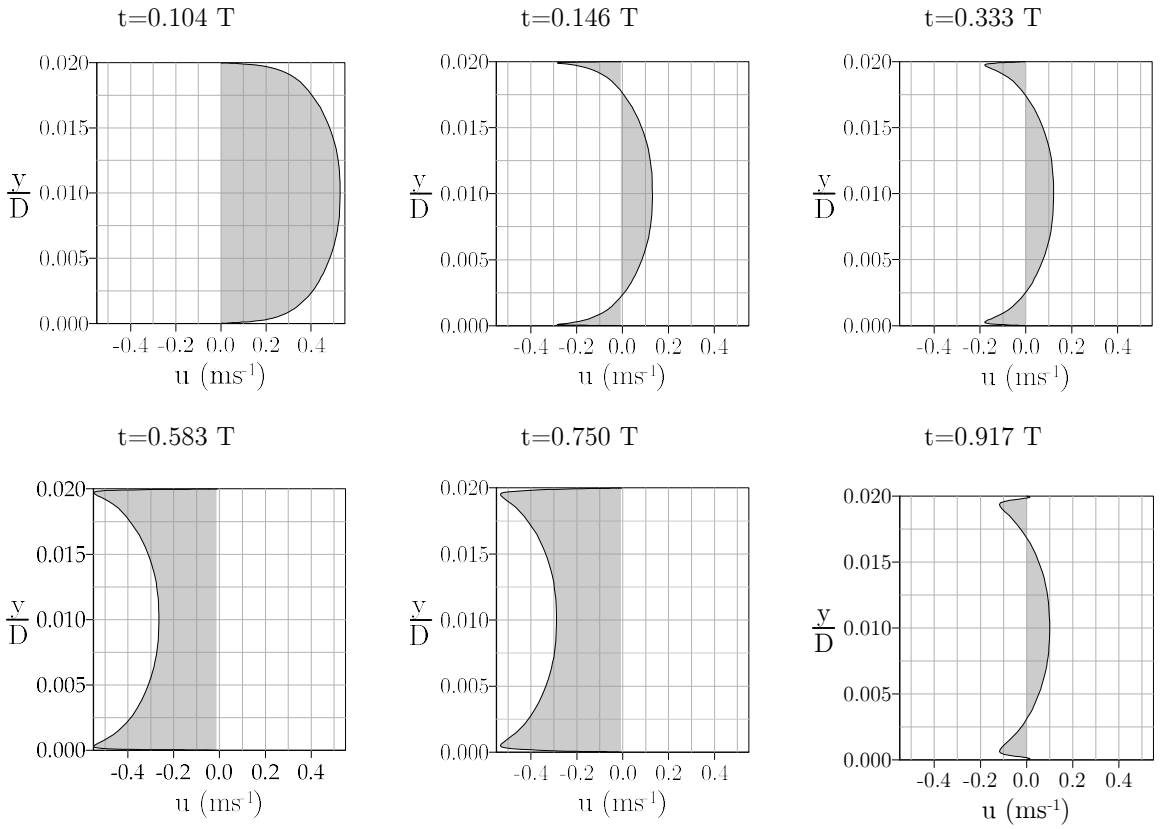

Figure 2.4. Velocity-distribution at the mid-section on the first period of the pressure wave (Martins *et al.*, 2016)

2.3 **Friction losses**

2.3.1 Friction components

The total wall shear stress has two main components, a steady and an unsteady one. That can be treated as independent:

$$\tau_w = \tau_{ws} + \tau_{wu} \tag{2.10}$$

in which τ_{ws} and τ_{wu} are the steady and unsteady components of the wall shear stress, respectively.

Friction losses in steady-state flows are well-described by theoretical or semi-empirical friction formulae both for laminar and turbulent flows, respectively. For unsteady flows, several formulations were developed divided in two of the main common categories – *instantaneous acceleration-based* and *convolution-based*. Both steady and unsteady-state friction formulations are revisited in the following sections. Other contributions presented improvements on the followed methods (Ghidaoui and Mansour, 2002, Vitkovsky *et al.*, 2004, Wahba, 2008), the development of hybrid models (Abreu and Almeida, 2009) or the development of 3D CFD models to simulate hydraulic transients (Martins *et al.*, 2016).

2.3.1 Steady-state formulations

Generically, steady-state friction may be obtained according to Wylie *et al.* (1993):

$$\tau_{ws} = \frac{1}{8} f \rho V \mid V \mid \tag{2.11}$$

The wall shear stress in laminar flows can be obtained by Hagen–Poiseuille formulation:

$$\tau_{ws} = 8 \frac{\mu V}{D} \tag{2.12}$$

in which μ is the fluid viscosity. This formula can be written in a simplified form in terms of the Darcy-Weisbach friction factor and Reynolds number, as $f = 64 / \mathrm{Re}$.

For smooth turbulent flows, Blasius (1913) formulation gives a relation between friction factor and the steady-state Reynolds number, according to:

$$f = 0.3164\,\mathrm{Re}^{-0.25} \tag{2.13}$$

being $\mathrm{Re} = {}^{VD\rho}\!/_{\mu}$ the Reynolds number. This formula is valid for low Re (i.e., $3000<\mathrm{Re}<10^5$).

For rough turbulent flows, Darcy-Weisbach factor can be obtained by Colebrook-White formulation in which the pipe absolute roughness, ε, is considered:

$$\frac{1}{\sqrt{f}} = -2\log\left(\frac{\varepsilon}{3.7D} + \frac{2.51}{\mathrm{Re}\sqrt{f}}\right) \tag{2.14}$$

This formula can be applied in the whole domain of turbulent flows. When used for smooth-wall pipes, null pipe roughness should be considered for achieving more accurate results.

2.3.2 Instantaneous acceleration-based formulations

Daily *et al.* (1956) were the first to propose a formulation based on instantaneous acceleration of the fluid. The researchers carried out experiments and found that the velocity gradient of the flow core, when accelerating, steepened in such a way that the unsteady wall shear stress would be much smaller rather than in decelerating flows. The proposed formulation is given as follows:

$$\tau_{wu} = \frac{k\rho D}{4} \frac{dV}{dt} \tag{2.15}$$

in which k is a coefficient that depends on the flow acceleration or deceleration, taking the values of 0.01 and 0.62, respectively. This led to an academic discussion which was supported with a thermodynamic approach by Axworthy and Ghidaoui (2000). Carstens (1959) derived an equation to determine the unsteady wall shear stress, based on the power law of velocity distribution:

$$\frac{v}{V} = \left(\frac{y}{R}\right)^{\frac{1}{n}} \quad \therefore \quad n = \frac{\left(\sqrt{\frac{v^2}{4V^2} + \frac{2v}{V}}\right)V + \frac{3v}{2}}{2V - 2v} \tag{2.16}$$

in which v is the local velocity in the flow direction, y is the distance to the wall in the radial direction and R is the pipe radius. However, this set of equations only is valid for very slow transient events, when the velocity profile is similar to the steady-state one.

Brunone *et al.* (1991a) developed a different approach to unsteady wall shear stress, taking in account local and convective accelerations. An empirically determined coefficient is used to fit the pressure history during the transient event to numerical results obtained by the proposed formulation. The wall shear stress can be obtained by:

$$\tau_{wu} = k_3 \frac{\rho D}{4}\left(\frac{\partial V}{\partial t} - a\frac{\partial V}{\partial x}\right) \tag{2.17}$$

Bergant *et al.* (2001) proposed an improvement to the previous formulation by taking into account the flow direction. This is particularly relevant when there is a change in an upstream boundary condition. When this is the case, Brunone *et al.* (1991a) formulation Eq.(2.17) gives a pressure rise instead of decay. The proposed wall shear stress formulation is given by:

$$\tau_{wu} = k_3 \frac{\rho D}{4}\left(\frac{\partial V}{\partial t} + a\,\frac{|V|}{V}\left|\frac{\partial V}{\partial x}\right|\right) \tag{2.18}$$

Vardy and Brown (1996) developed a formula to describe the decay coefficient in terms of the Reynolds number, not being necessary to calibrate this parameter based on pressure measurements.

The last improvement in instantaneous acceleration based models is the two coefficient model developed by Ramos *et al.* (2004):

$$\tau_{wu} = \frac{\rho D}{4}\left(k_t \frac{\partial V}{\partial t} + k_x a\ \frac{|V|}{V}\left|\frac{\partial V}{\partial x}\right|\right) \tag{2.19}$$

being k_t and k_x , two decay coefficients. When this formula was applied to high-density polyethylene pipe facility, these researchers have observed that the local acceleration component, $k_t\ \partial V\ /\ \partial t$, changed the phase shift of the pressure wave, whilst the convective acceleration component, $k_x\ \partial V\ /\ \partial x$, had influence on the pressure wave shape.

2.3.3 Convolution-based formulations

Convolution-based models take into consideration both the past accelerations and weighting functions for previous each time steps to estimate the unsteady friction of the flow, as the flow had past velocities "memory".

The first author to introduce such a method was Zielke (1968) with the exact solution (physically based) for laminar flows (Ghidaoui and Zhao, 2005). The author concludes that the pressure gradient is time dependent and the velocity profile does not have the same shape during transient events, and the flow direction in the viscous sub-layer can change earlier than the mean velocity. Such statement is supported by the fact that in the viscous sub-layer, friction prevails and inertial forces are comparatively small. Hence, the velocity is considered in phase with the pressure gradient, while in the flow core where inertial forces prevail and the pressure gradient is in phase not with velocity but with flow acceleration. This convolution formulation is given by:

$$\tau_{wu}(t) = \frac{4\mu}{D}\int_0^t \frac{\partial V}{\partial t}(w)W(t-w)dw \tag{2.20}$$

in which μ is the fluid viscosity and W is the weighting function to determine the weight of each past acceleration. The weighting function is described in terms of a non-dimensional time ($\Psi = 4t\nu \,/\, D^2$) by:

$$\begin{aligned} W(\Psi) &= 0.282095\Psi^{-1/2} - 1.25 + 1.057855\Psi^{1/2} + 0.9375\Psi + 0.396696\Psi^{3/2} - 0.351563\Psi^2 \\ W(\Psi) &= e^{(-26.3744\Psi)} + e^{(-70.8493\Psi)} + e^{(-135.0198\Psi)} + e^{(-218.9216\Psi)} + e^{(-322.5544\Psi)} \end{aligned} \tag{2.21}$$

for $\Psi < 0.02$ and $\Psi > 0.02$, respectively. Herein, ν represents kinematic viscosity ($\nu = \mu \,/\, \rho$) and t the time since the water hammer event started.

Despite the good fit with Holmboe and Rouleau (1967) experimental data, Zielke's solution requires a very large amount of memory and computational time because every time-step must be stored for the following time steps. That has triggered the development of a computationally less demanding method, such as, the one proposed by Trikha (1975):

$$\tau_{wu} = \frac{4\mu}{D}(Y_1 + Y_2 + Y_3) \tag{2.22}$$

where Y_i term can be calculated by

$$Y_i(t) = Y_i(t-\Delta t)\; e^{-n_i \frac{4\nu}{D^2}\Delta t} + m_i\,[V(t) - V(t-\Delta t)] \tag{2.23}$$

in which $n_1 = 8000$, $n_2 = 800$, $n_3 = 26.4$, $m_1 = 40$, $m_2 = 8.1$ and $m_3 = 1$.

Using this formulation, a good fit was obtained with experimental data from Holmboe and Rouleau (1967). Nevertheless, this approach does not agree well when compared with Zielke's using very small time-steps, as it considers only the last three time-steps.

Furthermore, Kagawa *et al.* (1983) followed the same approach but with several others exponential terms. The larger the number of exponential terms (k number) taken into account are, the better the obtained fit compared with Zielke's formulation is. Kagawa's weighting functions are depicted in Figure 2.5.

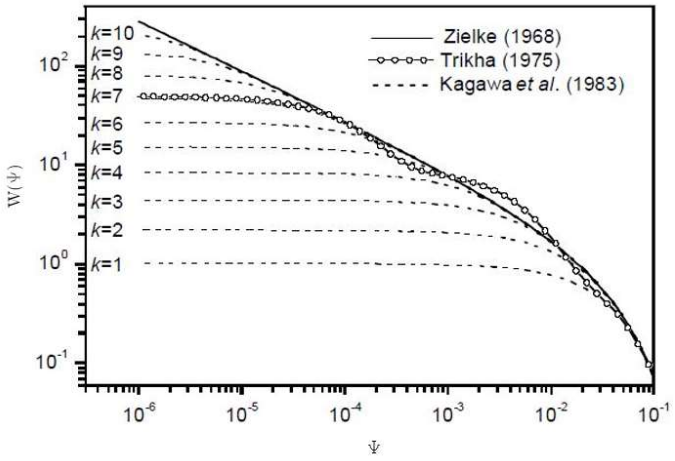

Figure 2.5. Zielke's, Trikha's and Kagawa's weighting functions (Vitkovsky *et al.*, 2004)

Suzuki *et al.* (1991) took Zielke's physical approach and simplified the model in order to reduce the simulation time. Nevertheless, being lesser demanding than the exact solution, the model is more precise than Trikha's solution.

Further on, Vardy *et al.* (1993) developed a friction formulation based on a series of weighing functions for smooth turbulent flows, using Trikha's approach but only considering two exponential terms:

$$\tau_{wu} = \frac{4\mu}{D}(Y_1 + Y_2) \tag{2.24}$$

in which

$$Y_i(t) = Y_i(t - \Delta t)e^{-B_i \frac{4\nu}{D^2} dt} + A_i \left[V(t) - V(t - \Delta t) \right] \tag{2.25}$$

Coefficients A_i and B_i are according Figure 2.6, taking in account that the friction factor used to determine the curve to adopt should be one fourth of the Darcy factor, due to the Fanning's coefficient ($f_f = f \,/\, 4$). These weighting functions have Zielke's as an upper bound.

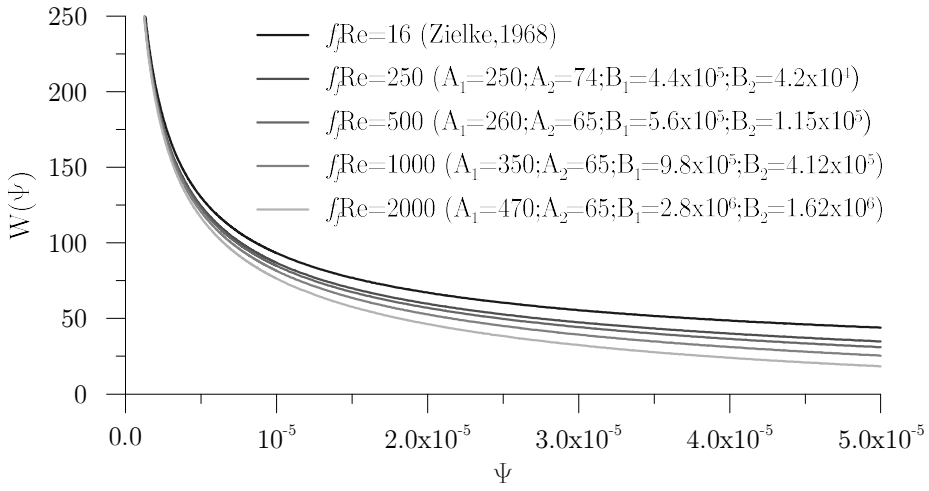

Figure 2.6. Zielke (1968) and Vardy *et al.* (1993) weighting functions

Later, Vardy and Brown (1995) developed a generic version of these weighting functions. Both Vardy *et al.* (1993) and Vardy and Brown (1995) consider a two-layer flow and state that the viscosity does not change for the event duration, considering a "frozen-viscosity". The first layer is considered to be around the pipe wall as an annular layer with a thickness $b = 0.2R$, in which the flow is considered laminar. The second layer (the core) occupies the remaining radius, in which the flow is considered turbulent.

For the described model, the kinematic viscosity distribution is:

$$\begin{cases} annulus : \nu = \nu_w(1 + \alpha_\nu y) \\ core : \nu = \nu_c \end{cases} \tag{2.26}$$

being ν_w the fluid viscosity around the wall, ν_c the fluid viscosity in the flow core, α_ν the viscosity increase rate and y the distance to the wall. Thus, the viscosity increases linearly from the wall to the flow core, where becomes constant and equal to $\nu_c = 0.065 u_* R$, in which friction velocity in the wall can be defined by:

$$u_* = \sqrt{\tau_{ws} / \rho} \tag{2.27}$$

Finally, the weighting function is described as:

$$W = \frac{\sqrt{(\nu_w \ / \ \nu_{lam})}\, e^{\left(-\Psi / C^*\right)}}{2\sqrt{\pi \Psi}} \tag{2.28}$$

in which ν_{lam} is the viscosity associated to laminar flow, Ψ is the non-dimensional time previously defined and is a Reynolds dependent variable given by:

$$C^* = \frac{12.86}{\mathrm{Re}^{\ \kappa}} \quad \text{in which} \quad \kappa = \log_{10}\left(\frac{15.29}{\mathrm{Re}^{\ 0.0567}}\right) \tag{2.29}$$

and for laminar flows has the constant value of 0.00476. With obtained Vardy and Brown (1996), the Reynolds number dependent decay coefficient is described by:

$$k_3 = \frac{\sqrt{C^*}}{2} \tag{2.30}$$

Having already the assumption of a laminar flow annulus surrounding a the turbulent uniform core, this formulation gives a good agreement with Holmboe and Rouleau (1967) for turbulent flows.

These contributions on smooth wall unsteady friction were further on improved with a three zone viscosity distribution Vardy and Brown (2003) as well as a contribution for rough turbulent flows Vardy and Brown (2004). The last contribution on this topic was Zarzycki *et al.* (2011), who has developed a four layer viscosity distribution inside the flow.

2.4 **Wall shear stress**

2.4.1 Theoretical formulations

To fully understand how shear stress varies within flow boundaries, relevant notions about the flow behaviour in each layer are introduced herein. In turbulent steady-state flow, three main layers can be distinguished in fluid motion:

- *Viscous sub-layer*, in which velocity is comparatively small to the mean velocity and viscous forces are predominant. Velocity distribution is linear until the buffer layer.
- *Buffer layer*, where both inertial and viscous forces have a relevant importance. However, velocity distribution is not as well quantified as in the viscous sub-layer.
- *Turbulent layer*, in which mainly inertial forces are relevant and viscous forces are negligible. Velocity distribution can be described by a power or a logarithmic law.

In order to define each layer's boundaries, friction velocity is usually considered Thus, dimensionless distance to the wall can be represented by $y^+ = yu_* / \nu$ and $u^+ = u / u_*$ is the dimensionless local velocity.

The viscous sub-layer is represented by y^+ values smaller than 5, the buffer layer for values understood between $5 < y^+ < 30$ and the turbulent layer comprehended for values $y^+ > 30$. Thus, shear stress can be estimated in any point of the flow knowing the fluid and flow properties (Schlichting, 1979, Martins *et al.*, 2014).

Figure 2.7 presents each layer in dimensionless axis with data obtained by Klewicki and Falco (2006) with hot-wire anemometry for different Reynolds number in an open channel steady flow.

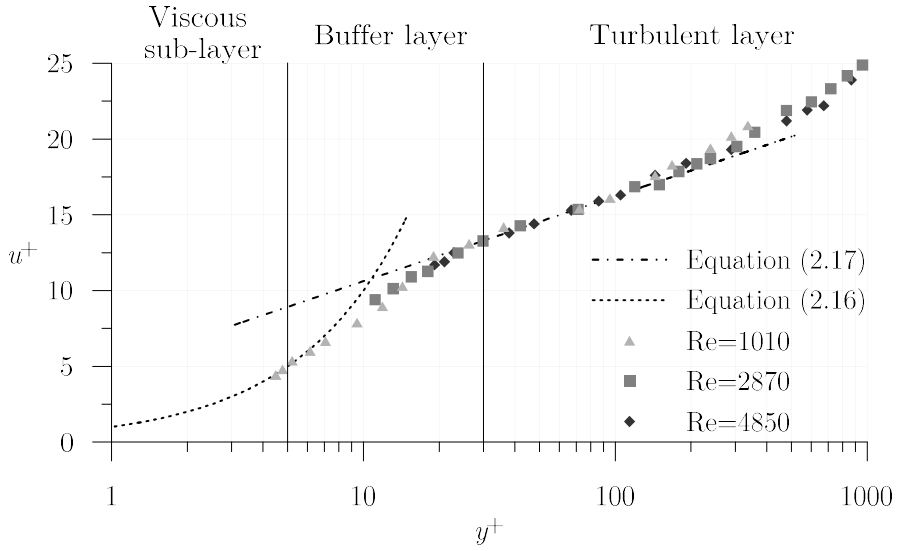

Figure 2.7. Law of the wall (adapted from Klewicky and Falco, 2006)

Inside the viscous sub-layer the velocity has a linear relation with the distance to the pipe wall, given by:

$$u^+ = y^+ \tag{2.31}$$

Accordingly to the power law, for the turbulent layer can be used to determine the local velocity u:

$$\frac{u}{u_{max}} = \left(\frac{y}{R}\right)^{1/n} \qquad \therefore \qquad \frac{u}{u_{max}} = \left(1 - \frac{r}{R}\right)^{1/n} \tag{2.32}$$

in which u_{max} is the maximum local velocity (in the pipe axis), r is the distance from the pipe axis and n is a Reynolds number dependent constant (Schlichting, 1979) that can be obtained by:

$$\frac{V}{u_{max}} = \frac{2n^2}{(n+1)(2n+1)} \tag{2.33}$$

In order to correctly describe the wall shear stress, two components of the flow must be considered: viscous and turbulent. For a turbulent flow, in which both components are relevant, the shear stress can be obtained by:

$$\tau = -\mu \frac{\partial V}{\partial r} + \rho \overline{u'v'} \tag{2.34}$$

being μ is the fluid viscosity and $\overline{u'v'}$ is the mean variation of the radial and axial velocity turbulent components.

2.4.2 Wall shear stress measurements

Several measurements have been carried out in several areas, such as, aerodynamics, hydraulics (both in pipes or rivers), and hemodynamics. In hydraulic transient events, contributions from Shuy (1996), Ariyaratne *et al.* (2010) and He *et al.* (2011) deal with accelerating and decelerating flows. Both Brunone

and Berni (2010) and Brito *et al.* (2014) deal with water hammer events using ultrasonic or optical techniques. Each of these fields has certain characteristics in what concerns the measurements and the used equipment.

The first classification divides flows in supersonic (higher flow velocity than sound velocity) and subsonic flows (lower flow velocity than sound velocity). Since the maximum of wave celerity in water for rigid pipes is 1450 ms^{-1}, corresponding to the speed of sound in water, supersonic flows do not occur in hydraulics transients in pressured water pipes.

Shear measurements may be carried directly or indirectly. Direct measurements correspond to the measurement of the total amount of viscous drag force experienced by a surface-mounted force balance (Berca, 2007). Indirect measurements are obtained through other physical or mechanical processes associated with the wall shear stress (e.g., unit energy dissipation in pipe for steady flow), as explained in the following paragraphs.

The most usual devices for the direct measurements are the floating elements technique and the oil-film interferometry. Floating elements technique is based on the force applied by the flow on a plate that is connected to springs which deform accordingly to the shear force (Figure 2.8). These devices can cover a wide range of surfaces and have proven to be quite accurate on their measurements. However, these can only be used for considerable shears, as the springs may not have enough precision, or would require a large area to be accurate, which would compromise pointwise measurements. Thus, high sensibility and bandwidth cannot be simultaneously achieved.

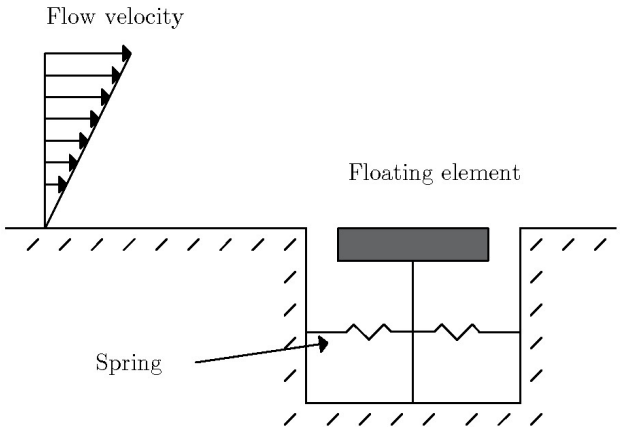

Figure 2.8. Floating element example (adapted from Berca, 2007)

Oil-film interferometry relies on flow visualization in order to quantify shear stress. This method is applied either in free-surface (Tanner, 1979), or in one or two-phase pipe flows (Garrison *et al.*, 1998). The oil layer is spread as thinly as possible and shear is obtained through the oil movement, visible with monochromatic light. Regardless the method advantages, oils viscosity is a major concern as well as the time involved in measurements. Usually, this technique takes from one to two minutes to reach steady-state equilibrium and measures should be taken from 10 minutes to 3 hours.

Wall shear stress indirect measurements are obtained through physical parameters, like pressure and heat transference that can be related with shear stress. Focusing on temperature and heat-transferring processes, hot-wire and hot-films are the most widely used technologies to measure the wall shear stress both in air and water flows. Three different techniques may be used (Tropea *et al.*, 2007):

- Constant current anemometry (CCA) – Keeping current constant, the filter's response is tuned with the sensor and compensates the sensor's thermal lag.
- Constant voltage anemometry (CVA) – By maintaining voltage constant, temperature and current change during the events. Thus, the compensation is only partial on the spot, requiring further post processing for correct measurements. By not having an intrinsic processing, a higher productivity is obtained thanks to a larger bandwidth in comparison to the other measurement techniques.
- Constant temperature anemometry (CTA) – Current and voltage change during measurements time allow the sensor's temperature to remain constant thanks to a feedback loop. If the thermal inertia is negligible, the process can be considered as compensated once the heat transfer is immediate.

Hot-wire equipment was formerly introduced by Bradshaw and Gregory (1959) and became extensively used for a wide speed ranges and the capacity to detect turbulence with a large dynamic response. Nevertheless, for reverse flows, the probe wires and supports create disturbances in the flow. Thus, for pulsating or reverse flows, hot-films are advantageous, as these do not interfere with the flow structure; additionally, hot-film anemometry is usually used thanks to a more rigid construction and to being less likely to be contaminated (Tropea *et al.*, 2007).

2.5 Main gaps and research motivation

Considering all the above developments, two main gaps of knowledge are identified and triggered the development of the current research. The first is the lack of a widely accepted universal unsteady friction formulation for turbulent flows. The second is the inexistence of wall shear stress measurements in water hammer events, even though some studies exist on wall shear stress measurement in accelerating or deaccelerating phases. This thesis aims at the implementation of the main unsteady friction formulations during water hammer events and their comparison with experimental data, discussing the advantages and drawbacks of each formulation. Wall shear stress tests in water hammer events are also carried out and compared with the former friction formulations.

Chapter 3 | Experimental programme

3.1 Introduction

Water hammer measurements have been carried out to validate the developed hydraulic transient models. For that purpose, an existing experimental facility at Laboratory of Hydraulics and Environment (LHE), in the Department of Civil Engineering, Architecture and Geo-resources (DECivil) at Instituto Superior Técnico (IST), has been used and adapted for carrying out the necessary measurements to meet the objectives of the thesis (Ferràs *et al.*, 2016, Martins *et al.*, 2016). The experimental facility, the instrumentation used to measure discharge, pressure-head and wall shear stress and the set of tests that have been carried out are described in the current chapter.

3.2 Experimental facility's description

The facility, schematized in Figure 3.1, consists of a copper pipe with 15.02 m of length, an inner pipe diameter of 0.02 m and a wall thickness of 1 mm (Figure 3.2a). The pipe is fixed in metal supports, 0.60 m equally spaced, to guarantee the constant pipe slope and to minimize fluid-structure interaction (i.e., pipe-structure movement and vibration) (Figure 3.2b).

At pipe upstream end, a centrifugal pump with nominal flow rate of 3.6 m^3h^{-1} and a maximum head of 46 m is fed by a 0.1 m^3 tank (Figure 3.2c), the pump has a membrane check valve, and at downstream supplies the pipe system (Figure 3.2d).

In order to ensure the system safety and to stabilize the upstream pressure, a 60 ℓ stainless steel hydropneumatic vessel is installed immediately after the pump, as shown in Figure 3.2e). The hydropneumatic vessel can operate both in by-pass and in derivation (Figure 3.2f). Operating in by-pass, the vessel behaves as a constant head reservoir. When operating in derivation (as used in this research work), this device works merely as a pressure stabilizer and a safety device during transient events.

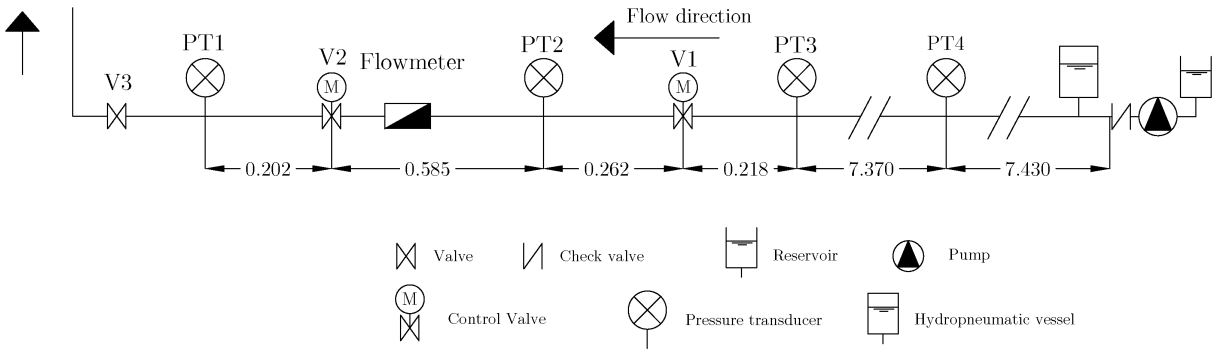

Figure 3.1. Simplified schematic and view of the straight copper pipe set-up

(a) (b) (c)

(d) (e) (f)

Figure 3.2. Experimental facility components: a) copper pipe; b) pipe metal supports; c) water supply tank; d) pump and needle check valve; e) hydropneumatic vessel; f) operation modes (yellow – derivation; red – by-pass).

At the pipe downstream end, a set of valves (Figure 3.3a) has been assembled to simultaneously control the flow and to generate the transient events. This set of valves is composed of (from upstream to downstream):

- Valve V1: a 3/4" pneumatically actuated spherical valve, used to generate the water-hammer events (Figure 3.3b);
- Valve V2: a 3/4" position controlled spherical valve and its positioner (Figure 3.3c,d) ;
- Valve V3: a 3/4" manual spherical valve, used to control the steady-state flow rate (Figure 3.3e).

Figure 3.3. Set of valves: a) valve configuration (V1 and V2), b) pneumatically actuated solenoid valve V1, c) position controlled valve V2, d) positioner of the valve, and e) manual flow control spherical valve V3

The **solenoid spherical valve** (V1), depicted in Figure 3.3b), is operated when a current variation is created from the data acquisition system. When the valve is activated, the compressed air enters in the valve controller system and turns the piston axis, which rotates the valve body until its full closure.

The **position controlled spherical valve** (V2) has a **spherical valve positioner** (SVP) attached to the valve controller. The SVP allows the valve to be partially closed and gives feedback position. The SVP comprises: a) a microprocessor that executes the sent signals and sends indication for valve movement; b) a Highway Addressable Remote Transducer (HART) modem (interface with the user) and LCD (display of the closure angle) and c) a potentiometer to give the position feedback and gauge blocks (required input is a 4-20 mA).

A **digital configurable current source** (DCCS), depicted in Figure 3.4, is necessary to provide the SVP with a certain current for the positioner to move. For that purpose, DCCS provides the positioner with a current between the allowances with a step of 0.03 mA, resulting in 500 points. In order to reduce errors (e.g., electric noise), the device has an internal self-calibration due to electronic own tolerances and temperature coefficients. To define the provided current to the SVP, a RS-232 cable is connected to a laptop where a current intensity is chosen. DCCS is connected to the SVP with a shielded cable for noise reduction and electrical interference minimization.

Figure 3.4. Digital configurable current source device

An oscilloscope is directly connected to the SVP providing the precise closure angle, which is not accurately displayed in the SVP's LCD. A converser is needed to transform the SVP output signal from current to tension. In a range of 0-10 V, the signal is converted in degrees of opening, being 0 V totally open and 10 V totally closed.

3.3 Measurement and control instrumentation

3.3.1 Data acquisition system

The data acquisition system (DAS) is composed of a *PicoScope* oscilloscope, a constant temperature anemometry *Dantec 54T30* MiniCTA device, a trigger synchronizer, a power source for the valve solenoid actuator, and a desktop computer. Figure 3.5 shows the used equipment except the MiniCTA device. These devices either receive data or control four strain-gauge type pressure transducers and a hot-film sensor. An electromagnetic flowmeter is also part of the DAS. Having its own transmitter and display, this device is not connected to the remaining system.

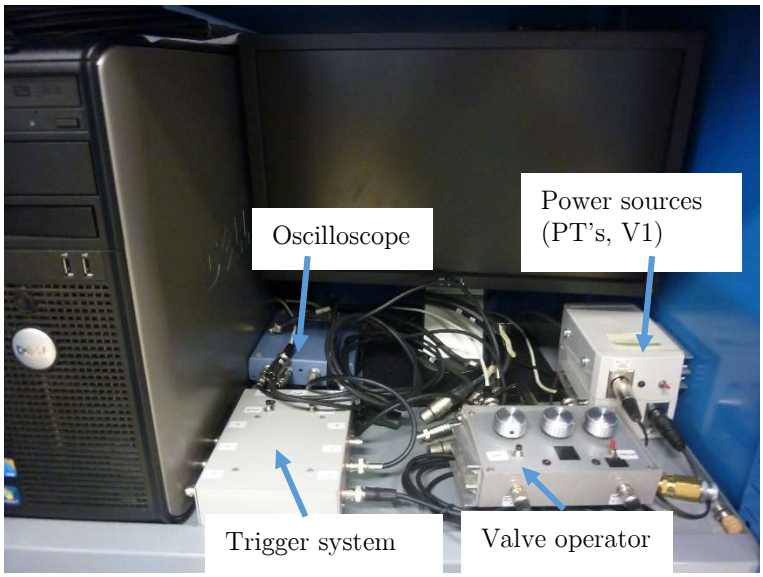

Figure 3.5. Control and reading equipment for measuring devices

Pressure transducers are connected to a power source, that is connect to the *Picoscope6* oscilloscope which transmits the signal to the computer. The MiniCTA is directly connect to the *Picoscope6*.

To obtain from the hot-film probe, a *DANTEC* constant temperature anemometer 54T30 (MiniCTA) is used, as depicted in Figure 3.6.

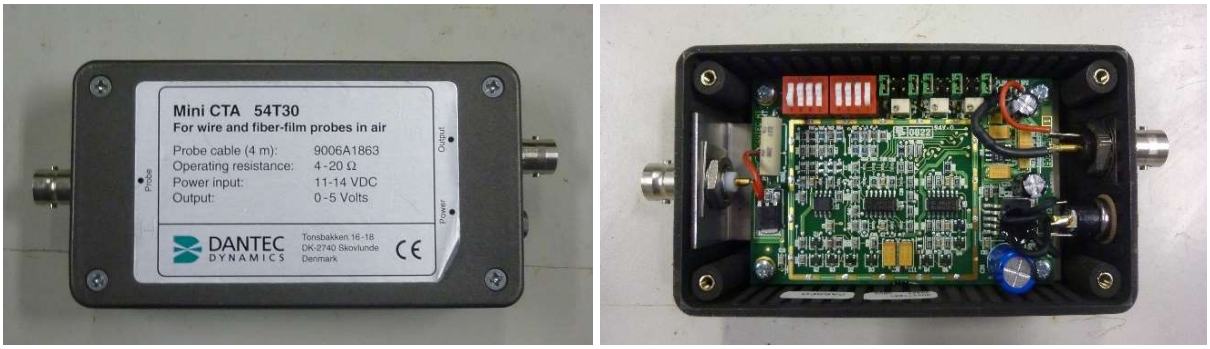

Figure 3.6. 54T30 MiniCTA and electric configuration

The MiniCTA must be configured as instructed by the manufacturer. The device collects the temperature of the glue-on probe in loop and provides it with such a current that the resistance temperature is the same as the desired one. Thus, the output signal is between 0 and 5 V according to the current provided to the sensor. MiniCTA acquisition frequency varies from 1 to 10 kHz.

The used resistance to configure the MiniCTA device can be obtained from the following equation

$$R_W = R_{Total} + \alpha_{20} R_{20} (T_{sensor} - T_0) \tag{3.1}$$

in which R_W is the Wheatstone bridge resistance to even the system, R_{Total} the resistance of the circuit itself α_{20} is the temperature coefficient of resistance at 20°C (TCR), R_{20} the sensor resistance at 20°C, T_{sensor} the sensor desired temperature and T_0 the flow temperature.

The trigger system synchronizes the set of measurement instruments by sending a 5 V variation. A set of commands are defined in order to change the status of the ports and to introduce delays between operations. It has a maximum number of programmable operations of 64, independently of the number of used ports. The power inlet should be 12 to 24 V and the outlet should not exceed 5 V.

When the trigger system identifies a tension variation, the system starts to record data with a pre-defined time and frequency and the pneumatically actuated valve is operated according to the given commands. Thus, each measured parameter (pressure, valve position, shear stress) corresponds to the same time with a maximum delay of 10 ms.

The schematic representation of the DAS connections are depicted in Figure 3.7.

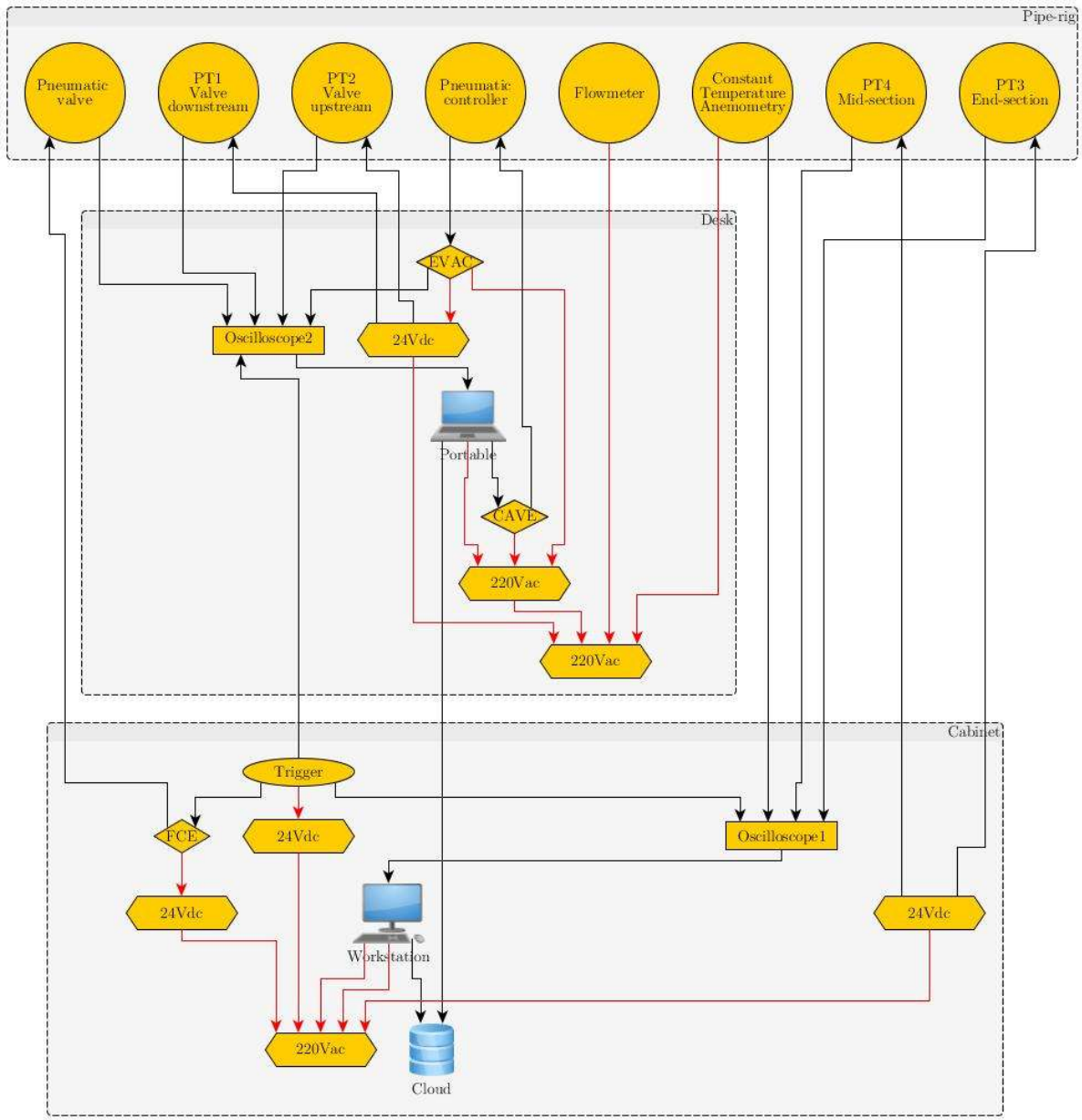

Figure 3.7. Data acquisition system (DAS) overview (red - power; black – information)

3.3.2 Electromagnetic flowmeter

An electromagnetic induction flowmeter is installed in line with the flow to measure the steady-state discharge. The *Siemens MAG 1100* flowmeter, with a stainless steel body, has an inner diameter slightly smaller than the pipe's (20 mm) and the nominal pressure is 40 bar (Figure 3.8). A *Siemens MAG 5000* transmitter is attached to the flowmeter, allowing both the connection with DAS and the display of the measure discharge values. The flowmeter accuracy is 0.4% of the measured discharge. Low flow cut-off occurs at discharges lower than 15 lh^{-1}.

Figure 3.8. Flow meter and transmitter

3.3.3 Pressure transducers

Four pressure transducers (PT1 to PT4) are installed in the pipe system (see Figure 3.1) to carry out the experimental tests both in steady and unsteady conditions. The transducers are connected to the pipe with tee junctions, as depicted in Figure 3.9. Transducers (*WYKA S-10*) have an accuracy of 0.25% of span and work for a nominal pressure of 25 bar, which leads to an absolute error of 0.31 m. The transducers send a 10 V signal to the data acquisition system.

Figure 3.9. WIKA S-10 pressure transducer

Two pressure transducers are used in the experimental tests to characterize the valve static behaviour: PT1 and PT2, located at 1.049 and 0.262 m downstream valve V1, respectively. The pressure transducers used to characterize the dynamic behaviour of the spherical valve: PT2, and PT3, located 0.218 m at upstream the pneumatically actuated valve. The transducers used for the transient events are: PT3, and PT4, located at pipe mid-length (7.37 m upstream the pneumatically actuated valve).

3.3.4 Hot-film probe

The hot-film probe was installed in the pipe-system with cyano-acrylate glue in an especially designed/assembled stainless steel box, with the same inner diameter as the copper pipe, in order to measure the shear stress within the viscous sub-layer (Figure 3.10). The steel box was designed with an indent to place the hot-film probe. This hollow depth was defined taking in consideration the necessary glue and the probe thickness, after several tests.

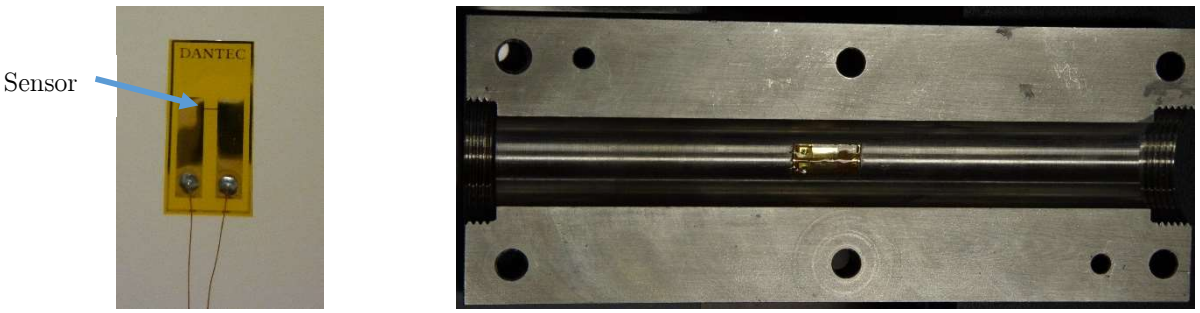

(a) (b)

Figure 3.10. (a) Hot-film probe. (b) Inside view of the stainless steel box

This type of glue-on probe, recommended for 1D flows measurements, is used for low and medium velocities. The probe is also protected to avoid electrolysis and oxidation. The hot-film was used rather than a hot-wire probe because the latter is an intrusive probe, interfering with the flow field during the flow reversal. The used sensor characteristics are presented in Table 3.1. These parameters, characteristic of each probe and provided by the manufacture, are used to determine the maximum resistance of the circuit in order to calibrate the sensor. The sensor temperature must be kept below 60°C in order to avoid micro-fractures in quartz layer and that there are no bubbles around the probe from the heating process.

Table 3.1. Hot-film characteristics

Parameter	Value
Dimensions (mm)	0.9 × 0.1×0.05
Resistance at 20°C (R_{20})	10.89 Ω
Leads resistance (R_L)	0.20 Ω
Sensor TCR (α_{20})	0.3 % / °C

3.4 Experimental tests

3.4.1 Sets of tests

In the scope of the current research, four sets of experimental tests have been carried out:

1) Static tests for valve behaviour characterization.
2) Dynamic tests for valve behaviour characterization.
3) Dynamic tests for numerical model calibration and validation.
4) Dynamic tests for the wall shear stress analysis.

These tests are described in the following paragraphs. Each of them required independent measurements due to physical constraints, as the oscilloscope has a maximum of four ports.

3.4.2 Static tests for valve behaviour characterization

The first set of tests – Static tests for valve behaviour characterization – is carried out with different steady-state initial flow rates, Q_0, controlled with valve V3 (the manual valve), in order to determine the variation of the flow rate and the head loss coefficients with the valve V2 closure angle. Measured parameters are the flow rate and the pressure head at PT1 (downstream) and PT2 (upstream). The flow rate is expected to change with the initial conditions but not the head loss coefficients which are intrinsic characteristics of the valve geometry and size. These tests are carried out for the flow rates presented in Table 3.2: two correspond to turbulent flows, one to transitional flow and one to laminar (according to Reynolds number).

Table 3.2. Static valve tests (S1-S4)

Test	Q_0 (lh^{-1})	V_0 (ms^{-1})	Re
S1	450	0.40	7957
S2	400	0.35	7073
S3	200	0.18	3536
S4	56.5	0.05	999

During these tests, the valve V2 rotation angle is changed in a step-wise manner and controlled by DCCS. A more discretized step is specified in the last 33% of closure to attain a better description of the valve characteristics. For each rotation angle, the flow rate and the pressures upstream and downstream the valve are simultaneously measured by using the DAS.

The variation of the flow rate and of pressure heads at upstream and downstream of the valve with closure angle, for the initial flow rate of 450 lh^{-1}, is depicted in Figure 3.11. As the valve body rotates, the flow rate and the pressure remain almost constant until a 66% closure is reached. From that moment onwards, pressure downstream the valve and flow rate significantly decrease and pressure upstream behaves

according to the pump curve (i.e., if the flow rate decreases, the head increases within the same velocity rotation). Measurements from the remaining tests are presented in Appendix A.

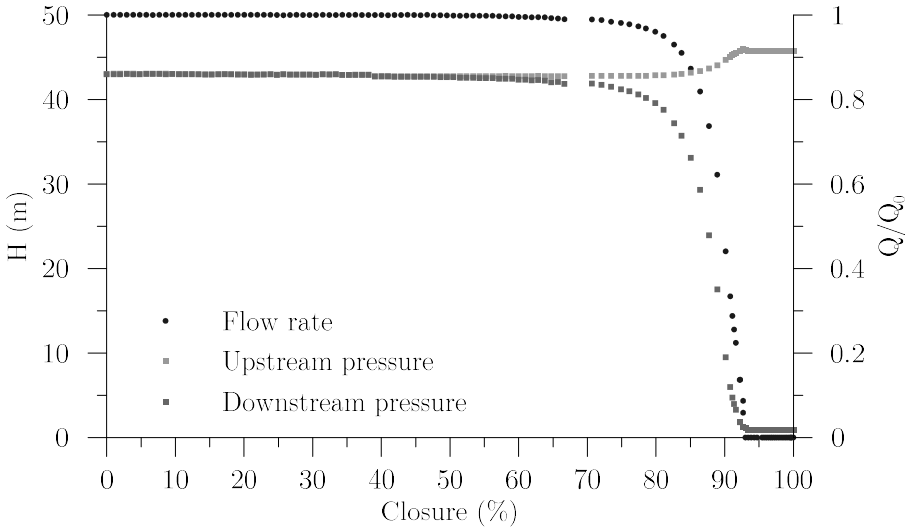

Figure 3.11. Measured flow rate, upstream and downstream pressure for Q_0= 400 lh^{-1} (Test S1)

3.4.3 Dynamic tests for valve behaviour characterization

The second set of tests – Dynamic tests for valve behaviour characterization – is carried out for the same initial flow conditions as the static tests. Collected data are transient pressure heads at PT2 (downstream) and PT3 (upstream) and initial flow rate, Q_0. To assess the closure time effect in the valve behaviour, the spherical valve is subjected to different closure times for different flow rates. The closure time is controlled by the operating air pressure in the solenoid that is connected to the spherical valve. As operating air pressure reduces, the valve piston torque force decreases. The carried out tests are presented in Table 3.3.

Table 3.3. Dynamic valve tests (D1-D9)

Test	Q_0 (lh^{-1})	Operating air pressure (bar)
D1	450	6.5
D2		4.5
D3		2.5
D4	200	6.5
D5		4.5
D6		2.5
D7	56.5	6.5
D8		4.5
D9		2.5

Observed transient pressure signals vary with the valve closure time, as depicted in Figure 3.12. A constant pressure value occurs at valve full closure, since all tests are generated by a fast closure manoeuvres. The remaining test measurements are shown in Appendix B.

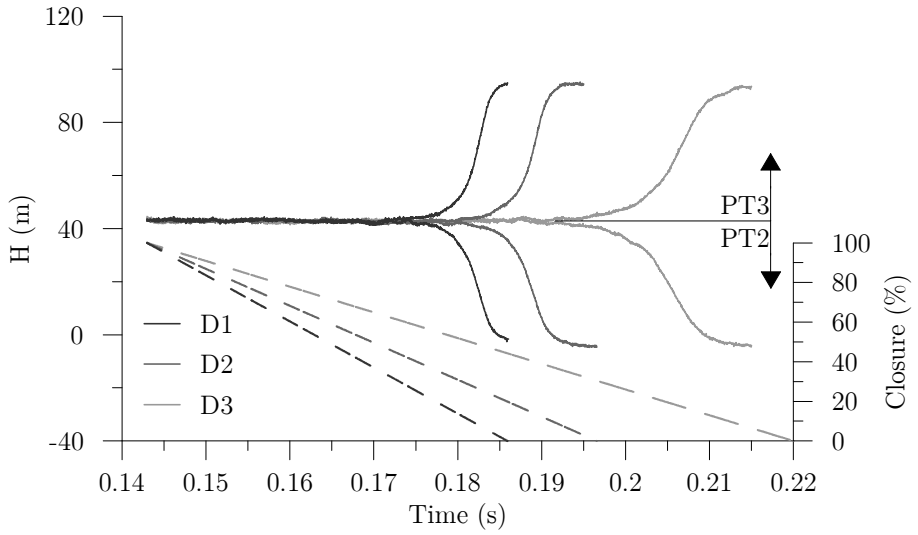

Figure 3.12. Dynamic valve tests: valve manoeuvre (dashed line) and piezometric head (continuous line) measurements for different closure times (D1-D3)

3.4.4 Dynamic tests for numerical model calibration and validation

The third set of tests – Dynamic tests for numerical model calibration and validation – is carried out to calibrate and validate the developed numerical model. Collected data are transient pressure heads at PT3 (downstream end) and PT4 (mid-length) and initial flow rate, Q_0. To fully characterize the system, turbulent, transitional and laminar flows are tested, using the same initial conditions as for the static behaviour of the spherical valve (Table 3.2). For the described tests, only 6.5 bar air operating pressure manoeuvres are considered to keep the same closure time. Higher flow rates are not considered, as cavitation occurs.

Each test was repeated 20 times with a data collection of 40 kHz frequency. A 20 test ensemble average was used to reduce the noise in the data acquisition system, as Martins *et al.* (2016) stated that for the same facility and equipment a 15 test sampling would be enough to a considerable noise reduction. This allows the minimization of electrical noise and other interferences on pressure measurements. The treated experimental data are depicted in Figure 3.13. As the valve does not close instantaneously, a smoother pressure rise is observed and is propagated for the subsequent pressure variations during pressure wave reversal. After the first pressure rise, pressure signal becomes close to the "squared" wave shape, typical of instantaneous manoeuvres.

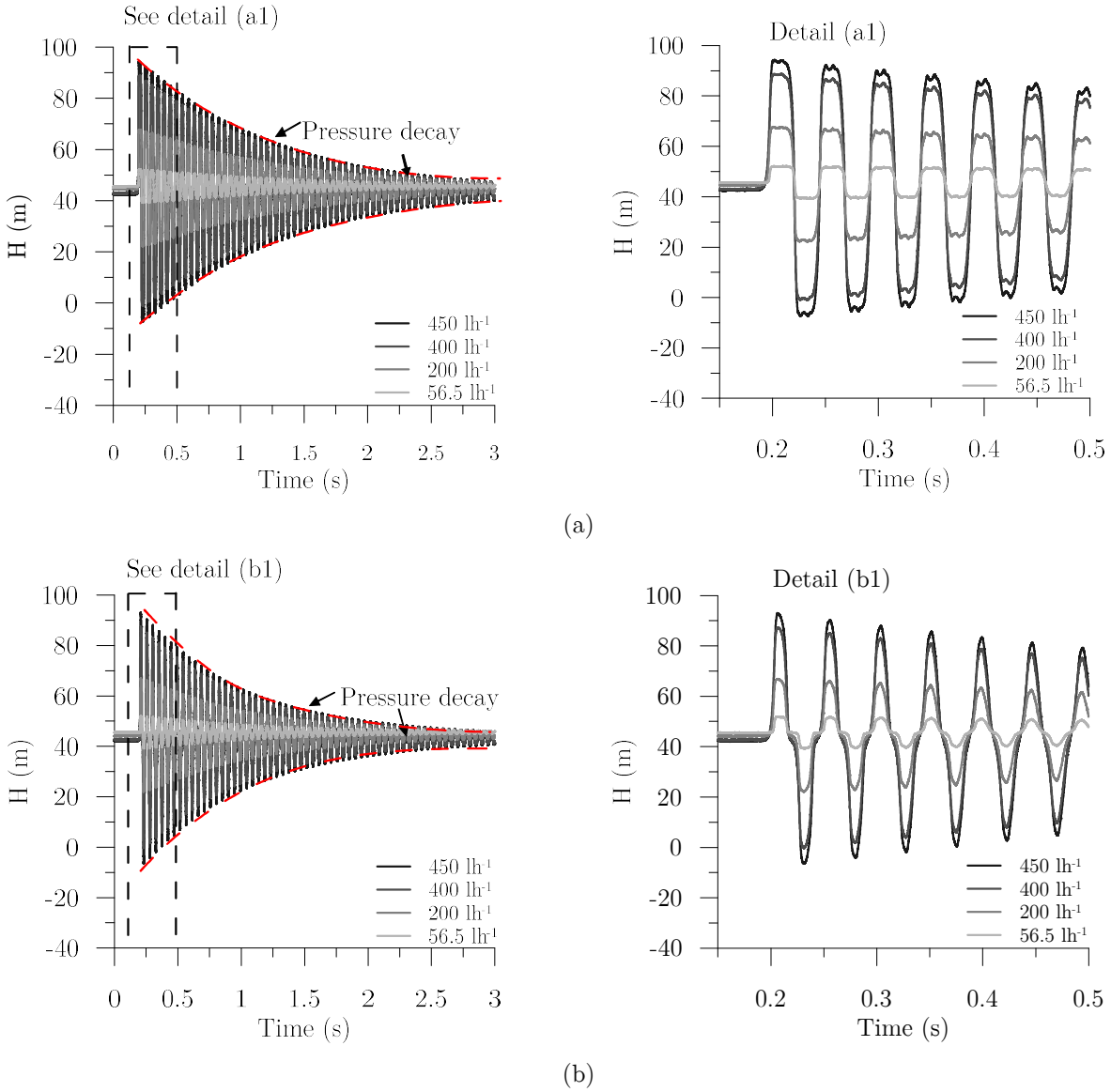

Figure 3.13. Sampled mean average for each transient test: (a) transducer PT3 and (b) transducer PT4

Some disturbances can also be observed in the pressure signal (Figure 3.13, details a1, b1) due to fluid structure interaction (FSI). This interaction was deeply analysed and discussed by Ferràs *et al.* (2016), who defended that these oscillations are due to slight movements of the pneumatically actuated valve during the water hammer event.

3.4.5 Dynamic tests for the wall shear stress analysis

In the last set of tests – Dynamic tests for the wall shear stress analysis – which consider the same initial flow conditions as the previous set, not only pressure-head (at transducers PT3 and PT4) but also wall shear stress are measured during transient events. The probe was configured for 40°C sensor temperature and a 28°C water temperature. The carried out tests have once more the initial flow conditions as in the ones for the static behaviour of the valve (initial flow rates of 450, 400, 200 and 56.5 lh^{-1}).

Experimental measurements obtained in the initial 450 lh^{-1} flow rate test are shown in Figure 3.14 and the remaining tests are presented in Appendix C. Measurements concerning wall shear stress, obtained in tension by the MiniCTA, must go through a calibration process for obtaining the real values of these parameter; this issue will be further developed and discussed in Chapter 6. Frequencies of 40 kHz and 10 kHz are used for the pressure and the wall shear stress measurements, respectively.

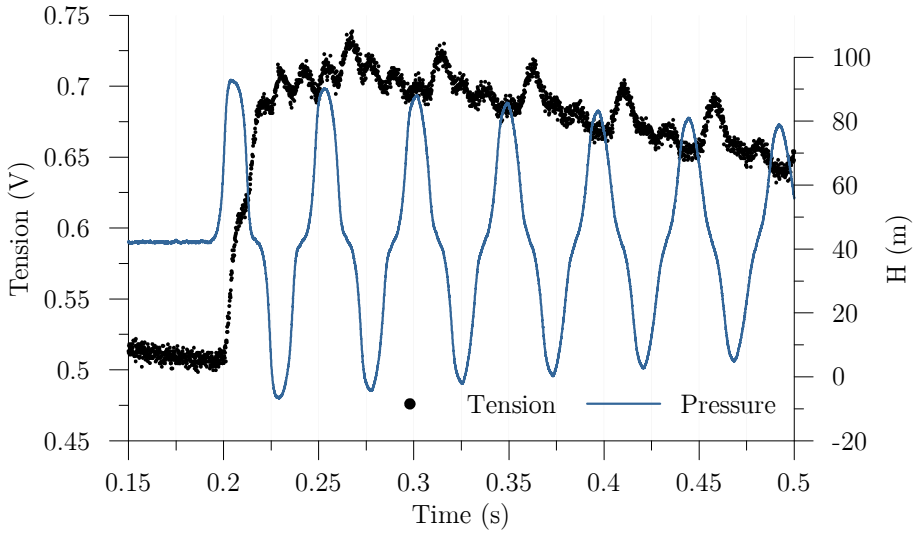

Figure 3.14. Pressure at PT4 and MiniCTA measurements for initial flow rate of 450 lh^{-1}

Chapter 4 | Spherical valve behaviour

4.1 Introduction

Valves have a major importance for the water pipe systems' operation. Moreover, if not properly designed, operated or maintained, cavitation and undesired operational conditions may occur associated to these components. If a valve is subjected to cavitation, an anticipated substitution is also susceptible to occur due to inner erosion, not regarding the noise, vibration or performance decrease. Despite the existence of established closure manoeuvres, if a valve closes too fast, a pressure surge may occur, which may lead, in the limit, to the occurrence of cavitation or to a pipe burst.

Valves used to operate pipe systems are called control valves. Regarding that a good knowledge of their behaviour is needed for modelling purposes, a set of tests is carried out to characterize the static behaviour of a spherical valve. This behaviour is described by the flow rate variation as function of the valve opening (or rotation angle). This step is important since the valve characteristics strongly depend on the valve type, geometry and size.

Transient valve tests are also carried out to evaluate the dynamic behaviour of the spherical valve. This behaviour can be mathematically described as a boundary condition by defining a given flow rate time variation or a valve manoeuvre knowing the valve head loss coefficients (or discharge coefficients). Two different approaches are discussed for modelling the valve manoeuvre: one considering an in-line valve, and another one as a valve discharging to the atmosphere. A flow rate closure law is proposed for each test to better describe the observed transient events when using the numerical model. Considerations are also made on the dynamic valve closure and on the flow rate variation with the valve closure time.

4.2 Procedure description

The orifice equation is used to determine the flow rate, Q, through the valve, based on collected data:

$$Q = C_d S_V \sqrt{2g\,(H_u - H_d)} \tag{4.1}$$

where C_d is the valve discharge coefficient, S_V is the area of valve cross-section in the totally opened position; and H_u and H_d are the piezometric-heads upstream and downstream the valve, respectively. Head loss coefficients can also be estimated by:

$$\Delta H = H_u - H_d = K_V \frac{Q^2}{2g{S_V}^2} \therefore K_V = 2gS_V^2 \frac{(H_u - H_d)}{Q^2} \tag{4.2}$$

in which K_V is the head loss coefficient through the valve for a specific percentage of closure.

As flow rate cannot be measured for the transient event with the necessary frequency by the flowmeter, and this parameter in important for the characterization of the valve dynamic behaviour, an indirect

measurement is carried out. This is based on pressure measurements and on the use of Joukowsky formulation, Eq.(2.5), valid for fast manoeuvres. Joukowsky formulation, expressed in terms of flow rate variation, yields:

$$Q = Q_0 - \frac{gS(H_u - H_0)}{a} \tag{4.3}$$

in which Q is the flow rate at time t, Q_0 is the steady-state flow rate, H_0 is the initial piezometric-head, and a is the wave celerity. This equation is only valid during the valve closure or opening.

4.3 Valve static behaviour

Figure 4.1 shows the measurements carried out in the static valve tests S1 to S4 in terms of the dimensionless flow rate, Q / Q_0. The dimensionless flow rate remains relatively constant until 70% closure is attained, from which the discharge takes different paths depending on the initial flow rate. The higher the initial flow rate is, the earlier the discharge changes and the less-steepened the variation becomes. This is taken to the limit of laminar flow (S4 test, Q= 56.5 lh^{-1}), in which the flow rate only changes on the last 5% of closure (i.e., between 89% and 94%).

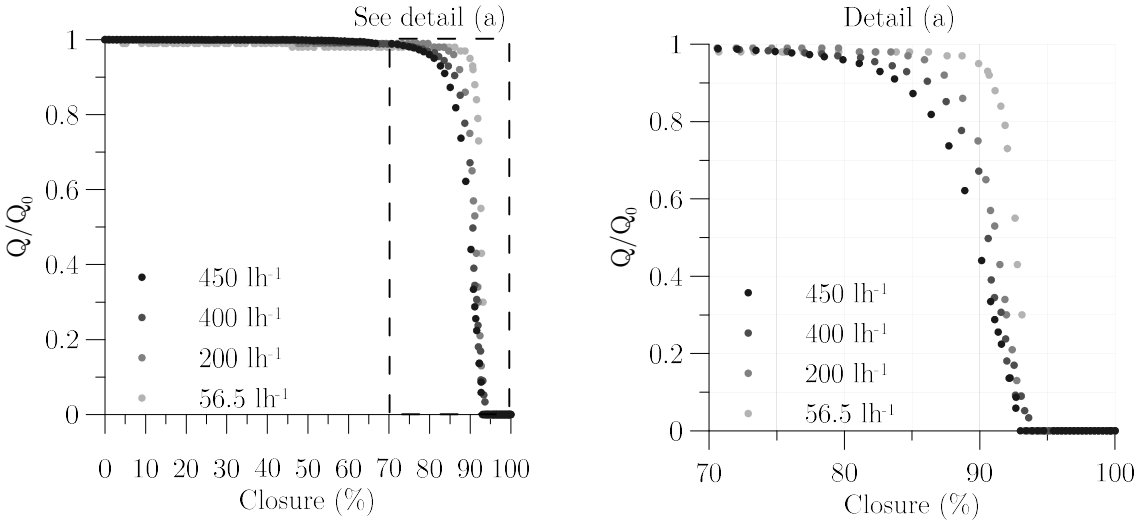

Figure 4.1. Dimensionless flow rate relation with closure angle

Another parameter that is expected to be constant for different initial flow rates is the ratio between the flow rate and the valve head loss square root, $Q / \sqrt{\Delta H}$, according to the orifice law, Eq.(4.1), varying only with the opening cross section. The variation of this parameter with the valve closure and with the initial flow rate is presented in Figure 4.2.

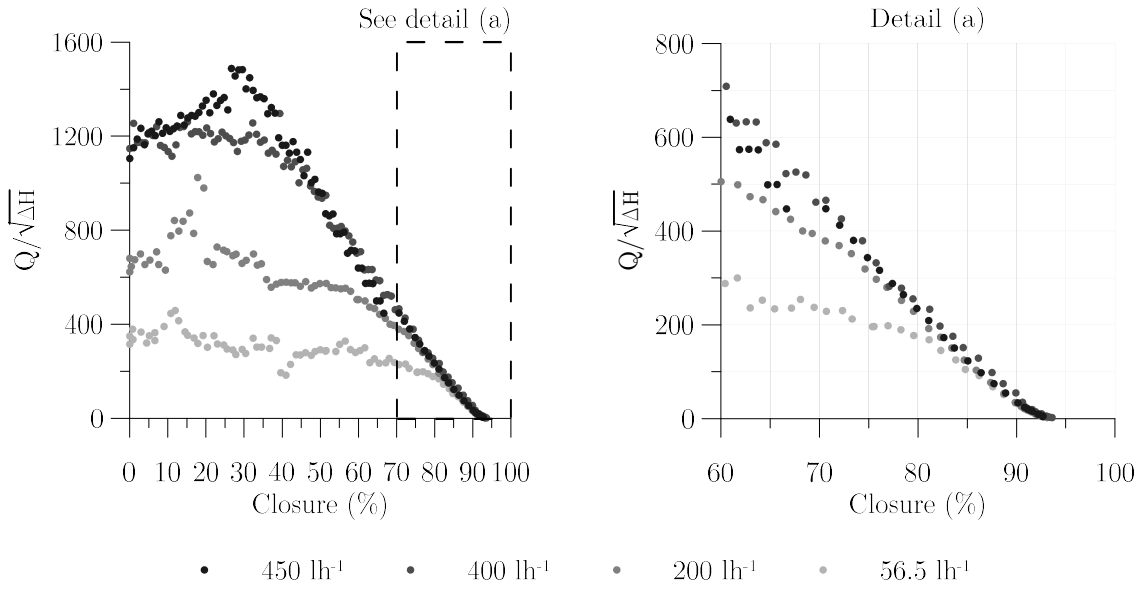

Figure 4.2. Experimental discharge coefficient according to the initial flow rate

A reasonably good fitting is observed for the obtained results for turbulent flows (450 and 400 lh^{-1}), except between 0 to 35% of closure. Higher discrepancies are observed in the discharge coefficients for transitional (200 lh^{-1}) and laminar flows (56.5 lh^{-1}), showing a good fitting with the obtained results for turbulent flows at the final stage of closure (83-94% closure). As these discrepancies are flow rate dependent, a more detailed analysis and discussion is carried out in the following paragraphs in terms of head loss coefficients.

Head loss coefficients of the spherical valve for different closure angles and initial flow rates are shown in Figure 4.3. These coefficients are calculated based on Eq.(4.2). These are obtained for different flow regimes, namely laminar (56.5 lh^{-1}), transitional (200 lh^{-1}) and turbulent (450, 400 lh^{-1}) flows. Several conclusions can be drawn from the analysis of these coefficients.

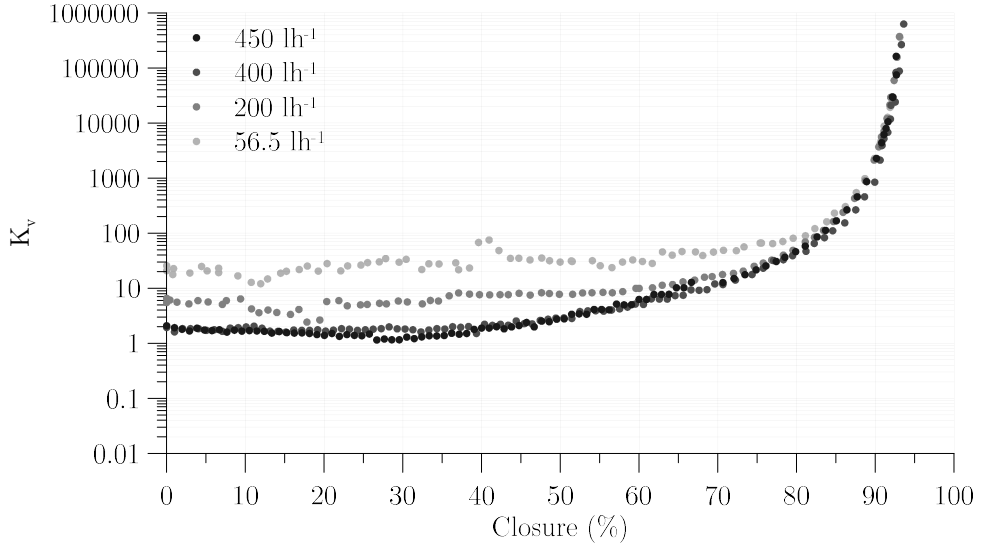

Figure 4.3. Experimental head loss coefficients for the tested spherical valve, obtained for different initial flow regimes

As expected, valve head loss coefficients, K_V, take the lowest values for the valve fully opened (0% closure); however, these K_V values vary with the initial flow conditions, being equal to 2, 7 and 20 for turbulent, transitional and laminar flows, respectively. These differences can be due to two main reasons. The first is the higher uncertainties in pressure measurements for lower flow rates, as the measured head losses for laminar flows (0.03-0.05 m) are lower than the accuracy range of the transducers (0.30 m); that occurs for a wide range of valve closure angles. The second reason is the effect of viscous forces, which are dominant over inertial forces in laminar and transitional flows, leading to increased head losses in comparison with turbulent flows; these increased head losses are described by the higher K_V values for lower Re; a similar phenomenon has been observed by Tian *et al.* (2013) when using a CFD model to describe globe valves' and elbows' behaviour for different flows. White (2010) also supports this observation by stating that K_V generally decreases for the higher Reynolds number, as shown in Figure 4.4 for the particular case of the 90° elbow.

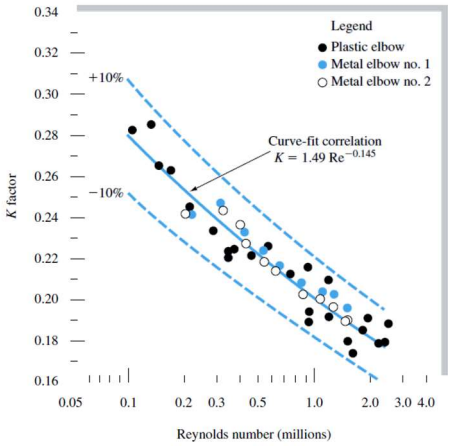

Figure 4.4. Recent measured loss coefficients for 90° elbows (White, 2010)

Experimental coefficients for the two turbulent flows are quite similar for the whole range of valve closure angles; these coefficients are associated with higher head losses and, consequently, with lower measurement uncertainties; in these tests, inertial forces and turbulence are dominant over viscous forces. Both transitional and laminar flow coefficients show higher discrepancies from the ones for turbulent flow, particularly from 0% until a 83% closure is reached, after which the values of K_V tend to overlap with those from turbulent flows. This is because, when the valve is almost closed, the flow is rapidly accelerated and highly turbulent; as such, flow conditions tend to be the same independently of the initial flow regime; also, the pressure differences are much higher with less error associated.

The comparison between obtained head losses coefficients and coefficients from Miller (1990) and Idel′chik and Steinberg (1996) is shown in Figure 4.5 for spherical valves. Both Miller (1990) and Idel′chik and Steinberg (1996) data significantly differ from the observed behaviour, although the former getting a progressively better fit for higher closure angles. These differences are associated to the experimental conditions in which each test was carried (e.g., fully developed flow), the used equipment and the geometry and size of the tested valves.

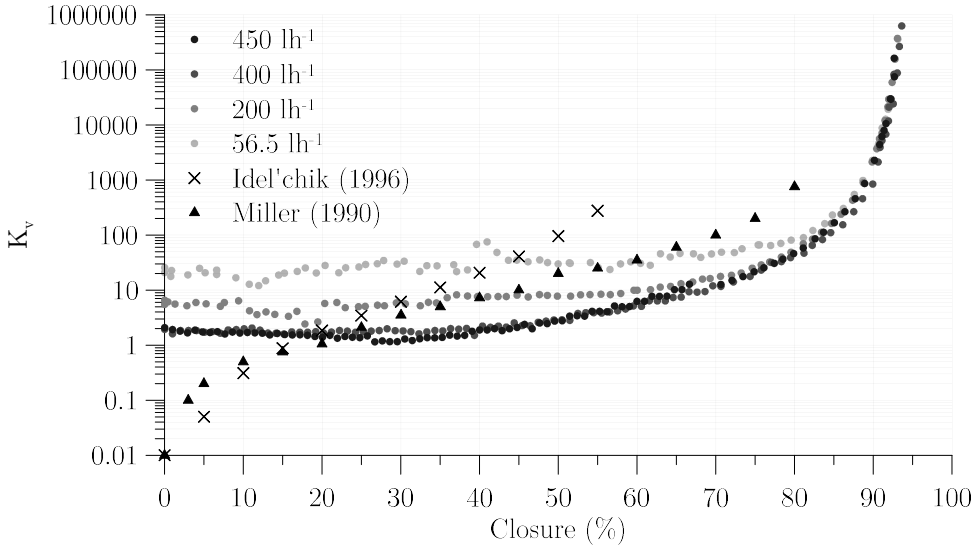

Figure 4.5. Comparison between experimental head loss coefficient and literature data

In summary, the valve static behaviour is Reynolds number dependent. This behaviour is described by different curves. As the Reynolds number increases, flow conditions tend to have the same features as in turbulent flow and the experimental coefficients tend to take similar values for the same angle. Characteristics head loss curve of the valve is an intrinsic valve characteristic and corresponds to the valve behaviour for fully developed turbulent flows.

4.4 **Valve dynamic behaviour**

4.4.1 Initial considerations

In order to characterize the dynamic behaviour of the valve during transient events, tests D1 to D9 were carried out to determine the corresponding closure law. Two modelling approaches have been considered for defining the valve closure laws:

a) The *first approach* describes the discharge variation as an in-line valve, based on the upstream and downstream pressure-head difference as defined by Eq.(4.1).

b) The *second approach* describes the discharge variation as a valve discharging to the atmosphere, considering only the upstream pressure-head measurement and assuming that the pressure-head at downstream is constant (in this case, null for relative pressures).

The latter approach is the most usual in hydraulic transient analysis, yet, this is not strictly accurate in many cases, like in the analysed pipe-rig, as there is a pressurized return pipe at downstream the valve that allows the recirculation of the flow to the tank. Indeed, this approach is a simplification of the real phenomenon, however, it accurately describes the observed valve behaviour during the transient event in this test-rig.

Both approaches, discussed in the following sections, correspond to indirect flow rate measurements as the flow meter does not allow data collection during transient events. As such, pressure-head data are used for estimating the flow rate based on Joukowsky/Michaud formulations for fast/slow manoeuvres.

4.4.2 Closure time

The total closure time of the valve, t_c, and the effective closure time obtained by Eq.(4.4) according to Lescovich (1967), t_{ef}, are presented in Table 4.1.

$$t_{ef} = \frac{\Delta Q}{\left(\frac{dQ}{dt}\right)_{max}} \tag{4.4}$$

The valve closure time increases with the decrease of operating air pressure in the valve control system. Despite the total closure time being significantly higher than the system characteristic time, $2L / a$ (0.024 s), all tests correspond to fast manoeuvres, since the effective closure times are much lower than $2L / a$, varying between 0.0028 and 0.0050 s.

Note that the calculation of the system characteristic time $2L / a$ requires the prior estimation of the wave speed. Considering that the pipe is thick ($e > D / 20$), the water is at a 20 ºC temperature and the Young modulus of elasticity of the copper pipe is 105 GPa (experimentally determined by Ferràs *et al.*, 2016), the wave celerity is 1269.2 ms^{-1} and the corresponding system characteristic time is 0.024 s.

Table 4.1. Valve closure time and effective closure time

Test	Q_0 (lh^{-1})	Operating air pressure (bar)	Closure time, t_c (s)	Effective closure time, t_{ef} (Lescovich, 1967)
D1	450	6.5	0.043	0.0028
D2		4.5	0.054	0.0031
D3		2.5	0.061	0.0046
D4	200	6.5	0.048	0.0016
D5		4.5	0.053	0.0023
D6		2.5	0.074	0.0032
D7	56.5	6.5	0.045	0.0020
D8		4.5	0.051	0.0044
D9		2.5	0.055	0.0050

In this context, valves manoeuvres should be classified according to the effective closure time in comparison with the system characteristic time; this issue was deeply discussed by Lescovich (1967). Figure 4.6 depicts the spherical valve flow rate variation and effective closure time estimation for test D1. For this test, the valve effective closure time is 6% of the total valve manoeuvre. This behaviour is typical of spherical valves. These differences are the reason why closure laws must be defined and implemented in the numerical model and not only considering a linear flow rate variation.

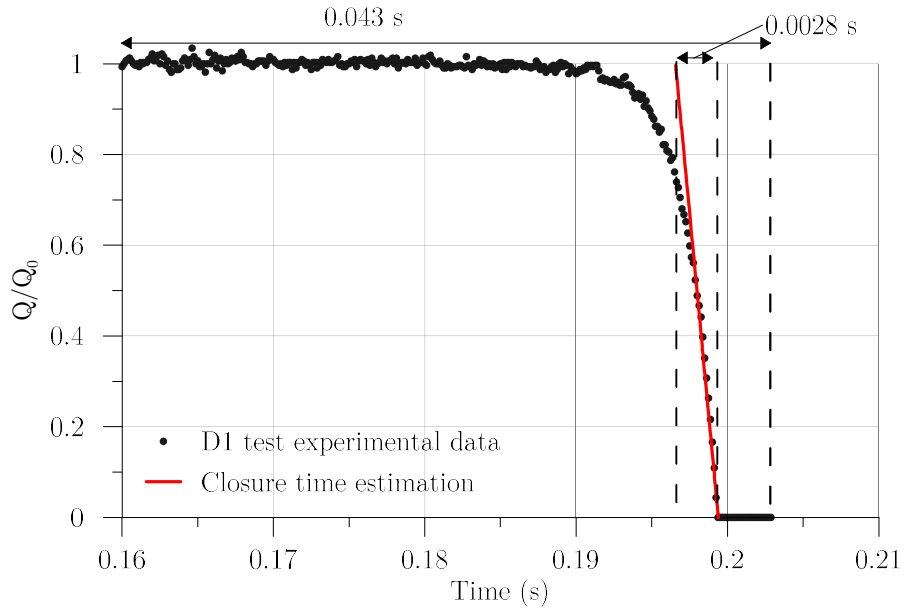

Figure 4.6. D1 test effective time closure estimation

4.4.3 First approach: in-line valve

The first approach describes the valve discharge, Q, in transient conditions based on the pressure-head difference between both ends of the valve, $H_u - H_d$, as an in-line valve installed in a pipeline. The respective closure curves are presented Figure 4.7 for three initial flow rates (56.5, 200 and 450 lh^{-1}). For each flow rate, a combination of three closure times (controlled by the supplied air pressure, 2.5, 4.5 and 6.5 bar) have been tested. As expected, the valve dynamic behaviour follows almost the same valve law as for static conditions between 0 and 83% closure, described by Eq.(4.1), since this equation is valid for both steady and unsteady-state flows. The valve is completely closed at 84.5º closure angle. This is observed for the three initial discharges.

However, a small flow rate discrepancy is observed at the final stage of closure, between 75º and the total closure angle (during the valve effective closure). For every initial flow rate, the higher the air pressure is, the faster the valve closes and the higher flow rate discrepancy becomes, leading to a steeper flow rate change at this stage (between 83% and 94% closure). This is because the faster the valve closes, the lesser time the flow has to reach an equilibrium, leading to a higher discrepancy from the steady flow closure.

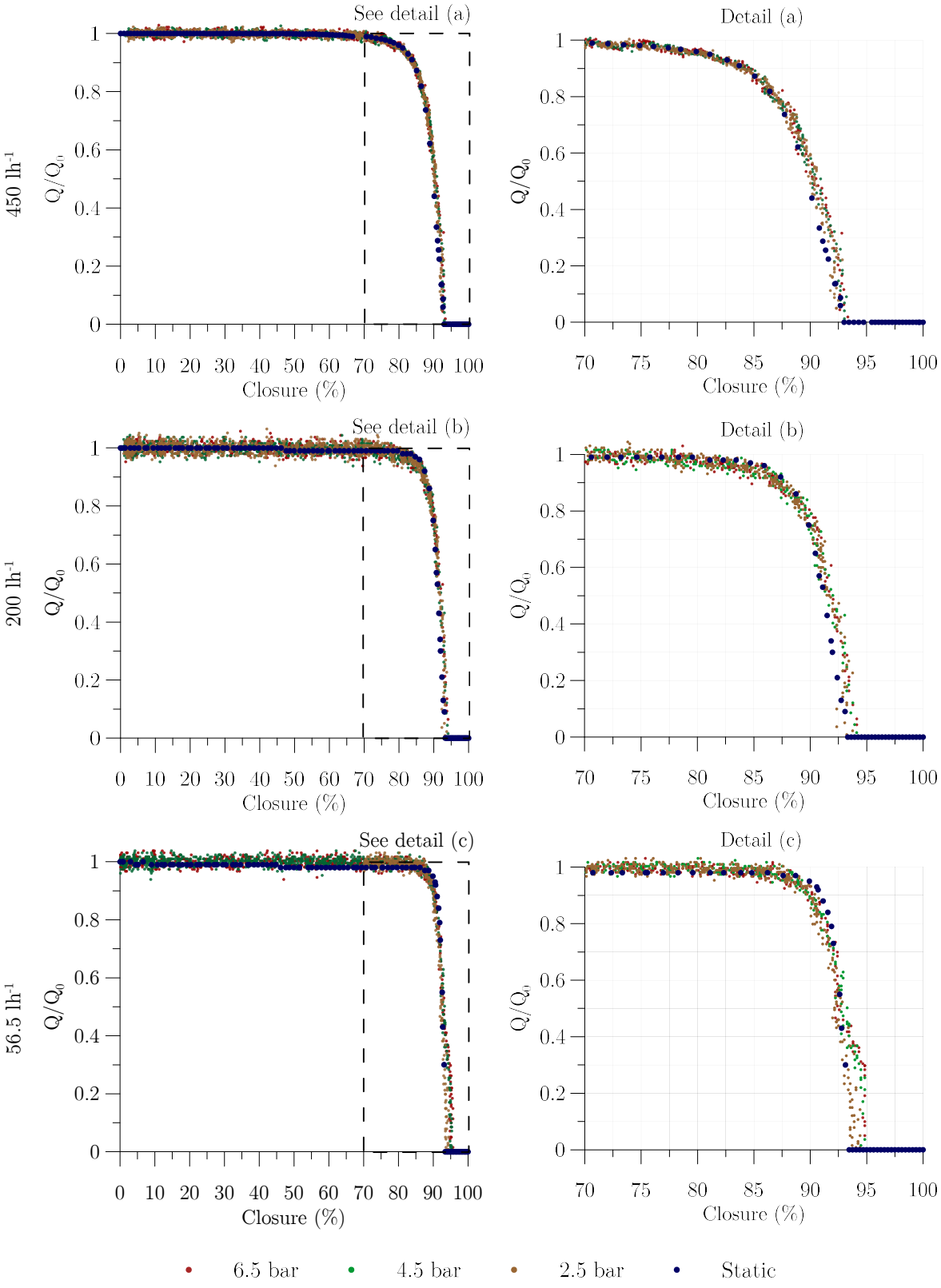

Figure 4.7. Dimensionless flow rate using upstream-downstream approach for each closure time for 450, 200 and 56.5 lh^{-1}

In order to numerically describe the flow variation for each initial condition, the function that better fits the observed experimental behaviour is a hyperbolic function:

$$\frac{Q}{Q_0} = 1 - \left(\frac{angle - m}{90}\right)^n \tag{4.5}$$

The constant parameters, m and n, that better fit experimental data, as well the coefficient of determination, R^2, are presented in Table 4.2.

Table 4.2. Closure law coefficients for each scenario for upstream-downstream approach

First approach	D1	D2	D3	D4	D5	D6	D7	D8	D9
m	-6.00	-6.13	-6.25	-5.20	-5.35	-5.50	-3.15	-3.00	-2.75
n	24	24	24	31	31	31	55	55	55
R^2	0.989	0.990	0.986	0.974	0.972	0.963	0.912	0.906	0.946

The obtained numerical closure laws as well as the static valve closure measurements are shown in Figure 4.8 for different closure times (i.e., D1 to D3 scenarios). Minor differences can be observed between different closure times, though the faster the valve closes, the further way from the static behaviour the response of the valve is.

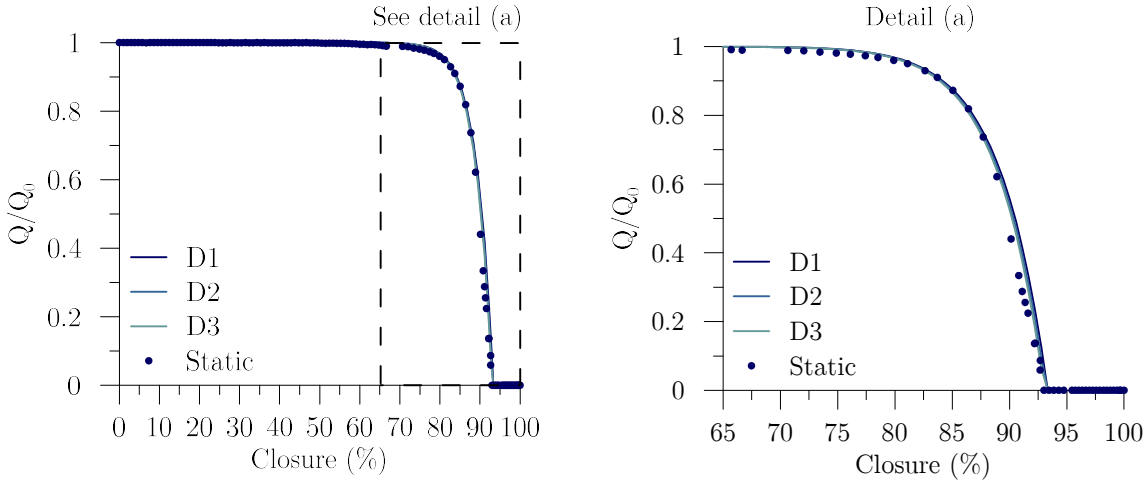

Figure 4.8. D1-D3 numerical valve closures laws and static experimental closure: in line valve model

4.4.4 Second approach: valve discharging to the atmosphere

The second approach describes the valve discharge in transient conditions based the pressure-head at the valve upstream end, as if the valve were discharging to the atmosphere or to a constant head reservoir and the valve downstream pipe did not exist in the system. This is the common approach used in numerical models. However, such condition does not correspond to the one in the existing facility. Thus, an artificial scheme is developed in order to simplify the system, avoiding the numerical simulation of the return pipe at downstream the valve, but describing the valve as accurately as possible. Hence, a valve closure law is determined and modelled, neglecting the pressure downstream the boundary condition.

Considering only the upstream end pressure history until complete valve closure, Eq.(4.3) is applied and the resulting closure curves for each scenario are shown in Figure 4.9. The flow rate variation has the same behaviour as the one observed in the first stage of closure for static (or steady) conditions. However, as the valve closes, pressure-head increases and the valve discharge pattern (sigmoid) has a completely

different response from that obtained in the first approach (hyperbolic), compare Figure 4.7 and Figure 4.9.

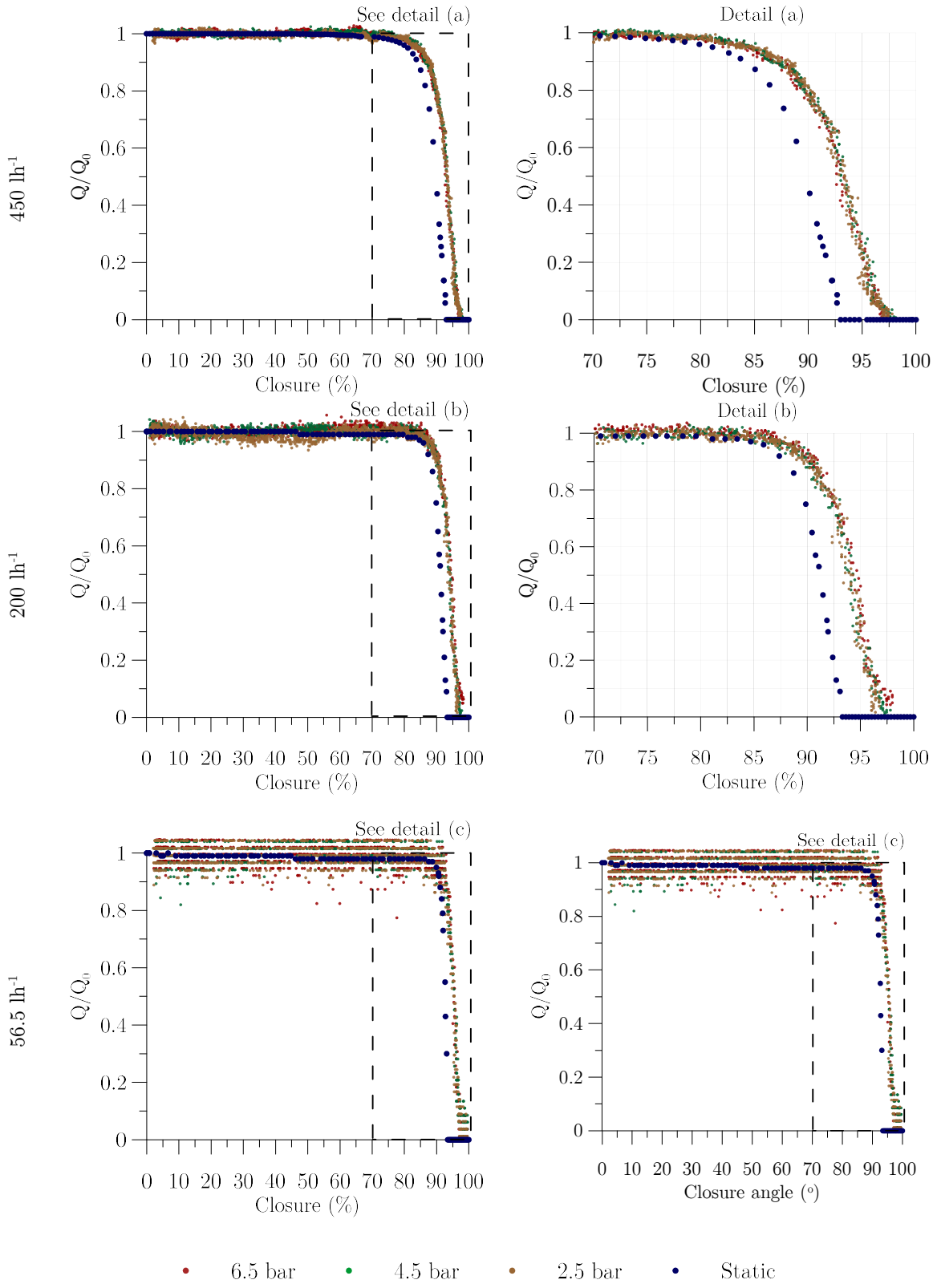

Figure 4.9. Dimensionless flow rate using upstream-upstream approach for each closure time for 450, 200 and 56.5 lh^{-1}

The valve discharge can be described by this approach as a sigmoid function:

$$\frac{Q}{Q_0} = 1 - \left(\frac{1}{1 + e^{-l(angle-m)}}\right)^n \tag{4.6}$$

which better-fitted constants are presented in Table 4.3

Table 4.3. Closure law coefficients for each scenario for upstream-upstream approach

Second approach	D1	D2	D3	D4	D5	D6	D7	D8	D9
l	1.75	1.75	1.85	1.5	1.70	4.20	6.00	6.00	6.00
m	86.	86.0	86.0	86.5	86.0	86.5	88.25	88.5	87.5
n	0.18	0.19	0.17	0.30	0.30	0.10	0.091	0.08	0.094
R^2	0.995	0.990	0.986	0.995	0.989	0.982	0.900	0.914	0.907

It should be highlighted that this corresponds to the numerical description of the valve behaviour to be implemented in the numerical model when neglecting the pipe at downstream the valve and replacing it by a constant pressure-head or a valve discharging to atmosphere.

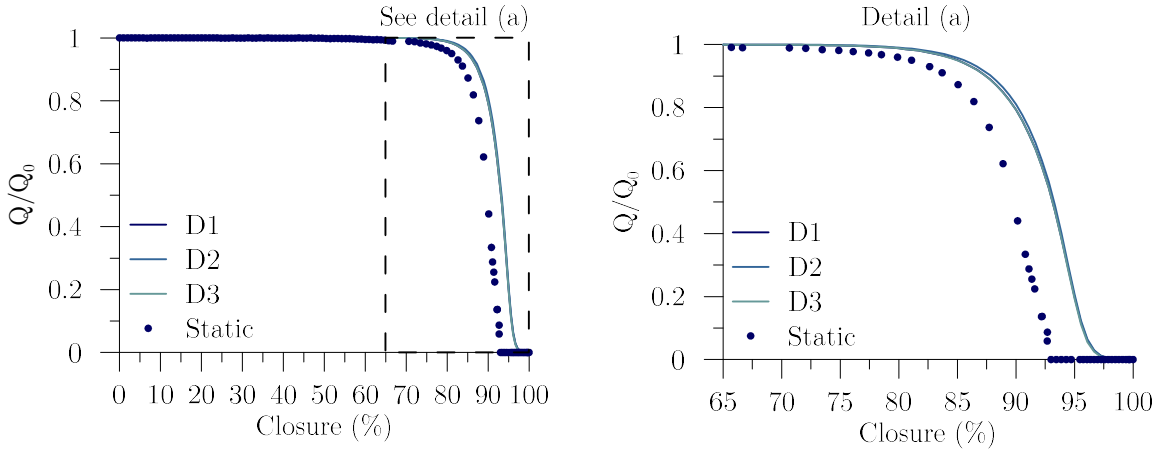

Figure 4.10. D1-D3 numerical valve closures laws and static experimental closure: discharge to the atmosphere

4.5 CFD valve closure

As a complement to the present research, an *Ansys Fluent* CFD model developed by Dr. Nuno Martins was used for the flow conditions presented in Table 3.3. A sensitivity analysis was carried out in order to evaluate the effect of the upstream pipe length in the valve discharge law. Two pipe lengths are analysed: 1 m and 15.02 m.

The model set up considers hydraulically smooth pipe and the wall is described by the "no slip-condition" (Day, 1990). Upstream boundary consists of a constant pressure allowing backflush as in the hydro pneumatic vessel. For the downstream boundary, the valve was geometrically described as a cylindrical shape with domed ends to characterize the quarter turn spherical valve. Two interfaces were considered: a) the inner surface of the valve; b) the disconnection surface that interferers with the flow and defines the amount of valve aperture/closure. The cylindrical shaped body with domed ends that corresponds to the valve body is depicted in Figure 4.11.

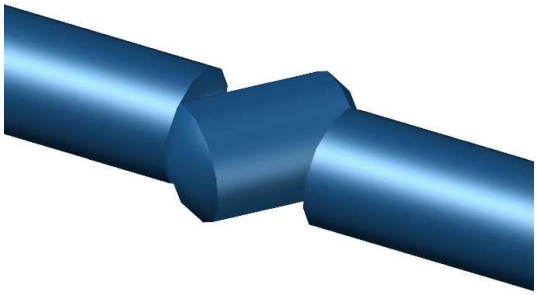

Figure 4.11. Valve body in CFD model

In order to define the flow in the system, a pressure difference at both reaches of the system was considered. The implemented numerical model was a finite volume method in which the flow solver uses a Semi-Implicit Method for Pressure-Linked Equation (SIMPLE) algorithm. This is a pressure-based solver that considers velocity and pressure corrections to carry out mass and momentum conservation equations and furthermore the system pressure field. The method convergence is assessed by tracking the imbalances by advancement in solving equations in each time step. These imbalances, known as residuals, allow to determine if each iteration is converging or not to the conservation flow properties. Thus the convergence criterion is pre-set inside the solver, within the iterative parameters. In the present case, the criterion (the relative error of the calculated parameters due to flow characteristics) is set to 10^{-3}.

The comparison between the measured dynamic valve behaviour and the CFD results are depicted in Figure 4.12 for two initial flow rates: the turbulent flow, 450 lh^{-1}, and the laminar flow, 56.5 lh^{-1}, as the transitional flow is not theoretically well-described. A flow rate offset can be observed for both flow rates for 1 m pipe length upstream the valve, in comparison with measurements; however, CFD results for a 15.02 m pipe fit quite accurately the measurements, with almost a perfect match between them. This 1 m pipe length was simulated to assess the variation of the flow rate with the pipe length.

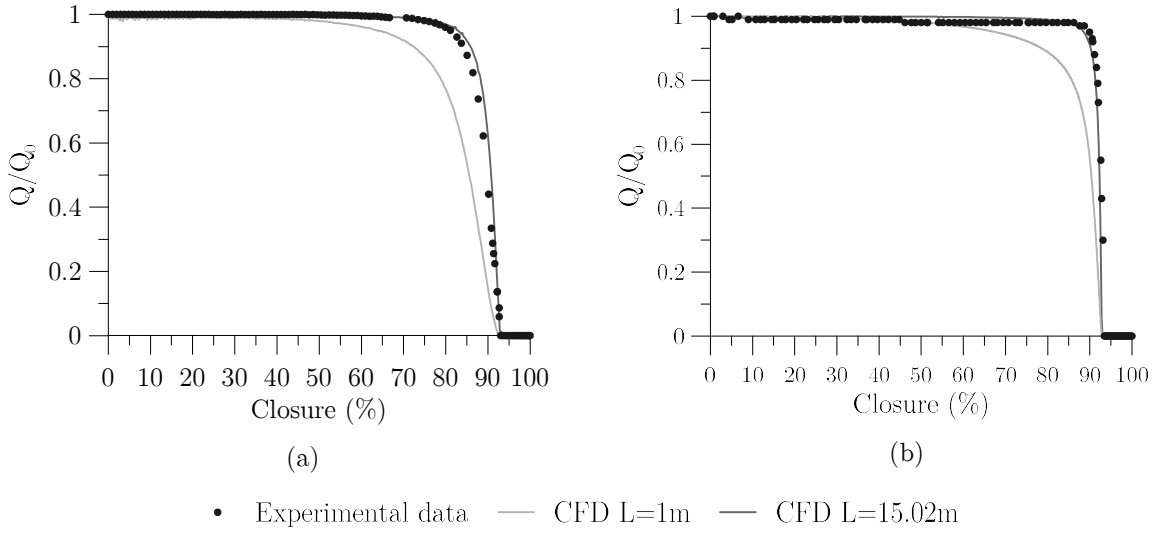

Figure 4.12. CFD results for 1 and 15.02 m pipe upstream for: (a) 450 lh^{-1} and (b) 56.5 lh^{-1} initial flow rate.

This flow rate discrepancy between the 1 m and 15.02 m pipe is associated with the pipe characteristic time, $2L / a$, which is 15 times smaller in the 1 m pipe. This causes the valve manoeuvre to be considered

slow and the pressure wave reversal interferes with the flow rate, diminishing the pressure-head, and, consequently, the valve discharge. The system characteristic time is 2.4×10^{-3} s for 15.02 m pipe and 1.6×10^{-4} s for 1 m pipe, which is smaller than the valve effective closure time (Table 4.1) for both initial flow rates. Figure 4.13 presents a sequence of snap-shots of the valve closure with respective velocity vectors. Closures between 80% and 87% correspond to high velocities in the valve inlet and outlet corroborating the conclusion of the occurrence of highly turbulent flow for high closures independently of the initial flow regime.

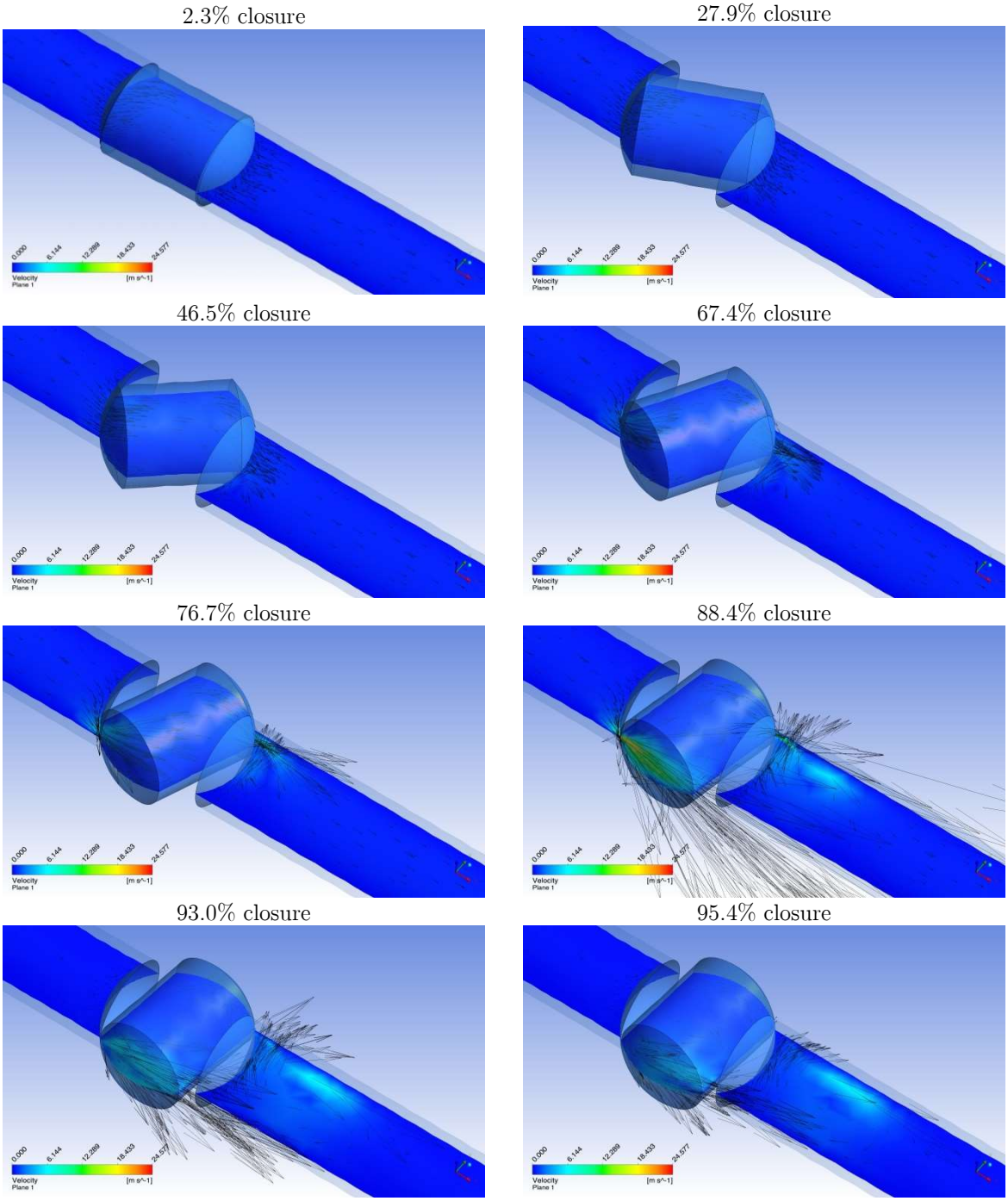

Figure 4.13.Velocity field during valve closure for Re_0 =7000 obtained by CFD modelling (*Courtesy of Dr. Nuno Martins*)

4.6 Final remarks

Being boundary conditions a major issue in hydraulic systems, especially in water hammer events a good characterization of these elements is essential for a good fitting between experimental data and numerical models. The static and dynamic behaviour of the spherical valve were characterized to describe as best as possible the system boundary condition.

The static valve behaviour is mainly characterized by head loss and flow variation, which are Reynolds number dependent. A total closure can be observed for 94% of closure (i.e., 85° closure angle).

A formulation to describe the valve dynamic behaviour using only the upstream pipe reach is proposed herein. This boundary condition does not correspond to a valve with a discharge to atmosphere but a valve with pressure variation both at the upstream and the downstream ends. That is the case of many valves in pressurised pipe systems, reason why this approach is important.

As the valve closure time decreases, the observed dynamic flow rate approaches to the one corresponding to the static (or steady-state) law. This flow rate difference is due to the flow instability as the valve closure is faster than the progressive valve axis rotation in static tests, allowing time for the flow to stabilize.

CFD results have highlighted that the same valve manoeuvre in pipe systems with different lengths leads to different flow variations, has different effective closure times and is described by different closure laws.

Chapter 5 | Model calibration and results analysis

5.1 Introduction

A 1D hydraulic transient model based on the classic water hammer theory and the method of characteristics (MOC) is implemented by the author of this document. The classic water hammer approach has always been considered sufficient for studying the phenomenon as maximum pressures are reasonably well predicted. However, the pressure wave dissipation, phase and shift in time is not accurately described, having been improved with several unsteady friction models.

This chapter presents the main equations that describe fluid transient events, the implemented equations in the numerical model, as well as the usual equations to describe the relevant boundary conditions for the experimental facility (i.e., reservoirs and valves).

An essential component of model development is the calibration process. The developed numerical model is calibrated and results discussed. In a first stage, pressure wave celerity is theoretically calculated and experimentally obtained. Steady-state friction is compared with Blasius friction formulation to assess if this approach is appropriate for the analysed smooth wall pipe. Finally, two valve descriptions are discussed according to the approaches defined in Chapter 4. This chapter follows the methodology proposed by Carriço *et al.* (2016) in what concerns hydraulic transient model calibration.

Unsteady friction formulations importance is highlighted by comparing experimental data with model results for a classic solver. Turbulent and laminar flows are subsequently compared with numerical results for the most relevant implemented unsteady friction formulations and conclusions are drawn. A time-step analysis is carried out to determine if unsteady friction formulations are time dependent and how they vary the time-step change.

5.2 Numerical model

5.2.1 Main equations

Within the 1D approach, unsteady-state pressurized flow in closed conduits is simulated by a set of two differential equations based on mass and momentum conservation principles (Almeida and Koelle, 1992, Wylie *et al.*, 1993, Chaudhry, 2014).

$$\frac{\partial H}{\partial t} + \frac{a^2}{gS}\frac{\partial Q}{\partial x} = 0 \tag{5.1}$$

$$\frac{\partial H}{\partial x} + \frac{1}{gS}\frac{\partial Q}{\partial t} + \frac{4}{\rho g D}\tau_w = 0 \tag{5.2}$$

These equations are once more presented due to their relevance in this context. Main assumptions associated with these equations development related to fluid, flow and pipe are summarized in Table 2.2.

Since a general solution of the partial differential Eq.s(5.1) and (5.2) is not available, numerical procedures must be used. Typically, the numerical integration of these equations is performed using the MOC, and Eq.s(5.1) and (5.2) are transformed into the following set of ordinary differential equations:

$$\begin{aligned} C^+ &: \frac{dQ}{dt} + \frac{gS}{a}\frac{dH}{dt} + R^* Q\left|Q\right| = 0 \\ C^- &: \frac{dQ}{dt} - \frac{gS}{a}\frac{dH}{dt} + R^* Q\left|Q\right| = 0 \end{aligned} \tag{5.3}$$

where R^* refers to the pipe resistance factor for laminar, $R^* = 32\nu \,/\, (gD^2 S)$, and turbulent flows, $R^* = f \,/\, (2gDS^2)$. Eqs.(5.3) are valid along the straight characteristic line C^+ and C^-, since the mean velocity, V, is negligible relative to the pressure wave speed $\left(V \ll a\right)$.

Using the MOC approach, the pipe is divided into a number of reaches, with the length of Δx, so that $\Delta x = a\Delta t$. This way, the two differential equations Eqs.(5.3) can be rewritten in the following simplified linear form:

$$\begin{aligned} C^+ &: Q_{i,j} = C_P + C_{a+} H_{i,j} \\ C^- &: Q_{i,j} = C_N - C_{a-} H_{i,j} \end{aligned} \tag{5.4}$$

where C_P, C_N, C_{a+} and C_{a-} are constants coefficients that can be applied at section i and time j. These coefficients depend on the numerical scheme used to simulate the steady-state friction and the unsteady friction model considered. These coefficients are defined as follows:

$$C_P = \frac{Q_{i-1,j-1} + BH_{i-1,j-1} + C_{P1}{}' + C_{P1}{}''}{1 + C_{P2}{}' + C_{P2}{}''} \tag{5.5}$$

$$C_N = \frac{Q_{i+1,j-1} - BH_{i+1,j-1} + C_{N1}{}' + C_{N1}{}''}{1 + C_{N2}{}' + C_{N2}{}''} \tag{5.6}$$

$$C_{a+} = \frac{B}{1 + C_{P2}{}' + C_{P2}{}''} \tag{5.7}$$

$$C_{a-} = \frac{B}{1 + C_{N2}{}' + C_{N2}{}''} \tag{5.8}$$

where parameter $B = gS \,/\, a$ and superscripts $'$ and $''$ refer to the steady-state and unsteady state friction components, respectively. Several unsteady friction formulae have been implemented in the numerical model. The formulae of these coefficients are presented in Table 5.1.

In order to calculate the flow rate and the piezometric-head in the pipe inner sections, the two following equations should be used:

$$H_{i,j} = \frac{C_P - C_N}{C_{a+} + C_{a-}} \tag{5.9}$$

$$Q_{i,j} = C_P - C_{a-} H_{i,j} \tag{5.10}$$

Table 5.1. C_{P1}, C_{P2}, C_{N1} and C_{N2} coefficients for steady and unsteady friction components (Martins, 2016)

Steady-state friction		
Frictionless	$C_{P1}' = C_{P1}' = 0$ $C_{N1}' = C_{N1}' = 0$	
First-order accuracy	$C_{P1}' = -R^* \Delta t \lvert Q_{i-1,j-1} \rvert Q_{i-1,j-1}$ $C_{P2}' = 0$	$C_{N1}' = -R^* \Delta t \lvert Q_{i+1,j-1} \rvert Q_{i+1,j-1}$ $C_{N2}' = 0$
Second-order accuracy Chaudhry and Hussaini (1985)	$C_{P1}' = 0$ $C_{P2}' = R^* \Delta t \lvert Q_{i-1,j-1} \rvert$	$C_{N1}' = 0$ $C_{N2}' = R^* \Delta t \lvert Q_{i+1,j-1} \rvert$
Unsteady friction		
Brunone *et al.* (1991a)	$C_{P1}'' = k_3\theta Q_{i,j-1} - k_3(1-\theta)(Q_{i-1,j-1} - Q_{i-1,j-2}) + k_3(Q_{i-1,j-1}) \lvert Q_{i,j-1} - Q_{i-1,j-1} \rvert$ $C_{N1}'' = k_3\theta Q_{i,j-1} - k_3(1-\theta)(Q_{i+1,j-1} - Q_{i+1,j-2}) + k_3(Q_{i+1,j-1}) \lvert Q_{i,j-1} - Q_{i+1,j-1} \rvert$ $C_{P2}'' = C_{N2}'' = k_3\theta$	
Bergant *et al.* (2001)	$C_{P1}'' = k_3\theta Q_{i,j-1} - k_3(1-\theta)(Q_{i-1,j-1} - Q_{i-1,j-2}) - k_3 SGN(Q_{i-1,j-1}) \lvert Q_{i,j-1} - Q_{i-1,j-1} \rvert$ $C_{N1}'' = k_3\theta Q_{i,j-1} - k_3(1-\theta)(Q_{i+1,j-1} - Q_{i+1,j-2}) - k_3 SGN(Q_{i+1,j-1}) \lvert Q_{i,j-1} - Q_{i+1,j-1} \rvert$ $C_{P2}'' = C_{N2}'' = k_3\theta$	
Ramos *et al.* (2004)	$C_{P1}'' = k_t\theta Q_{i,j-1} - k_t(1-\theta)(Q_{i-1,j-1} - Q_{i-1,j-2}) - k_x SGN(Q_{i-1,j-1}) \lvert Q_{i,j-1} - Q_{i-1,j-1} \rvert$ $C_{N1}'' = k_t\theta Q_{i,j-1} - k_t(1-\theta)(Q_{i+1,j-1} - Q_{i+1,j-2}) - k_x SGN(Q_{i+1,j-1}) \lvert Q_{i,j-1} - Q_{i+1,j-1} \rvert$ $C_{P2}'' = C_{N2}'' = k_t\theta$	
Trikha (1975) and Vardy *et al.* (1993)	$C_{P1}'' = C_{N1}'' = S\Delta t \frac{16\nu}{D^2} \sum_k \left[e^{-B_k \frac{4\nu}{D^2}\Delta t} Y_{k,j-1} - \frac{A_k}{S}(Q_{i,j} - Q_{i,j-1}) \right]$ $C_{P2}'' = C_{N2}'' = \Delta t \frac{16\nu}{D^2} \sum_k (A_k)$	
Zielke (1968) and Vardy and Brown (2003)	$C_{P1}'' = C_{N1}'' = \frac{16\nu}{D^2}\Delta t \cdot \left[W_{(t/\Delta t)} Q_{i,j-1} + \sum_{k=1}^{t/\Delta t - 1} W_{t/\Delta t-(k-1)}(Q_{i,k} - Q_{i,k-1}) \right]$ $C_{P2}'' = C_{N2}'' = \frac{16\nu}{D^2}\Delta t \cdot W_{(t/\Delta t)}$	

Parameter θ corresponds to the relaxation coefficient. This allows the positive equation to remain in the rectangular grid and do not requiring interpolations. For null values the time derivative becomes explicit but some instabilities may occur in certain conditions. For values $0 < \theta < 1$ the numerical scheme becomes implicit and the solution is unconditionally stable (Soares *et al.*, 2013).

5.2.2 Boundary conditions

Different types of boundary conditions exist in pipe systems, such as, valves, reservoirs and tanks, pumps, air chambers and hydro pneumatic vessels. Two boundary conditions were implemented in the numerical model. At the system upstream reach, the hydro pneumatic vessel is modelled as a constant head reservoir. Pressure can be considered the same as in the transient's event beginning. Thus, the only unknown variable is the inflow/outflow of the pneumatic vessel. The pneumatically actuated spherical valve can be described by three different approaches, depending on the condition at downstream the valve being a pipe reach (in-line valve), a constant level reservoir or the atmosphere. Implemented boundary condition equations are presented in Table 5.2.

Table 5.2. Implemented boundary condition equations (Covas, 2003)

Type	**Equations**		
Reservoir	$H_R = H_0$	$Q_{i,j} = C_N - C_{a-}H_R$	
Flow control valves	$H_N = \dfrac{C_N - Q_{i,j}}{C_{a+}}$	$Q_{i,j} = -\dfrac{2E_E}{C_N + \sqrt{B_E{}^2 + 4C_E\lvert E_E\rvert}}$	
In-line valves	$C_E = K_V(t) \,/\, (2gS_{V0}^2)$	$B_E = C_{a+}$	$E_E = H_d - C_N$
Valve to reservoir	$C_E = C(t)$	$B_E = C_{a+}$	$E_E = H_R - C_N$
Valve to atmosphere	$C_E = C(t) + \dfrac{1}{2gS(t)_v^2}$	$B_E = C_{a+}$	$E_E = Z - C_{Nu}$

being H_d the piezometric downstream the valve, H_R the reservoir head and z the valve geometric head.

5.3 Model calibration

5.3.1 Wave celerity estimation

The wave celerity is one of the most important parameters of hydraulic transient analysis in pressurised pipes. This parameter can be theoretically estimated by Eq.(2.1), as presented in 4.4.2, being obtained the value of 1269.2 ms^{-1}. Wave celerity can also be obtained based on the pressure wave period of the transient pressure signal, being observed a celerity of 1265.5 ms^{-1}.

Values are almost coincident, as such, from this moment onwards a wave celerity of 1265.5 ms^{-1} has been considered in this document. The obtained small difference is negligible.

5.3.2 Steady-state friction calibration

Darcy-Weisbach friction factors are estimated from pressure measurements (by Hagen–Poiseuille and Blasius formulation for laminar and turbulent flows, respectively) for each steady-state flow rate. Values are further compared to assess if the pipe can be considered hydraulically smooth. The seven steady-state flow rates used to calibrate the model are presented in Table 5.3. Transitional flows are not considered.

Table 5.3. Steady-state flows for friction calibration

Q_0 (lh^{-1})	Re (-)	Experimental f	Theoretical f
47.8	845	0.276	0.0757
76.5	1352	0.131	0.0473
342.4	6054	0.0596	0.0359
424.5	7506	0.0779	0.0339
550.4	9733	0.0463	0.0319
700.7	12391	0.0428	0.0299
882.7	15609	0.0342	0.0283

Theoretical and experimental friction factor results are compared in Figure 5.1. A high discrepancy is identified for laminar flows. However, as the flow rate increases, a better fit is obtained and Blasius friction formulation becomes progressively more accurate. This discrepancy is due to the continuous head loss being between the accuracy range of the transducers (0.30 m). As flow rate increases, head loss gets higher until the pressure head loss outreaches the pressure transducers accuracy span. From that steady-state flow rate onwards, data have much less uncertainty and become more representative of the observed phenomenon. For further researches, it is recommended the assembly of a transducer at the upstream reach of the system, increasing the piezometric difference between the data collection points.

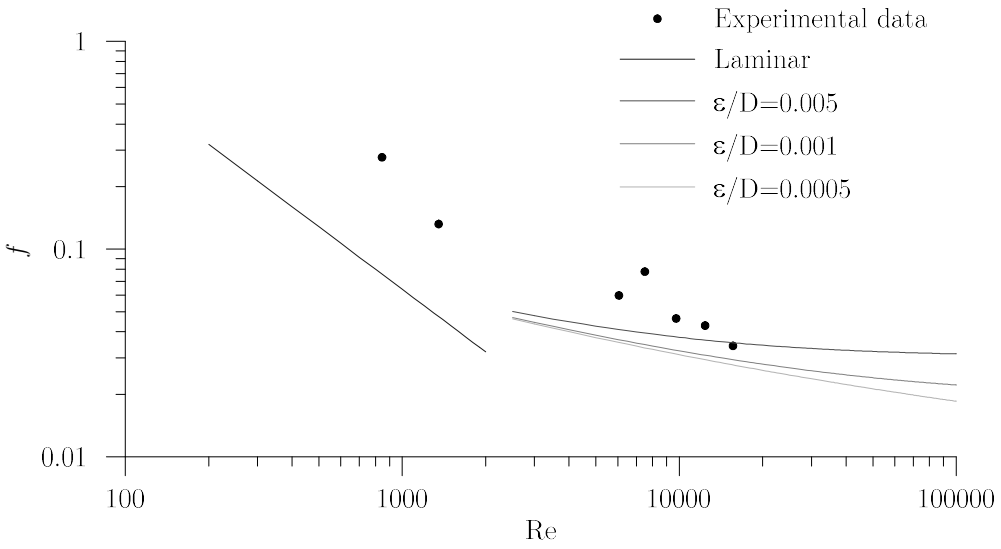

Figure 5.1. Experimental and theoretical friction factor comparison

5.3.3 Valve manoeuvre establishment

The two developed approaches to characterize the valve behaviour in Chapter 4 (i.e., the in-line valve and the valve discharge to atmosphere) are considered and analysed to assess the best formulation that describes the valve closure law. These approaches are defined as a function of the closure angle for each

initial flow rate (*cf.* Table 4.2 and Table 4.3). Thus, a relation is obtained between time and the flow rate at the valve at each closure instant considering a linear valve closure.

Obtained results using each of the two methods are depicted in Figure 5.2. The valve law that better fits experimental data is the second one (i.e., the one obtained for the valve discharging to atmosphere). This is because the returning is neglected in the numerical model and the pressure downstream the valve is considered constant. When using the first approach law (for the in-line valve), this results in an abrupt closure, hyperbolic shape, which does not accurately fit experimental data. Despite the real valve behaviour being described by the in-line valve law, the numerical simplifications introduced in the model require that this valve is described by the discharging to atmosphere law.

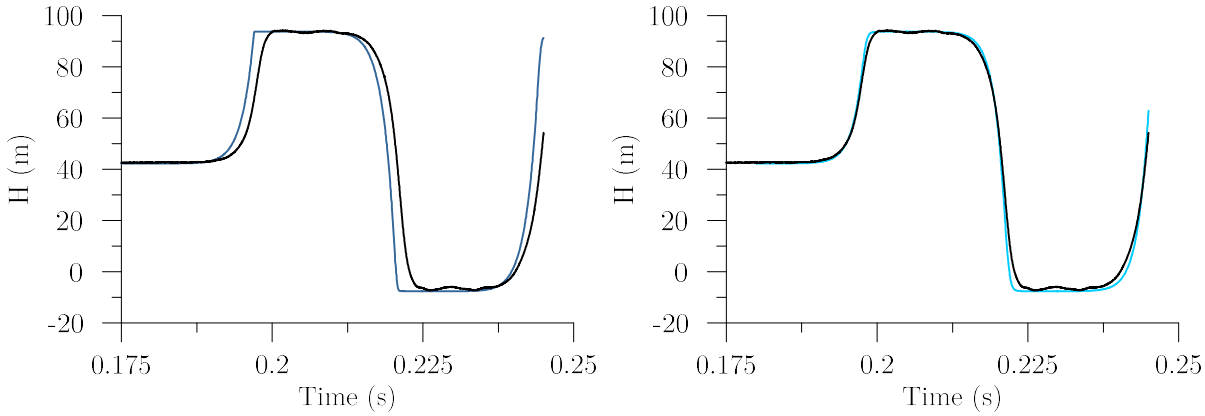

Figure 5.2. Pressure at the valve using both approaches: (a) hyperbolic manoeuvre; (b) sigmoid manoeuvre (black – experimental; blue – numerical results).

5.4 Numerical results

5.4.1 Classic transient solver approach

Friction formulations are usually split in quasi-steady and unsteady-state friction losses. Usually commercial water hammer models only consider the quasi-steady friction loss to determine energy dissipation during the transient event. However, the unsteady component has a major relevance for fast transient events due to the phenomenon described in Figure 2.4.

For this reason, experimental data and pressure using a quasi-steady friction approach at the valve are depicted in Figure 5.3 for the initial flow rate 450 lh^{-1} test. The first pressure peak has a clearly good fitting to experimental data. However, in the following pressure wave periods a great difference is observed between both results. These differences are due to the energy dissipation by viscous forces (Wahba, 2008) and a vortex sheet phenomenon when a valve shuts (Martins *et al.*, 2016).

With such pressure decay, the time between two steady-state conditions is greatly reduced. This is especially important for hydraulic systems operation rules.

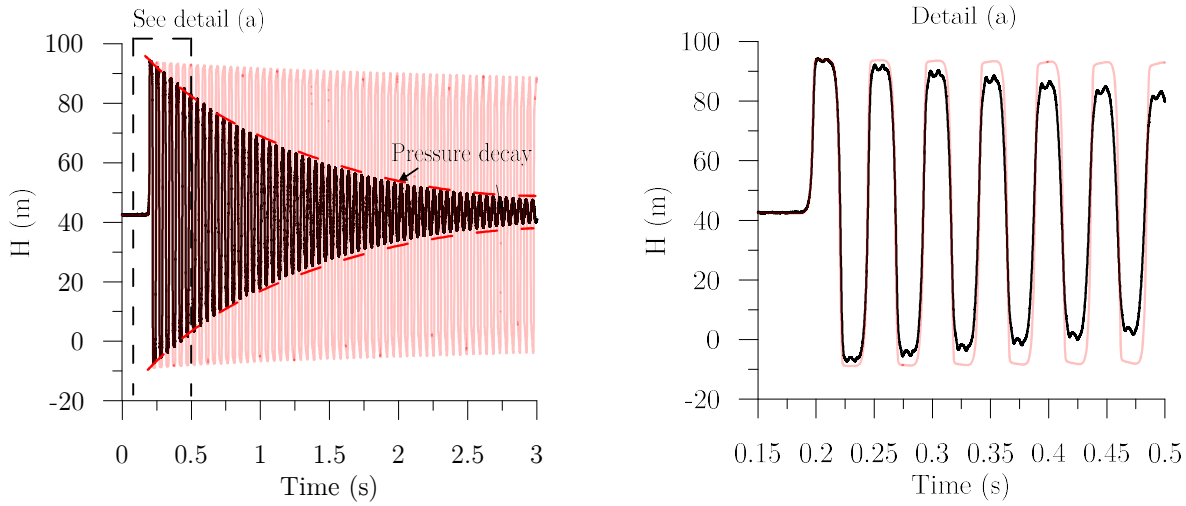

Figure 5.3. Comparison between experimental data and results from the classic model at the valve for 450 lh^{-1} (black – experimental; red – numerical results).

5.4.2 Unsteady friction modelling for turbulent flows

For the sake of simplicity in the following sections, Brunone et al. (1991), Ramos *et al.* (2004), Zielke (1968), Trikha (1975) and Vardy and Brown (2003) unsteady friction models will be analysed, hereinafter, simply referred to as Brunone, Ramos, Zielke, Trikha and Vardy models.

Instantaneous acceleration-based and convolution-based models are used to assess results from the developed numerical model with steady-state turbulent transient event.

Instantaneous acceleration-based models (Brunone and Ramos) results are compared in Figure 5.4, both for end-section (valve) and mid-section. The decay coefficient k_s that better characterizes experimental data for Brunone's formulation is 0.016. The better shape and decay coefficient from Ramos formulation are k_x and k_t equal to 0.02 and 0.026, respectively.

Relaxation coefficient θ (see Table 5.1) weights the local acceleration with the previous velocity and the value that leads to better results is zero for Brunone's formulation and no instabilities are observed for the used parameter. This should be unitary for Ramos formulation.

Brunone's formulation gives a good fit with experimental data with the proposed valve closure law. Pressure peaks are well described and the energy dissipation is accurately characterized. A slight pressure wave shift is noticed after two wave periods, which may be due to the chosen decay coefficient.

Ramos's also gives a good fitting with experimental data in what concerns pressure peaks and decay. However, the previously identified pressure wave shift does not occur as the coefficients for local and convective accelerations are specifically calibrated for pressure decay and wave shift.

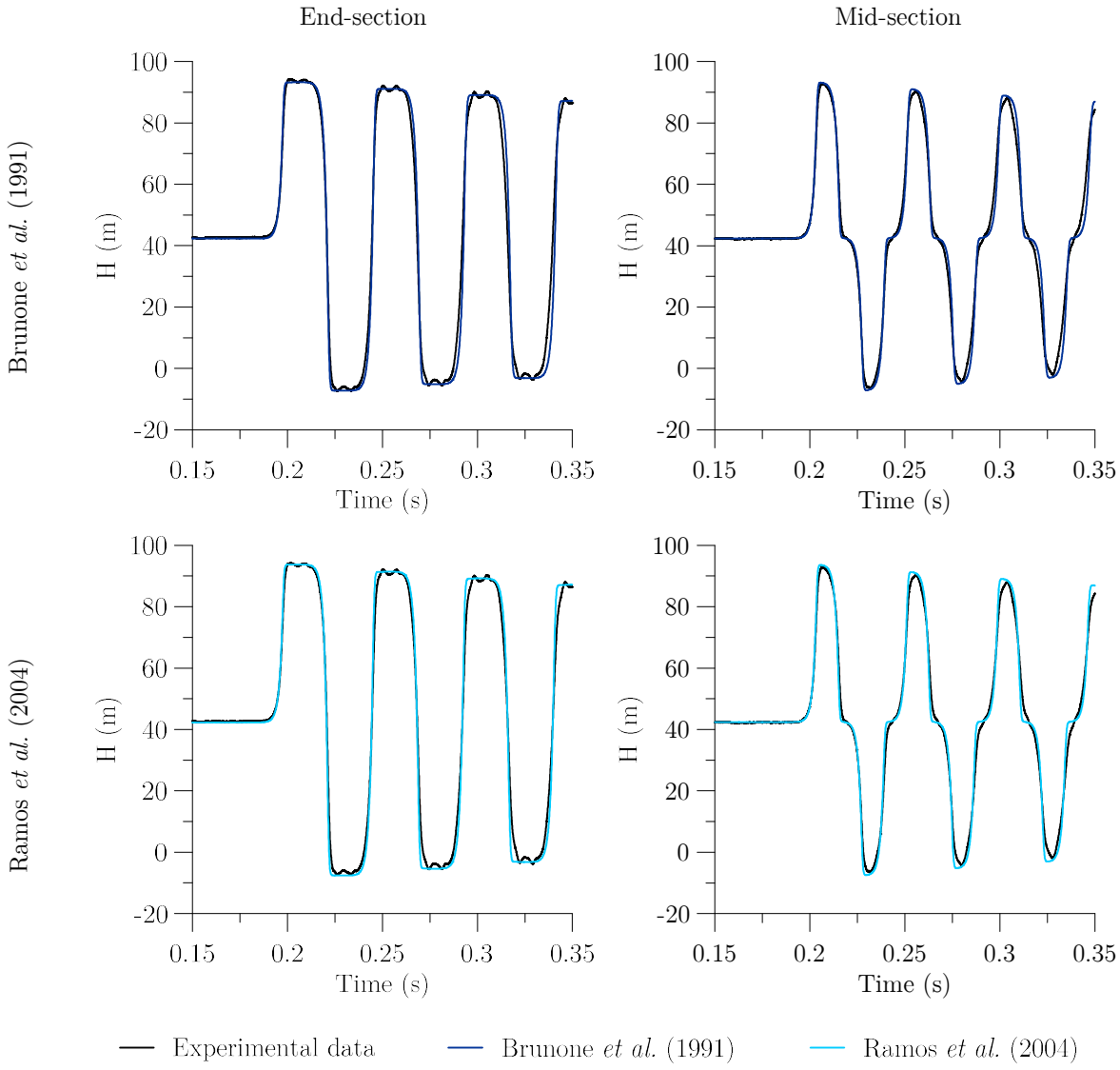

Figure 5.4. Comparison between 450 lh^{-1} test experimental data and instantaneous acceleration-based models

The comparison between the convolution-based model results and the experimental data is depicted in Figure 5.5 at pipe end and at pipe mid-section.

Zielke's formulation results describe reasonably well experimental data. Despite Vardy and Brown (1995) advise against Zielke's model application outside laminar flow regime, this formulation can be applied according to Ghidaoui and Mansour (2002) as the duration between wave pulses gets smaller.

Trikha's results accurately describe pressure wave peaks. However, pressure variations are more pronounced than Zielke's due to an approximate weighting function usage. This issue will be furtherly address in a time-step analysis.

Vardy's unsteady friction formulation has very similar results to Zielke's as all previous past accelerations are considered. Weighting functions considered for each formulation are considerably close to one another as the Reynolds number of the tested flow is small. Pressure decay is accurately described and a smoother pressure transition is obtained rather in instantaneous acceleration-based models.

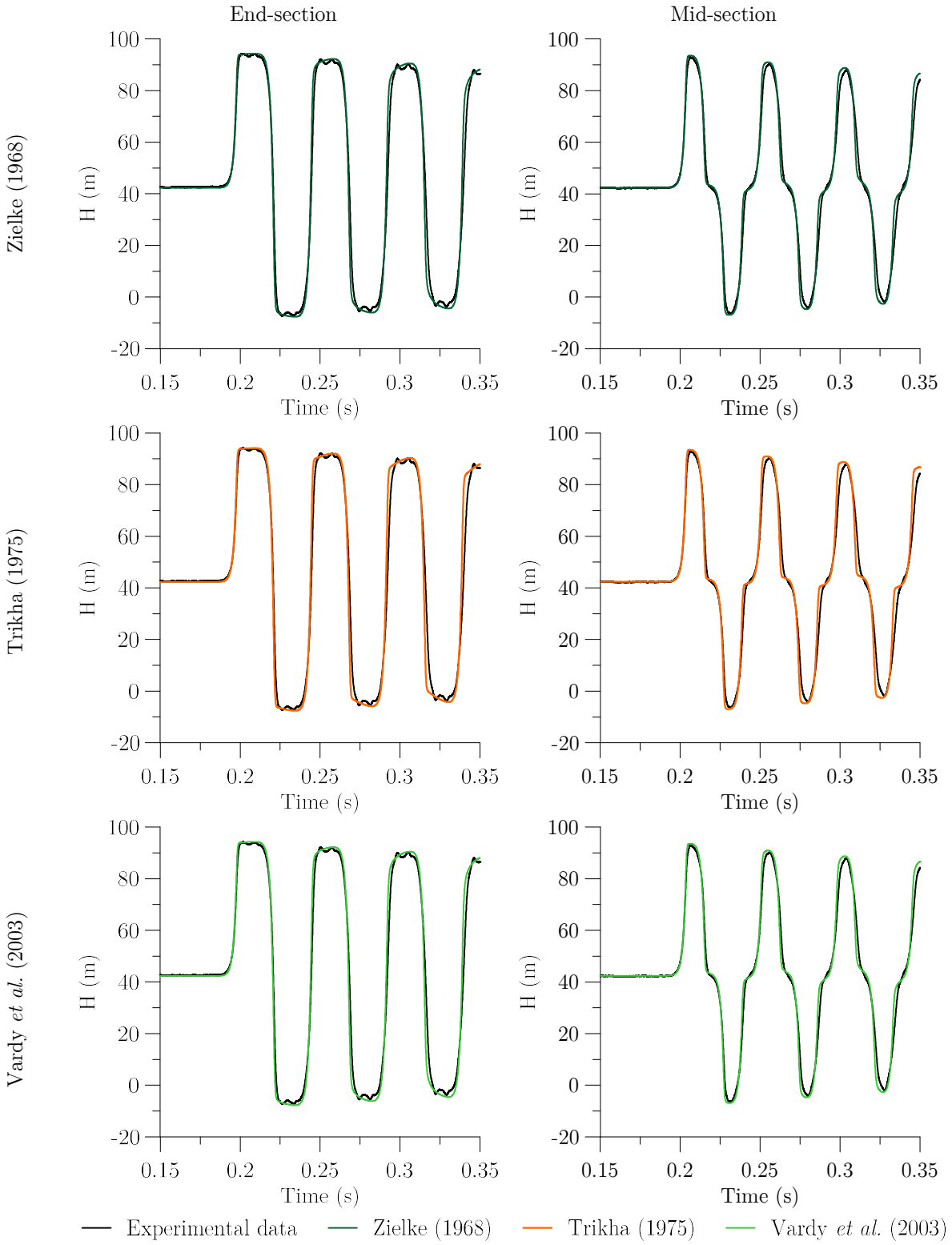

Figure 5.5. Comparison between 450 lh^{-1} test experimental data and convolution-based models

5.4.3 Unsteady friction modelling for laminar flows

Instantaneous acceleration-based models results are compared with steady-state laminar flow transient event ($Q_0 = 56.5$ lh^{-1}) in Figure 5.6.

Decay coefficients mentioned in turbulent flow results are used as they are intrinsic to the system. A good fitting is observed for the first pressure peak in all unsteady friction formulations. Despite the accurate characterization of the valve manoeuvre, a sharp transition is observed between pressure variations. This effect is due to the viscous component of shear in unsteady-state flows not being accurately merely described by past flow accelerations.

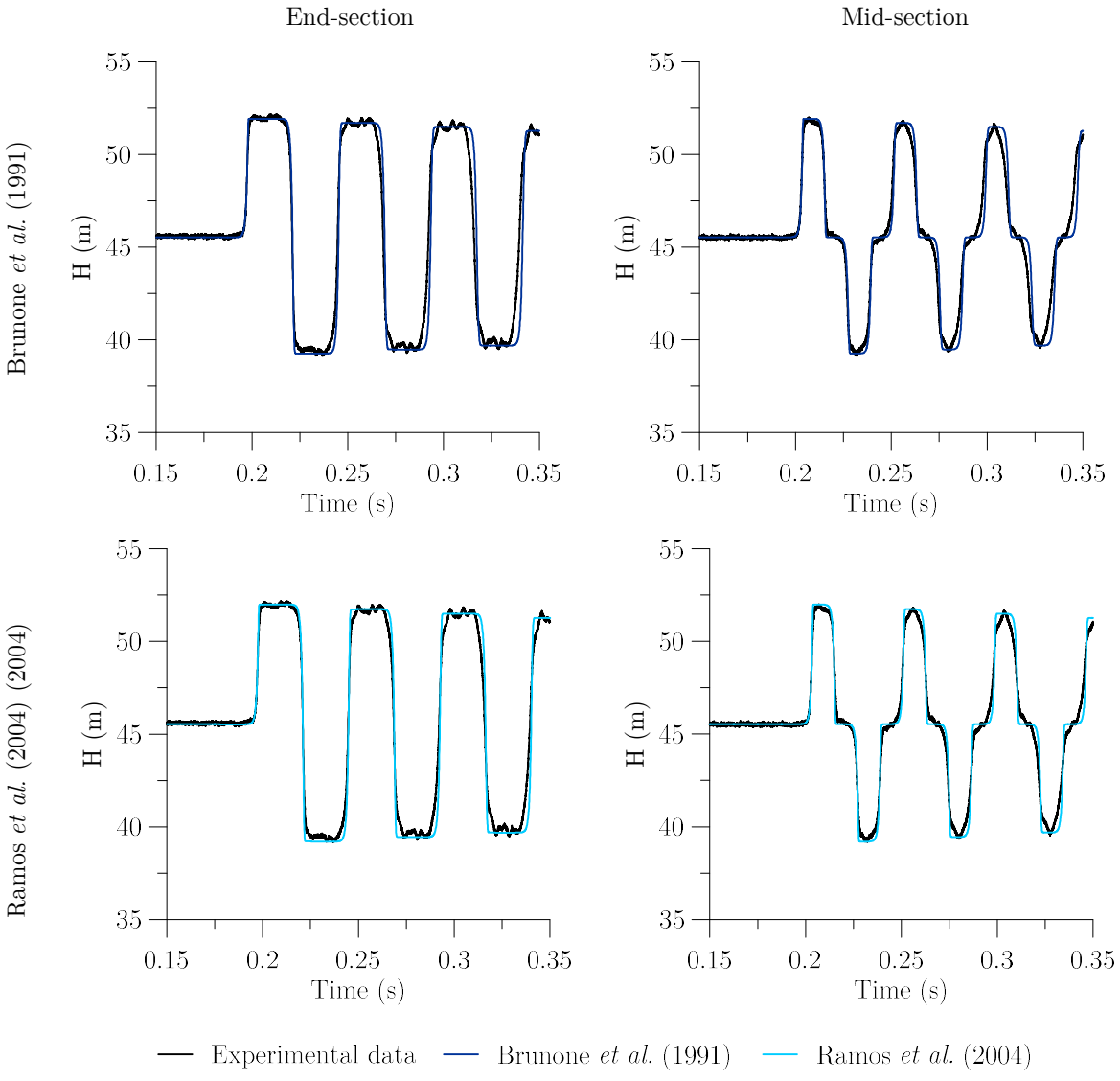

Figure 5.6. Comparison between 56.5 lh^{-1} experimental data and instantaneous acceleration-based models

Convolution-based models' (Zielke, Trikha and Vardy) results are compared with experimental data in Figure 5.7, for a 56.5 lh^{-1} initial flow rate. Zielke's formulation presents a good fitting, as expected. Trikha's formulation gives good results but discrepancies are observed for inflexion points. This issue is discussed in the next sub-section as this is due to the numerical time-step. Vardy's model results are the same as Zielke's formulation, as the used weighting function tends to Zielke's.

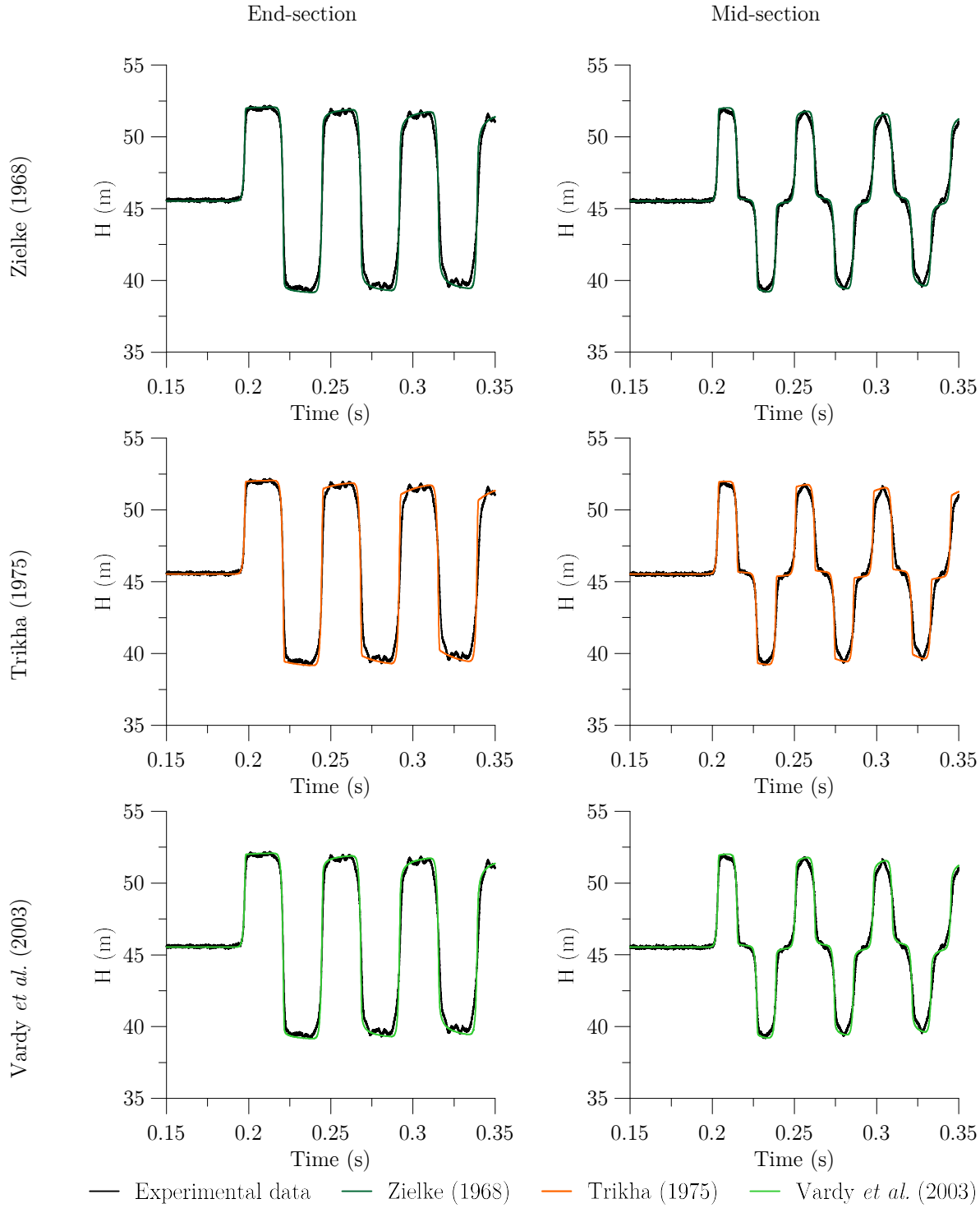

Figure 5.7. Comparison between 56.5 lh^{-1} experimental data and convolution-based models

5.4.4 Time-step analysis

Unsteady friction models are highly time-step (Δt) dependent models. This issue is especially relevant for convolution based models as the integral of the weighting function gets rougher results with higher time-steps due to the first weighting value considered. Zielke formulation is subjected to the following time-steps: 1.10^{-3}, 5.10^{-4} and 1.10^{-4} s. Results are depicted in Figure 5.8. Pressure is accurately estimated and a higher pressure wave delay can be observed as the time-step increases for both unsteady friction formulations. The smaller the time step is, the more accurate the numerical results become.

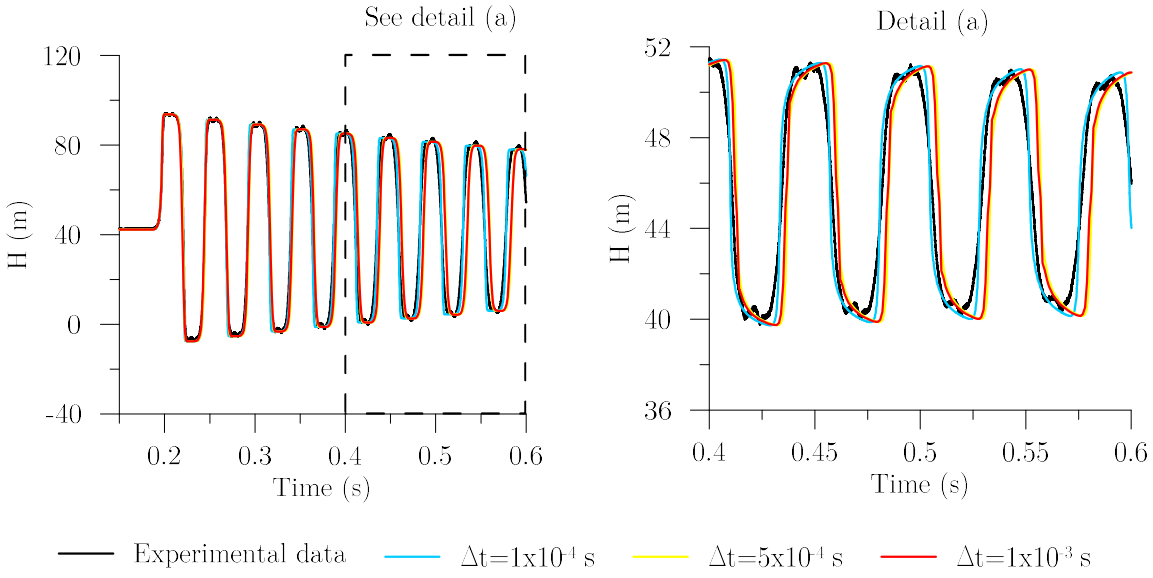

Figure 5.8. Time-step dependent analysis for Zielke formulation with 450 lh^{-1} test.

Another relevant issue is Zielke's and Trikha's weighting functions, depicted in Figure 5.9. For the time-step considered in this research (5.10^{-5} s), a $\Psi = 5.10^{-7}$ non-dimensional time is obtained. This value is lower than non-dimensional time of 1.10^{-4}, which is the maximum recommended for Trikha's formulation to be accurate. For smaller non-dimensional times Zielke's weighting function reaches much higher values, which leads to much more smoother pressure waves (without sharp edges). Thus, edges/inflection zones can be identified in Trikha's formulation in comparison with experimental data and Zielke's formulation, as previously mentioned (Figure 5.7).

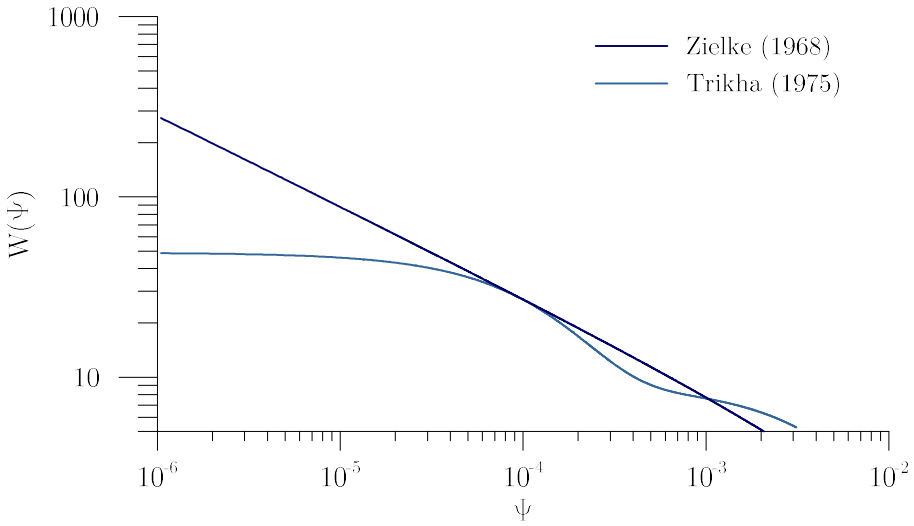

Figure 5.9. Zielke (1968) weighting function and Trikha (1975) approximate weighting function

5.5 Final remarks

Wave celerity was theoretically obtained and compared to the one obtained experimentally; very similar values were obtained (1256.5 ms^{-1}). Steady-state friction and valve closure manoeuvre were calibrated leading to reasonably good results for Blasius formulation.

Instantaneous acceleration-based and convolution-based models were compared with experimental data, both for different flow regimes. For turbulent flows, instantaneous acceleration-based models and convolution-based models give a good fitting with experimental data. For laminar flows, a better fit was obtained for convolution-based models.

A time-step analysis was carried out and a pressure wave delay was identified for higher time-steps (i.e., $\Delta t > 10^{-4}$ s). Using non-dimensional time steps lower than 10^{-4} in Trikha unsteady friction formulation leads hardly changes the obtained results, whereas when used in Zielke formulation leads to much more accurate results in comparison with experimental data.

Chapter 6 | Wall shear stress analysis

6.1 Introduction

In the present chapter, constant temperature anemometry technique is used to measure wall shear stress during water hammer events. Hot-film calibration is carried out according to Keller and Wilkinson (2002) and a calibration curve is obtained. Experimental data are compared with numerical results from the previously described model for instantaneous acceleration based and convolution based unsteady friction formulations. CFD results are used herein to compare with experimental data in order to better understand the cause of observed discrepancies between measurements and numerical results. A comparison between CFD and 1D model wall shear stress results is carried out and the sensor position is determined according to the velocity profiles during steady-state flows. At last, the MiniCTA response is analysed and conclusions are drawn for the usage of this equipment in this kind of events.

6.2 Procedure description

6.2.1 Equipment assembly

As the pipe system is pressurized, special care must be taken with leakage from the stainless steel box and the possibility to the vapour bubbles creation around the hot-film. Thus, an indentation was created with probe thickness inside stainless steel box in order to glue it evenly on the surface and to minimize the gap as much as possible. Wires from the probe are accessible through holes in the structure itself, connecting to the MiniCTA. The installed steel box is not levelled for the probe not to have interferences with eventual air bubbles within the flow. The stainless steel box is shown in Figure 6.1.

Figure 6.1. Assembled wall shear stress measurement structure

6.2.2 Data calibration

Data collected by the constant temperature anemometry requires a specific calibration in order to obtain wall shear stress. First, the wall shear stress is highly viscosity dependent, hence fluid temperature dependent. Tests were carried out one hour after the system start-up, after the water temperature having stabilized.

An extensive amount of steady-state flows are tested to determine the calibration curve. For each steady-state flow rate, voltage from the MiniCTA is collected. According to Admiraal (1997), the relation between wall shear stress and the output voltage signal from the constant temperature anemometer is

$$E^2 = A\tau^{\frac{1}{m}+B} \tag{6.1}$$

in which E is the output probe voltage, A and B depend on the sensor resistance and dimensions, fluid properties, temperature difference and heat losses. Coefficient m depends on the thermal conductivity between the fluid and the pipe (Menendez and Ramaprian, 1985).

A constant temperature friction factor is obtained for each flow rate based on Blasius and on Hagen-Poiseuille friction formulations, depending on Reynolds number. Thus the steady-state wall shear stress is theoretically calculated according to Eq.(6.2), assuming that the glue-on probe is inside the viscous sub-layer.

$$\tau = \gamma R_H h_{fs} \tag{6.2}$$

in which R_H is the hydraulic radius, that is equal to $D/4$ in pressurized circular pipe. The MiniCTA output voltage and the corresponding theoretical wall shear stress as function of the steady-state flow rate are shown in Figure 6.2.

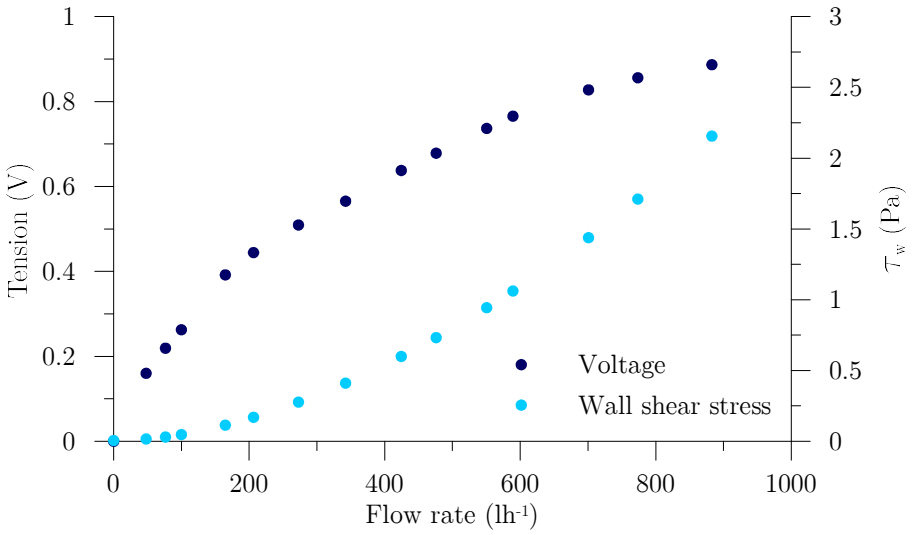

Figure 6.2. Calibration voltage and wall shear stress with flow rate

The calibration curve that relates wall shear stress and the output voltage from the MiniCTA is presented in Figure 6.3. The obtained curve is characterized for being a 7th grade polynomial function, as for a smaller polynomial degree, shear value would be negative due to the lack of information in laminar flows:

$$\tau_w = 0.98V - 17.99V^2 + 135.03V^3 - 484.51V^4 + 930.72V^5 - 875.74V^6 + 321.98V^7 \quad (6.3)$$

in which V is the provided tension from the MiniCTA. Thus, a good fitting is obtained between the voltage and the theoretical wall shear stress.

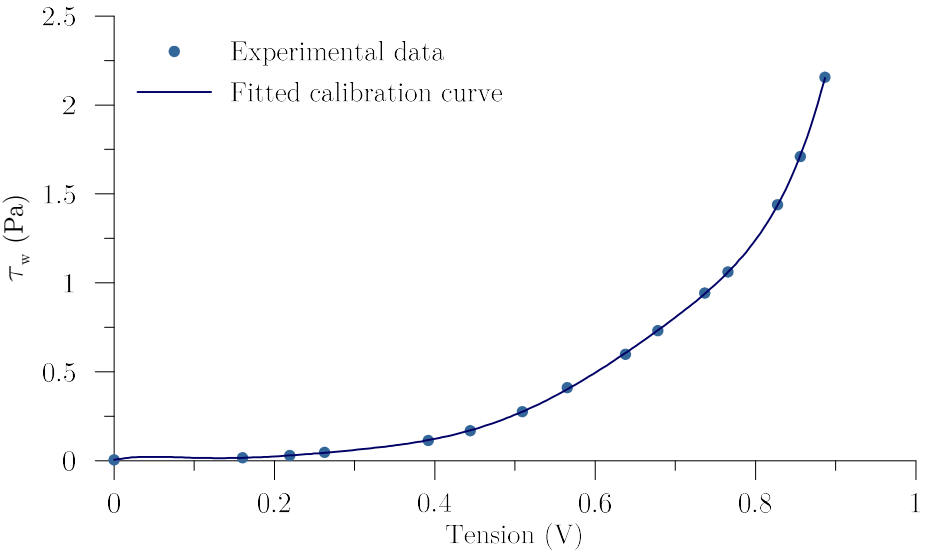

Figure 6.3. Calibration curve between voltage and wall shear stress

A relevant issue is that when steady-state wall shear stress is being measured, fluctuations can be observed in the collected signal. A non-dimensional wall shear stress, defined as $\tau / \bar{\tau}$, in which τ is the instantaneous wall shear stress and $\bar{\tau}$ is the sample mean wall shear stress, is used for depicting these fluctuations in Figure 6.4. A reason for those is the fluctuating velocity component in turbulent flows, which is inexistent in laminar flows.

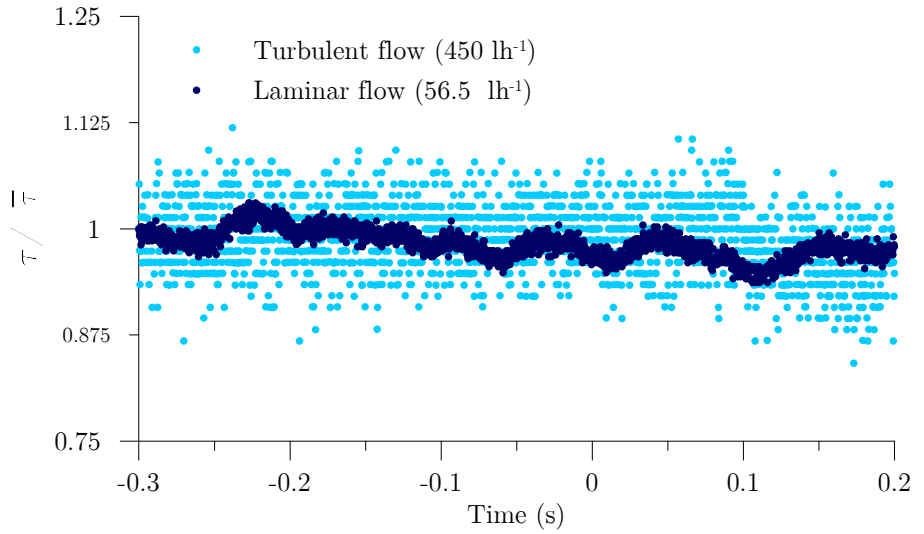

Figure 6.4. Laminar and turbulent steady-state measured wall shear stress

6.3 Experimental data considerations

The wall shear stress can be obtained based on the application of the calibration curve to the MiniCTA measurements (i.e., output voltage). Wall shear stress comparisons must be carried out for absolute τ_w values since the MiniCTA device does not identify the flow direction but quantifies only rates of heating (the higher the velocity gradient is, the higher the measured rate of heating becomes).

Experimental wall shear stress for both tests Q_0= 450 lh^{-1} and Q_0= 56.5 lh^{-1} are depicted in Figure 6.5.

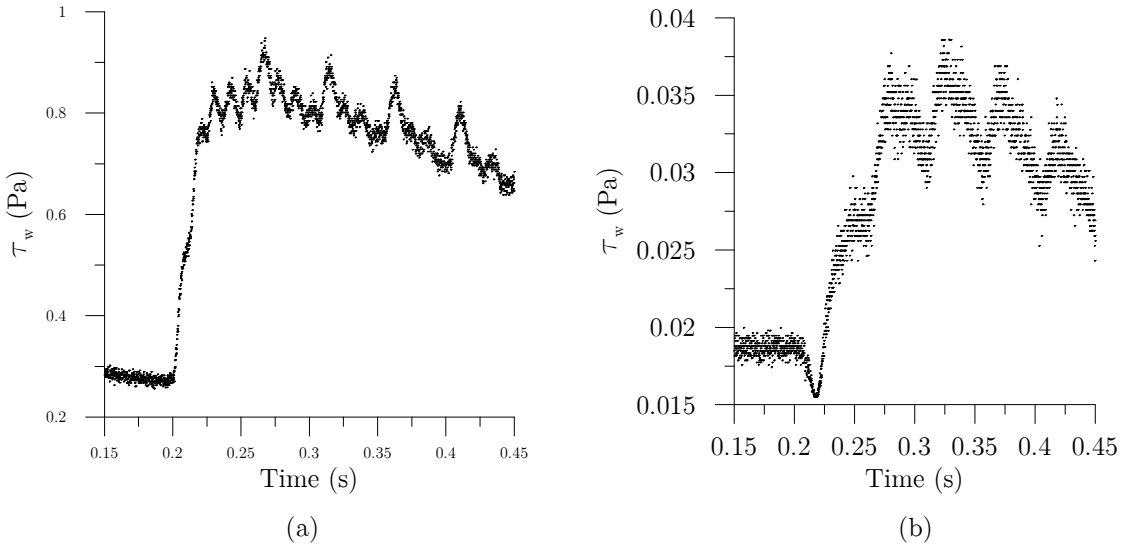

Figure 6.5. Experimentally obtained wall shear stress for tests: (a) Q_0= 450 lh^{-1} and (b) Q_0= 56.5 lh^{-1}

Wall shear stress increases as the sensor begins to identify a flow reversal. This is characterized by a slight step in the first wall shear stress rise, maybe due to null flow, increasing afterwards during the total flow reversal. The same step occurs when the flow is expected to be zero during pressure wave travel. These are the oscillations in wall shear stress after the first peak.

Wall shear stress progressively reduces until a null value is obtained, as long as the probe continues to register heat transfer. However, no null wall shear stress values are obtained when the flow rate is expected to be null. One possible explanation for this unexpected behaviour is the continuous heating need to balance the sensor and the water temperatures. Another possible explanation is that when a water hammer event occurs, the thermal boundary layer reverses similarly to the velocity profile being the same amount of water continuously heated until thermodynamic equilibrium is achieved. A thermal boundary layer is illustrated in Figure 6.6.

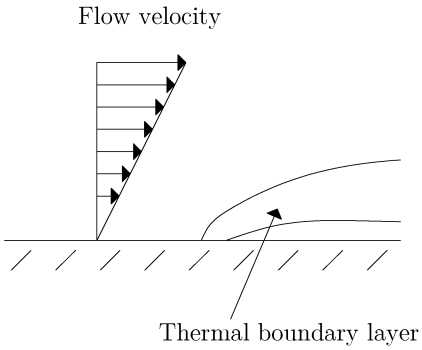

Figure 6.6. Scheme of the thermal boundary layer

Pressure variation is compared with wall shear stress for both initial flows Q_0= 450 lh^{-1} and Q_0= 56.5 lh^{-1} in Figure 6.7. A delay is observed between pressure and wall shear stress variation. This effect may be due to equipment delay between temperature reading and the sensor heating. Frequency data output cannot assure the probe is supplied with the same time interval and with a necessary frequency for the phenomenon characterization. This time delay tends to increase as the number of electric connections' and cables' lengths increase. This issue was not reported by Ariyaratne *et al.* (2010) and He *et al.* (2011) in purely accelerating and decelerating flows, when using the same technology for measuring the wall shear stress.

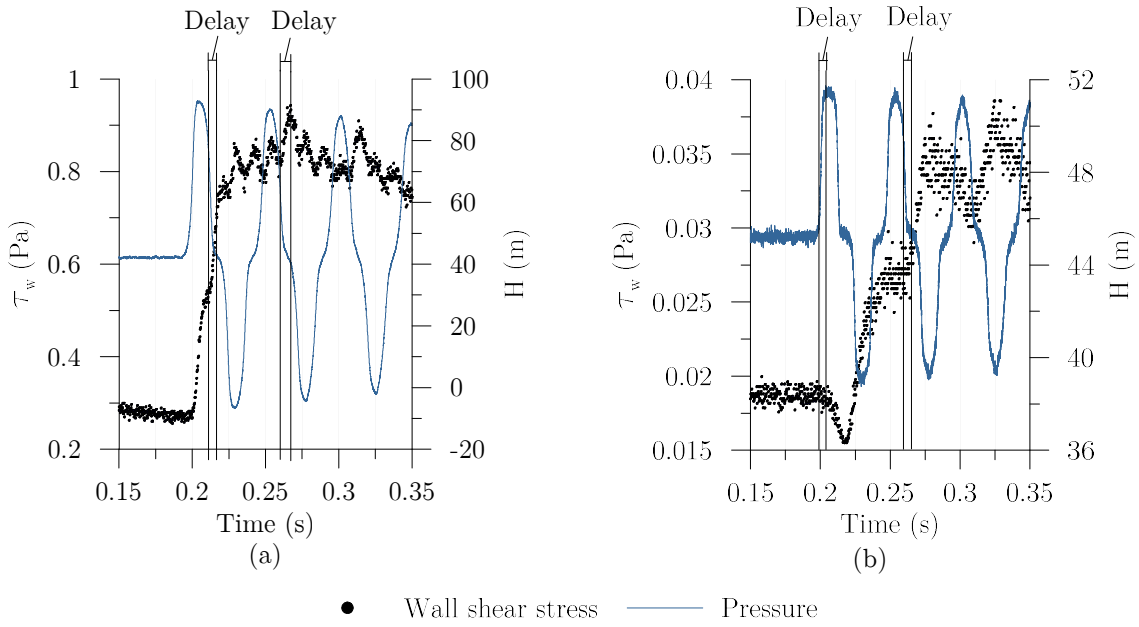

Figure 6.7. Experimentally obtained wall shear stress and pressure at mid-section for steady-state flows: (a) Q_0= 450 lh^{-1} and (b) Q_0= 56.5 lh^{-1}

6.4 Experimental data and numerical model comparison

6.4.1 One-dimensional model results: laminar flow

The comparison between the wall shear stress measurements for Q_0= 56.5 lh^{-1} test and numerically obtained results for two convolution-based models is depicted in Figure 6.8. Wall shear stress peaks obtained in the numerical models do not fit experimental data. Steady-state wall shear stresses fit reasonably well in the numerical model and the measurements, being obtained $\tau_w = 0.17$ Pa. Energy dissipation (behaviour out of peaks) is also not accordingly to experimental results.

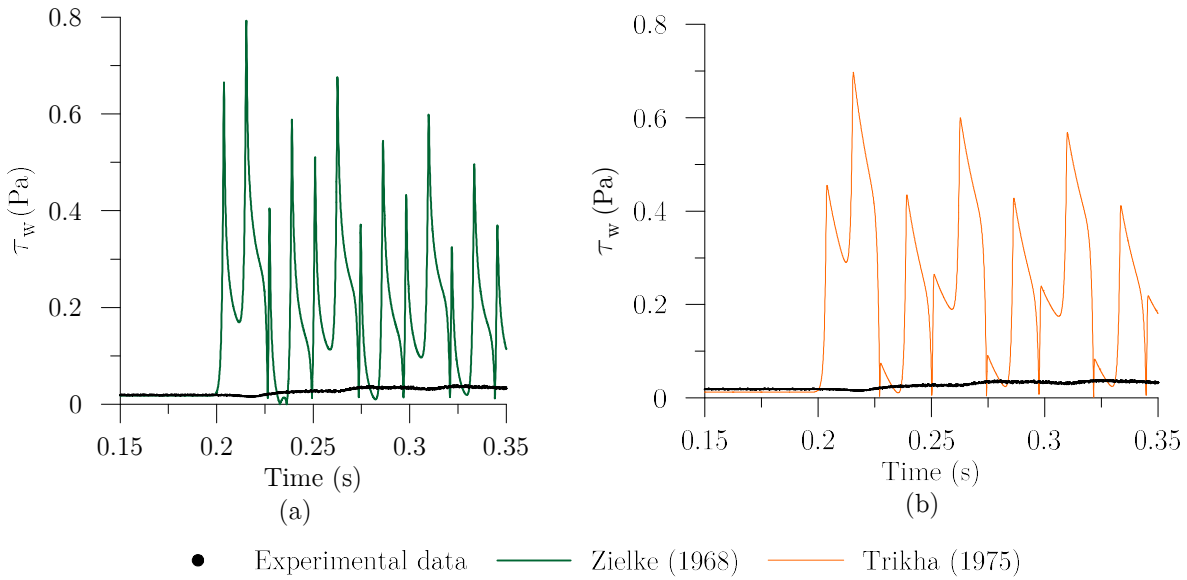

Figure 6.8. Experimental wall shear stress comparison with convolution based model for Q_0= 56.5 lh^{-1}: (a) Zielke and (b) Trikha

6.4.2 One-dimensional model results: turbulent flow

Results from the instantaneous acceleration-based unsteady friction models are compared with experimental data for Q_0= 450 lh^{-1} in Figure 6.9. Numerical and experimental steady-state wall shear stresses are significantly different, being the measured wall shear stress (0.30 Pa) lower than the numerical (0.66 Pa). A possible reason for this difference is the sensor not being installed inside the viscous sub-layer. If that is the case, the closer the sensor is to the flow core, the more relevant inertial forces are and the smaller shear stress becomes. This could also be a reason for the behaviour observed in the Figure 6.4. None of the wall shear stress models is capable of describing the observed wall shear stress.

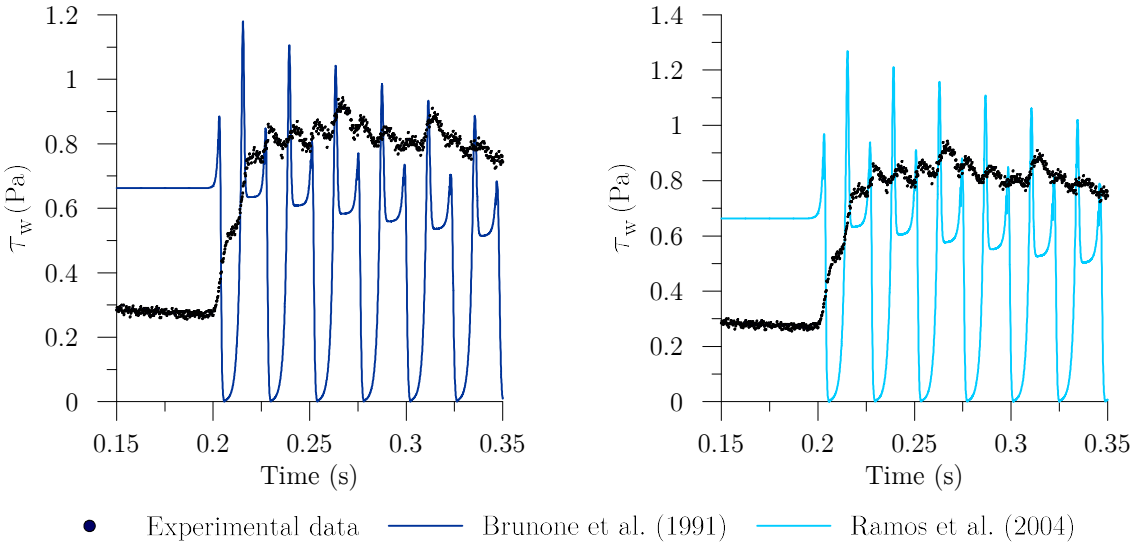

Figure 6.9. Experimental wall shear stress vs results from the instantaneous acceleration-based models for Q_0= 450 lh^{-1}.

Results from the convolution-based unsteady friction models are compared with experimental data in Figure 6.10. Steady-state experimental wall shear stress is much lower than the numerically obtained wall shear stress once more. Neither Zielke (1968) nor Vardy and Brown (1995) formulations accurately describe experimental data. This strengthens the conclusion that the sensor may not be located inside the viscous sub-layer, or an uncertainty exists in the sensor calibration curve.

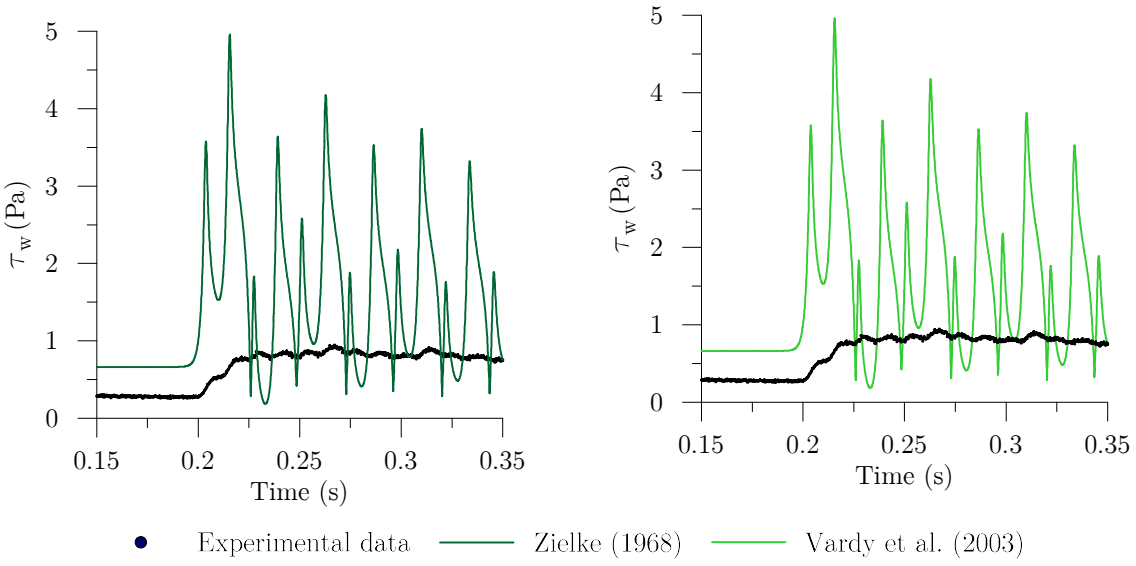

Figure 6.10. Experimental wall shear stress vs results from the convolution-based models for Q_0= 450 lh^{-1}

6.4.3 1D and CFD models wall shear stress results

Since the 1D model results do not agree with the measurements, wall shear stress was obtained from a CFD test for $Q_0 = 450$ lh^{-1}. The used CFD setup and the system characteristics are described in 4.5. The comparison of the wall shear stress results from CFD model and Zielke UF model are depicted in Figure 6.11. Wall shear stress behaviour is the same in both models, regardless the wall shear stress peaks being slightly underestimated in 1D modelling. This shows that the 1D model have accurately results comparing with the ones from the CFD model.

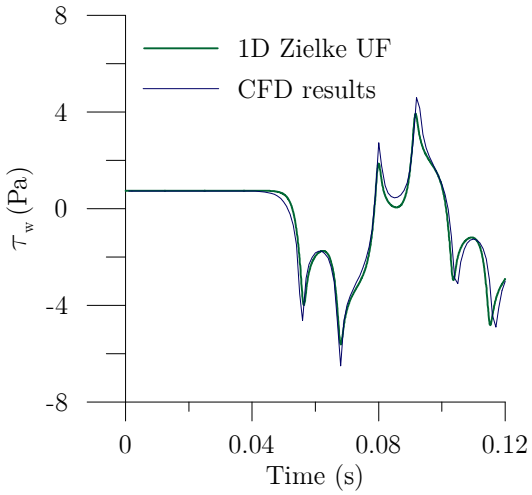

Figure 6.11. 1D and CFD wall shear stress results for Q_0= 450 lh^{-1}

Local velocities are obtained from the described CFD model for flow rates between 55 to 1679 lh^{-1} (Reynolds numbers from 973 to 35600). This is useful to assess at what distance the sensor could be from the wall. This analysis is made for steady-state conditions.

The shear stress has two main components - a viscous component and a turbulent component – described by Eq.(2.34):

$$\tau(r) = \tau_v + \tau_t \qquad \therefore \qquad \tau(r) = -\mu \frac{\partial V}{\partial r} + \rho \overline{u' v'} \tag{6.4}$$

Results from CFD numerical simulations allow the estimation of an approximate value of the viscous shear stress based on the velocity gradient along the pipe axis:

$$\tau_v(r_i) \approx -\mu \frac{V_i - V_{i+1}}{r_i - r_{i+1}} \tag{6.5}$$

Considering that the shear stress varies linearly between the maximum value at the wall, τ_w, and the null shear stress in the pipe axis, and knowing the approximate value of the viscous component given by Eq.(6.4), the turbulent shear component can be estimated. The total shear stress, the viscous and the turbulent components are depicted in Figure 6.12 for both laminar and turbulent flows. The viscous component is maximum at the pipe wall ($r = D/2$) and null at the pipe axis ($r = 0$); the turbulent

component does not exist in laminar flows and, in turbulent flows, is null both at the wall and at the pipe axis, having a maximum value in-between.

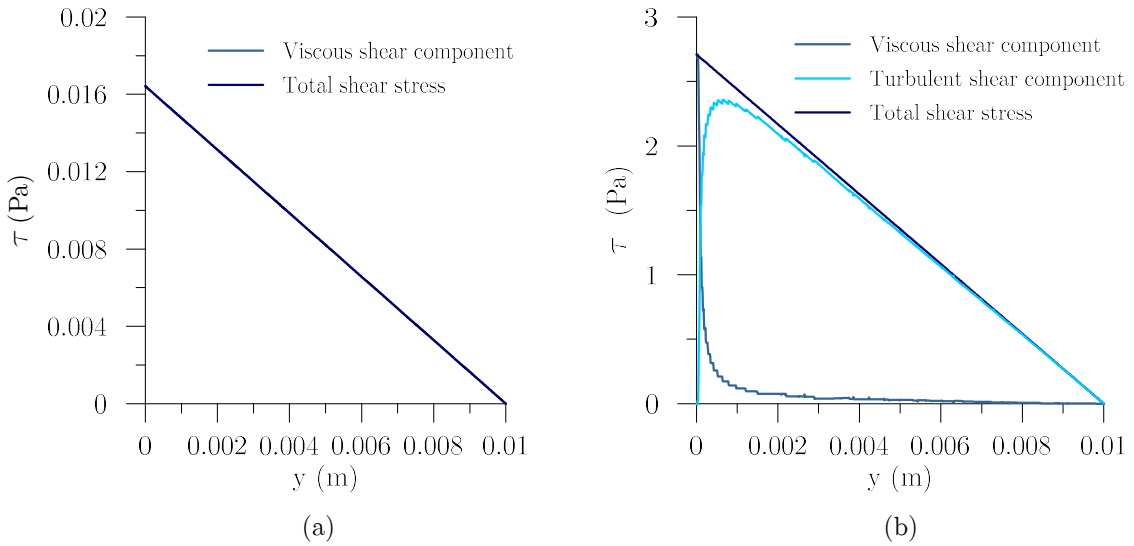

Figure 6.12 Shear stress distributions obtained by CFD for: (a) laminar flow (Q_0= 56.5 lh^{-1}) and for (b) turbulent flow (Q_0= 450 lh^{-1})

As referred, the measured wall shear stress is approximately half the value calculated in 1D and CFD models (see Figures 6.9 and 6.10). This may indicate that the hot-film sensor may not be exactly aligned with pipe wall and is measuring the shear stress at an unknown distance from the wall. For the initial flow Q_0= 450 lh^{-1}, the measured wall shear stress is 0.30 Pa and the calculated by 1D and CFD models is 0.66 Pa.

To estimate the sensor location, wall shear stress measurements from steady-state tests were used and analysed. The CFD model was run for each flow rate and velocity profiles were calculated for steady-state conditions. The probe location was estimated based on the measured wall shear stress and on calculated CFD velocity profiles, using Eq.(6.5). This location was compared with the viscous sub-layer thickness, δ^*, obtained by (Schlichting, 1979, Cardoso, 1998, Brunone and Berni, 2010):

$$\delta^* = \frac{11.6\nu}{u^*} \tag{6.6}$$

in which u^* is the friction velocity defined in Eq.(2.27). Estimated sensor distances from the wall and viscous sub-layer thicknesses for each flow rate are depicted in Figure 6.13. For turbulent flows (Re>4000), the sensor distance from the wall is lower than the viscous sub-layer thicknesses, which means that the sensor is installed inside this sublayer whose thickness decreases with the Reynolds number, as expected. For laminar flows however (Re<2000), the opposite results are obtained and the estimate sensor position seems to be outside the viscous sub-layer, which is incoherent with the previous result, as δ^* is supposed to increase for lower flows. This result can be due to uncertainties in the sensor calibration for lower flows.

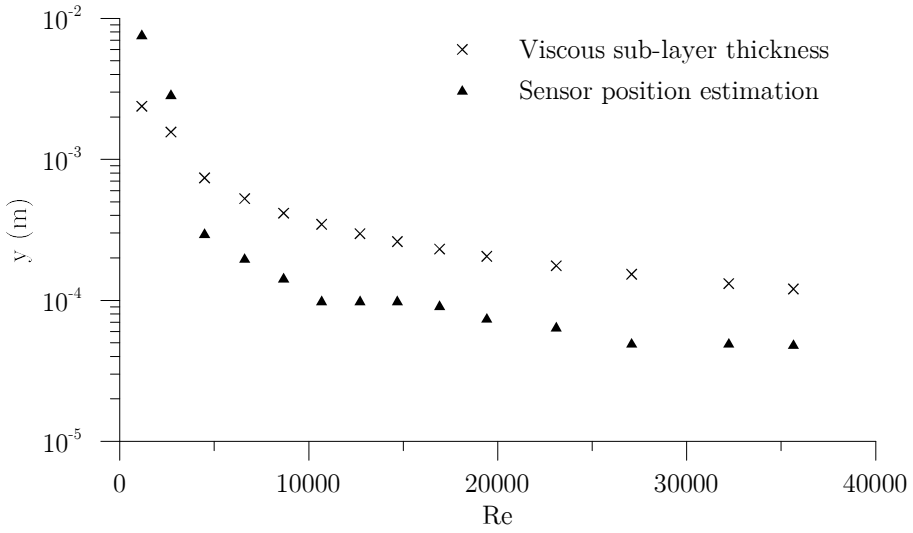

Figure 6.13. Variation of the probe distance from the wall and of the viscous sub-layer thickness with the flow rate

6.4.4 MiniCTA response

As measurements are carried out within the viscous sub-layer and the 1D numerical model gives reasonably accurate results, the MiniCTA response is analysed in order to understand the observed discrepancies. The equipment increases and reduces the provided current to the probe whenever needed, with its own heating frequency. However, this frequency may not be as high as the necessary for the unsteady wall shear stress characterization. Measurements would have relatively the same shape in time, if the sensor heating frequency were smaller or equal than the event frequency. However, if the MiniCTA had a lower heating frequency, the required current would not be immediately provided as the received signal at the MiniCTA

takes time to "travel" between the equipment and the probe, measurements would be much smoother and previous instances would interfere with the emitted signal reducing wall shear stress measurements; the same happens when flow rate is theoretically null as this situation is not identified in the carried out measurements.

Wall shear stress tests with initial flow rates of 450 and 56.5 lh^{-1} were analysed for different time delays (t_d) comparing with the corresponding Zielke's results from the 1D model. A moving average with a pre-determined amount of time is calculated for each model results. The wall shear stress measurements and the corresponding Zielke's moving averages are presented in Figure 6.14.

For the initial flow rate of 450 lh^{-1}, a shape match is obtained for the moving average with a time delay of 0.0025 s in the wall shear stress rise. Further variations may be due to thermal inertia to the flow and measuring differences, as the sensor is not perfectly aligned with the wall, despite being in the viscous sub-layer.

For the initial flow rate of 56.5 lh^{-1} shows a mismatch between the moving averages and experimental results, even for the time delay of 0.0025 s. This can be justified by the lack of points in laminar flow regime for the calibration curve or by the lack of sensitivity of the sensor for so small velocities. When converting measured tension to wall shear stress, a slight variation introduces higher differences than it should and wall shear stress is underestimated.

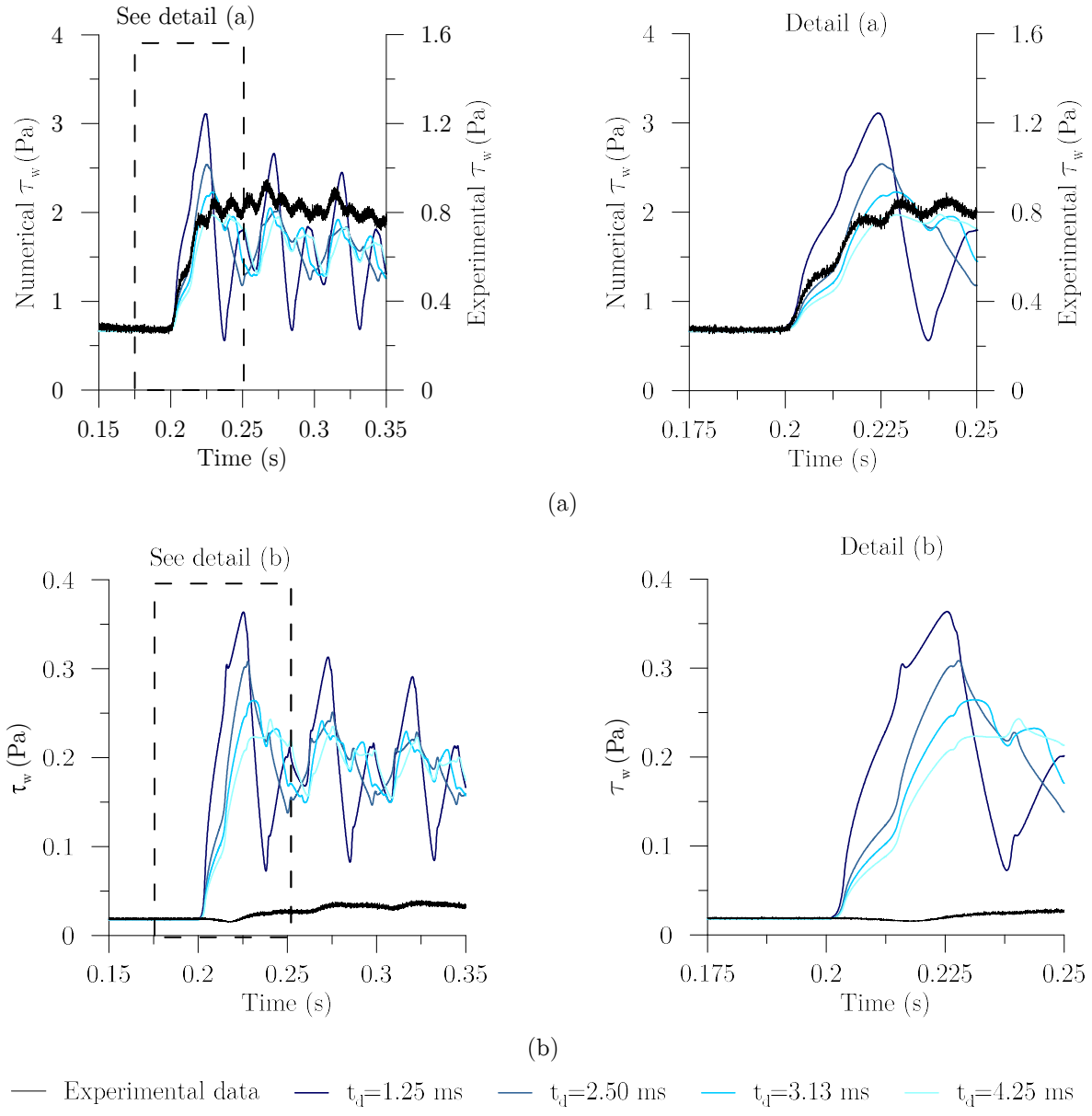

Figure 6.14. Experimental results with Zielke's moving average results for different time delays: (a) $Q_0 = 450$ lh^{-1} and (b) $Q_0 = 56.5$ lh^{-1}

6.5 Conclusions

Wall shear stress measurements were carried out in the experimental facility using a detailed and careful calibration approach as this measurement technique is based on heat transfer process. Steady-state flows are used to determine the calibration curve and a rough relation between the defined curve and experimental data is obtained.

Different numerical formulations are used for the calculation of the wall shear stress using the 1D model. Wall shear stresses obtained from the numerical model are compared with the ones experimentally obtained; major disagreements are observed not only in terms of extreme values (i.e., peaks during flow reversal could not be described), but also in terms of phase (a delay between pressure and wall shear stress is observed) and shape of variations (much smoother and gradual in the measurements). These discrepancies can be due to three main reasons. The first is the calibration curve that is highly sensitive to temperature variations and may have uncertainties associated with viscosity. The second is the position of the hot-film in relation to the pipe wall; ideally, it should be glued at the face of wall without creating any roughness; it was observed that the sensor was installed in the viscous sub-layer but not perfectly aligned with the pipe wall. These two reasons may justify the extreme values' differences and the signal shape, for measurements with high discrepancy from the numerical model. The latter is associated to the MiniCTA heating frequency that does not allow an accurate transient event characterization due to a delay of 2.5 ms (0.0025 s) in the electric system and equipment response. The technology used to measure unsteady wall shear stress method is not considered adequate for this kind of measurements, given the observed uncertainties (sensor location and calibration), physical reasons (system assembly and sensors' wires delicacy) and the frequency of response of the measuring equipment (MiniCTA).

Chapter 7 | Conclusions and recommendations

7.1 Summary and main conclusions

The current thesis aims to contribute to a better understanding on hydraulic transient events by using 1D numerical models. An extensive experimental data collection has been carried out and a 1D numerical model has been developed. The valve behaviour is characterized according to the orifice equation. The implemented numerical model consists of a 'reservoir-pipe-valve' system incorporating the main unsteady friction formulations developed for 1D models. Wall shear stress measurements have been carried out to assess friction evolution during water hammer events. Several results have been achieved: (i) the characterization of the spherical valve behaviour both in static and dynamic conditions; (ii) the development of a numerical model for a better understanding of water hammer events and the physical phenomenon associated with flow energy dissipation; and (iii) the wall shear stress measurements using temperature anemometry. The main conclusions from this research are:

Valve behaviour | The valve static behaviour is characterized by the flow rate variation and by the head loss coefficients for each percentage of closure. These parameters are Reynolds dependent as the viscous forces are predominant in laminar and transitional flows and inertial forces in turbulent flows, which significantly influence the valve behaviour for closures smaller than 83%. Valve dynamic behaviour is determined using two approaches for different closure times. The first considers the valve as an in-line valve. A flow rate discrepancy between the static and the dynamic behaviour is observed at higher closure angles due to the abrupt manoeuvres. The second approach idealizes a discharge to atmosphere considering only the pressure upstream the valve, which allows neglecting the pipe system at downstream the valve in the numerical model. To determine if the valve closure changes with the system configuration, a CFD model with different pipe lengths have shown that sustain that the type of manoeuvre (either fast or slow) strongly influences the valve closure law and low rate variation. Spherical valve effective closure time varies between 4 to 10% of the total closure time.

One-dimensional models | A 1D numerical model with different unsteady friction formulations was implemented, calibrated and compared with experimental data from the carried out transient events. A good fitting is obtained for both instantaneous acceleration-based and convolution-based models for turbulent flow measurements. Instantaneous acceleration-based do not accurately describe laminar flow. Convolution-based models describe reasonably well the pressure wave behaviour. A time dependent analysis was carried out and a pressure wave shift is obtained for the higher time-steps considered.

Wall shear stress | Wall shear stress measurements were carried out using a hot-film probe and constant temperature anemometry (CTA) measurement technique. Collected tension was subject of a calibration stage using the Blasius friction approach. The obtained wall shear stress after calibration was compared with numerical results and major discrepancies were observed in terms of extreme values, phase and shape. Observed discrepancies can be due to: (i) the calibration curve that is highly sensitive to temperature variations and the amount of tested flow rates; (ii) the position of the hot-film in relation to the pipe wall, which may not be accurately installed in the viscous sub-layer; and (iii) the MiniCTA heating frequency response to transient events with a time delay of 0.0025 s.

7.2 Recommendations for future work

The current research allowed the understanding of water hammer phenomenon and the spherical valve behaviour. However, several issues have arisen during the development of the research and recommendations are made for further research on the studied phenomena.

Valve behaviour | The valve characteristic curves (static and dynamic) depend on the valve type, the body size, the experimental conditions, the flow regime and the effective closure time. Other valve types and sizes could be tested, and the respective characteristic curves and effective closure times obtained. Another problem that has arisen was the pressure transducer accuracy range. Pressure transducers of lower nominal pressure should be used to determine more accurately the static behaviour of the valve. Thus, the uncertainties at lower closure angles would be smaller than the ones observed.

Hydraulic transient model | 1D numerical results only fit with experimental data, if the valve closure law is a priori known or is calibrated based on pressure-head measurements. An optimization algorithm could be developed for automatically carrying out the calibration process. Fluid-structure interaction (FSI) could also be analysed and complemented with unsteady friction models to characterize pressure oscillations in the pressure wave.

Wall shear stress | Wall shear stress measurements still have to overcome major challenges, namely better determining the calibration curve for pressurised pipe flows, measuring the shear stress at wall surface and correcting the time delay of the constant temperature anemometry acquisition system. Other indirect and non-intrusive measurement techniques, like the ones used by Brunone and Berni (2010) and Brito *et al.* (2014), based on the measurement of the velocity field (such as PIV), should be tested.

References

Abreu, J. and Almeida, A. B. (2009) Timescale Behavior of the Wall Shear Stress in Unsteady Laminar Pipe Flows. Journal of Hydraulic Engineering 135 415-424. DOI 10.1061/(ASCE)HY.1943-7900.0000024.

Admiraal, D. M. (1997) Hot-film shear stress measurements in laminar and turbulent flows. in IAHR 27th Congress, San Francisco.

Allievi, L. (1902) Theory of Water-Hammer. translated by E. Halmos (1925) Typography Riccardo Garroni.

Almeida, A. B. and Koelle, E. (1992) Fluid transients in pipe networks, ISBN: 1562520962.

Ariyaratne, C., Wang, F., He, S. and Vardy, A. E. (2010) Use of hot-film anemometry for wall

shear stress measurements in unsteady flow. in International Heat Transfer Conference, Washington DC.

Axworthy, D. H. and Ghidaoui, M. S. (2000) Extended thermodynamics derivation of energy dissipation in unsteady pipe flow. Journal of Hydraulic Engineering 126 276-287. DOI 10.1061/(ASCE)0733-9429(2000)126:4(276).

Berca, E.-L. (2007), Instrumentation development for wall shear-stress applications in 3D complex flows, PhD. Thesis. École Polytechnique Fédérale de Lausanne, Section de génie mécanique.

Bergant, A., Simpson, A. and Vitkovsk, J. (2001) Developments in unsteady pipe flow friction modelling. Journal of Hydraulic Research 39 249-257. DOI 10.1080/00221680109499828.

Bergant, A., Simpson, A. R. and Tijsseling, A. S. (2006) Water hammer with column separation: A historical review. Journal of Fluids and Structures 22 135-171. DOI 10.1016/j.jfluidstructs.2005.08.008.

Blasius, H. (1913) Das Aehnlichkeitsgesetz bei Reibungsvorgangen in Flussigkeiten, Mitteilungen über Forschungsarbeiten auf dem Gebiete des Ingenieurwesens: insbesondere aus den Laboratorien der technischen Hochschulen, Berlin, Heidelberg.

Bradshaw, P. and Gregory, N. (1959) The determination of local turbulent skin friction from observations in the viscous sub-layer.

Bratland, O. (1986) Frequency-Dependent Friction and Radial Kinetic Energy Variation in Transient

Pipe Flow. in 5th International Conference on Pressure Surges, Hannover, Germany.

Brito, M., Sanches, P., Ferreira, R. M. and Covas, D. I. C. (2014) PIV Characterization of Transient Flow in Pipe Coils. Procedia Engineering 89 1358 - 1365. DOI 10.1016/j.proeng.2014.11.458.

Brunone, B. (1999) Transient Test-Based Technique for Leak Detection in Outfall Pipes. Journal of Water Resources Planning and Management 125 302-306. doi:10.1061/(ASCE)0733-9496(1999)125:5(302).

Brunone, B. and Berni, A. (2010) Wall shear stress in transient turbulent pipe flow by local velocity measurement. Journal of Hydraulic Engineering 136 716-725. DOI 10.1061/(ASCE)Hy.1943-7900.0000234.

Brunone, B., Ferrante, M., Meniconi, S. and Massari, C. (2013) Effectiveness Assessment of Pipe Systems by Means of Transient Test-based Techniques. Procedia Environmental Sciences 19 814-822. 10.1016/j.proenv.2013.06.090.

Brunone, B., Golia, U. M. and Greco, M. (1991a) Some remarks on the momentum equation for fast transients. in International Meeting on Hydraulic Transients and Water Column Separation, Universidad Politecnica de Valencia.

Brunone, B., Golia, U. M. and Greco, M. (1991b) Some remarks on the momentum equation for fast transients b). in International Meeting on Hydraulic Transients and Water Column Separation, Universidad Politecnica de Valencia.

Cardoso, A. H. (1998) Hidráulica Fluvial, Gulbenkian, F. C. ISBN: 9723108151. Lisboa, Portugal

Carriço, N. J. G., Soares, A. K. and Covas, D. I. C. (2016) Uncertainties of inverse transient modelling with unsteady friction and pipe-wall viscoelasticity. Journal of Water Supply: Research and Technology - Aqua 65 342-353. DOI 10.2166/aqua.2016.075.

Carstens, M. R. a. R., J. E. (1959) Boundary-shear Stress in Unsteady Turbulent Pipe Flow. Journal of Hydraulic Divison 95 67-81.

Chaudhry, M. H. (2014) Applied Hydraulic Transients, ISBN: 978-1-4614-8537-7.

Chaudhry, M. H. and Hussaini, M. Y. (1985) Second-order accurate explicit finite-difference schemes for waterhammer analysis. Journal of Fluids Engineering 107 523-529. DOI 10.1115/1.3242524.

Covas, D. (2003), Inverse transient analysis for leak detetion and calibration of water pipe systems modelling special dynamic effects, PhD. Thesis. Imperial College of Science, Technology and Medicine, Department of Civil and Environmental Engineering.

Covas, D. and Ramos, H. (2001) Hydraulic transients used for leakage detection in water distribution systems. in Proc. Intl. Conf. Water Pipelyne Systems York UK.

Covas, D. and Ramos, H. (1999) Pratical methods for leakage control, detection, and location in pressurized systems. in BHR CONFERENCE SERIES PUBLICATION,

Covas, D., Ramos, H. and Almeida, A. B. d. (2005a) Standing Wave Difference Method for Leak Detection in Pipeline Systems. Journal of Hydraulic Engineering 131 1106-1116. DOI 10.1061/(ASCE)0733-9429(2005)131:12(1106).

Covas, D., Stoianov, I., Ramos, H. and Graham, N. (2005b) The dynamic effect of pipe-wall viscoelasticity in hydraulic transients. Part I—Experimental analysis and creep characterization. Journal of Hydraulic Research 42 517-532. DOI 10.1080/00221686.2004.9641221.

Daily, J. W., Jr, H. W. L., Olive, R. W. and Jr, J. J. M. (1956) Resistance coefficients for accelerated and decelerated flows through smooth tubes and orifices.

Day, M. A. (1990) The no-slip condition of fluid dynamics. Erkenntnis 33 285-296. DOI 10.1007/bf00717588.

Dickenson, T. C. (1999) Valves, Piping, and Pipelines Handbook, ISBN: 9781856172523. Oxford ; New York

Duan, H.-F., Lee, P. J., Kashima, A., Lu, J., Ghidaoui, M. S. and Tung, Y.-K. (2013) Extended Blockage Detection in Pipes Using the System Frequency Response: Analytical Analysis and Experimental Verification. Journal of Hydraulic Engineering 139 763-771. doi:10.1061/(ASCE)HY.1943-7900.0000736.

Ferrante, M. and Brunone, B. (2003) Pipe system diagnosis and leak detection by unsteady-state tests. 1. Harmonic analysis. Advances in Water Resources 26 95-105. 10.1016/S0309-1708(02)00101-X.

Ferrante, M., Massari, C., Todini, E., Brunone, B. and Meniconi, S. (2013) Experimental investigation of leak hydraulics. Journal of Hydroinformatics 15 666-675. 10.2166/hydro.2012.034.

Ferràs, D., Manso, P. A., Schleiss, A. J. and Covas, D. I. C. (2016) Experimental distinction of damping mechanisms during hydraulic transients in pipe flow. Journal of Fluids and Structures 66 424-446. DOI 10.1016/j.jfluidstructs.2016.06.009.

Garrison, T. J., Manceau, E. and Nikitopoulos, D. E. (1998) Skin Friction Measurements in a Gas-Liquid Pipe Flow Via Optical Interferometry. Journal of Fluids Engineering 120 303. DOI 10.1115/1.2820649.

Ghidaoui, M. S. and Mansour, S. (2002) Efficient treatment of the Vardy-Brown unsteady shear in pipe transients. Journal of Hydraulic Engineering 128 102-112. DOI 10.1061/(ASCE)0733-9429(2002)128:1(102)

Ghidaoui, M. S. and Zhao, M. (2005) A review of water hammer theory and practice. Applied Mechanics Reviews 58 49-76. DOI 10.1115/1.1828050.

He, S., Ariyaratne, C. and Vardy, A. E. (2011) Wall shear stress in accelerating turbulent pipe flow. Journal of Fluid Mechanics 685 440-460. DOI 10.1017/jfm.2011.328.

Holloway, M. B. and Chaudhry, M. H. (1985) Stability and Accuracy of Waterhammer Analysis. Advances in Water Resources 8 121-128. DOI Doi 10.1016/0309-1708(85)90052-1.

Holmboe, E. L. and Rouleau, W. T. (1967) The Effect of Viscous Shear on Transients in Liquid Lines. Journal of basic engineering 89 174-180. DOI 10.1115/1.3609549.

Idel′chik, I. E. and Steinberg, M. O. (1996) Handbook of Hydraulic Resistance, ISBN: 9781567000740.

Joukowsky, N. (1900) Über den hydraulischen Stoss in Wasserleitungsröhren, Mémoires de l'Académie Impériale des Sciences de St.-Pétersbourg

Kagawa, T., Lee, I., Kitagawa, A. and Takenaka, T. (1983) High Speed and Accurate Computing Method of Frequency-Dependent Friction in Laminar Pipe Flow for Characteristics Method. Transactions of the Japanese Society of Mechanical Engineers 49 2638-2644.

Keller, R. and Wilkinson, S. (2002) Construction, Calibration and Use of Flush Mounted Wall Shear Stress Probes. in Hydraulic Measurements and Experimental Methods, Estes Park, Colorado, USA.

Klewicki, J. C. and Falco, R. E. (2006) On accurately measuring statistics associated with small-scale structure in turbulent boundary layers using hot-wire probes. Journal of Fluid Mechanics 219 119-142. DOI 10.1017/S0022112090002889.

Lee, P. J., Duan, H.-F., Tuck, J. and Ghidaoui, M. (2015) Numerical and Experimental Study on the Effect of Signal Bandwidth on Pipe Assessment Using Fluid Transients. Journal of Hydraulic Engineering 141 04014074. doi:10.1061/(ASCE)HY.1943-7900.0000961.

Lescovich, J. E. (1967) The control of water hammer by automatic valves. American Water Works Association 59 632-644. DOI 41265218

Leslie, D. J. and Tijsseling, A. S. (2000) Travelling discontinuities in waterhammer theory. in Pressure Surge, The Hague, The Netherlands.

Martins, N. (2016), Transient flow dynamics in pressurized pipes: CFD modelling and experimental analysis, PhD Thesis. Instituto Superior Técnico, DECivil.

Martins, N., Carriço, N., Ramos, H. and Covas, D. (2014) Velocity-distribution in pressurized pipe flow using CFD: Accuracy and mesh analysis. Computers & Fluids 105 218-230. DOI 10.1016/j.compfluid.2014.09.031.

Martins, N., Soares, A., Ramos, H. and Covas, D. (2016) CFD modeling of transient flow in pressurized pipes. Computers & Fluids 126 129-140. DOI 10.1016/j.compfluid.2015.12.002.

Massari, C., Yeh, T. C. J., Ferrante, M., Brunone, B. and Meniconi, S. (2014) Detection and sizing of extended partial blockages in pipelines by means of a stochastic successive linear estimator. Journal of Hydroinformatics 16 248-258. 10.2166/hydro.2013.172.

Menabrea, L. F. (1858) Note sur les effets du choc de l'eau dans les conduites,

Menendez, A. N. and Ramaprian, B. R. (1985) The use of flush-mounted hot-film gauges to measure skin friction in unsteady boundary layers. Journal of Fluid Mechanics 161 139-159. DOI 10.1017/S0022112085002853.

Michaud, J. (1878) Coups de belier dans les conduites: etude des moyens employes pour en attenuer les effets. 4 55-64, 65-77.

Miller, D. S. (1990) Internal Flow Systems, ISBN: 9780947711771.

Parmakian, J. (1955) Waterhammer analysis, 9780486610610.

Ramos, H., Almeida, A., Portela, M. and Almeida, H. P. (2000) Guidelines for design of small hydropower plants. WREAN and DED, Belfast, North Ireland

Ramos, H., Covas, D., Borga, A. and Loureiro, D. (2004) Surge damping analysis in pipe systems: modelling and experiments. Journal of Hydraulic Research 42 413-425. DOI 10.1080/00221686.2004.9641209.

Riedelmeier, A., Becker, S. and Schlücker, E. (2014) 3D CFD Simulation of Water Hammer Through a 90° Bend: Applicability of URANS, 3D Effects and Unsteady Friction. in ASME 2014 Pressure Vessels and Piping Conference, Anaheim, California, USA.

Schlichting, H. (1979) Boundary-layer theory, ISBN: 978-3-540-66270-9.

Shuy, E. B. (1996) Wall shear stress in accelerating and decelerating turbulent pipe flows. Journal of Hydraulic Research 34 173-183. DOI 10.1080/00221689609498495.

Soares, A. K., Covas, D. I. C. and Ramos, H. M. (2013) Damping Analysis of Hydraulic Transients in Pump-Rising Main Systems. Journal of Hydraulic Engineering 139 233-243. DOI 10.1061/(ASCE)HY.1943-7900.0000663.

Stephens, M. L., Lambert, M. F. and Simpson, A. R. (2013) Determining the Internal Wall Condition of a Water Pipeline in the Field Using an Inverse Transient. Journal of Hydraulic Engineering 139 310-324. doi:10.1061/(ASCE)HY.1943-7900.0000665.

Suo, L. and Wylie, E. B. (1990) Complex Wavespeed and Hydraulic Transients in Viscoelastic Pipes. Journal of Fluids Engineering 112 496. DOI 10.1115/1.2909434.

Suzuki, K., Taketomi, T. and Sato, S. (1991) Improving Zielke's Method of Simulating Frequency-Dependent Friction in Laminar Liquid Pipe Flow. Journal of Fluids Engineering 113 569. DOI 10.1115/1.2926516.

Tanner, L. H. (1979) Skin friction measurement by viscosity balance in air and water flows. Journal of Physics E: Scientific Instruments 12 610. DOI 10.1088/0022-3735/12/7/015.

Tian, X., Zhang, S. X.-Y., Valade, M. and Young, P. (2013) Head Loss through Pipe Fittings for Laminar Flows. Pipelines 2013 301-308. 10.1061/9780784413012.028.

Trikha, A. K. (1975) An Efficient Method for Simulating Frequency-Dependent Friction in Transient Liquid Flow. Journal of Fluids Engineering 97 DOI 10.1115/1.3447224.

Tropea, C., Yarin, A. L. and Foss, J. F. (2007) Springer Handbook of Experimental Fluid Mechanics, ISBN: 9783540251415.

Tsinober, A. (2009) An Informal Conceptual Introduction to Turbulence: Second Edition of An Informal Introduction to Turbulence, ISBN: 9789048131747.

Tuck, J. and Lee, P. (2013) Inverse Transient Analysis for Classification of Wall Thickness Variations in Pipelines. Sensors (Basel, Switzerland) 13 17057-17066. DOI 10.3390/s131217057.

Tullis, J. P. (1989) Hydraulics of Pipelines: Pumps, Valves, Cavitation, Transients, ISBN: 9780471832850.

Vardy, A. E. and Brown, J. M. B. (2004) Efficient approximation of unsteady friction weighting functions. Journal of Hydraulic Engineering DOI 10.1061/(ASCE)0733-9429(2004)130%3A11(1097).

Vardy, A. E. and Brown, J. M. B. (1996) On Turbulent, Unsteady, Smooth-Pipe Friction. in Pressure Surge and Fluid Transients, Harrogate, United Kingdom.

Vardy, A. E. and Brown, J. M. B. (2003) Transient turbulent friction in smooth pipe flows. Journal of Sound and Vibration 259 1011-1036. DOI 10.1006/jsvi.2002.5160.

Vardy, A. E. and Brown, J. M. B. (1995) Transient, turbulent, smooth pipe friction. J Hydraul Res 33 435-456. DOI 10.1080/00221689509498654.

Vardy, A. E., Brown, J. M. B. and Hwang, K.-L. (1993) A weighting function model of transient turbulent pipe friction. J Hydraul Res 31 533-548. DOI 10.1080/00221689309498876.

Vitkovsky, J., Stephens, M., Bergant, A., Lambert, M. and Simpson, A. (2004) Efficient and accurate calculation of Zielke and Vardy-Brown unsteady friction in pipe transients. in Proceedings of the 9th International Conference on Pressure Surges, Chester, United Kingdom.

Wahba, E. M. (2008) Modelling the attenuation of laminar fluid transients in piping systems. Applied Mathematical Modelling 32 2863 - 2871. DOI 10.1016/j.apm.2007.10.004.

Wang, H., Zhou, L., Liu, D., Karney, B., Wang, P., Xia, L., Ma, J. and Xu, C. (2016) CFD Approach for Column Separation in Water Pipelines. Journal of Hydraulic Engineering 142 04016036. DOI doi:10.1061/(ASCE)HY.1943-7900.0001171.

White, F. M. (2010) A Brief Introduction To Fluid Mechanics, ISBN: 9780470596791.

Wu, D., Yang, S., Wu, P. and Wang, L. (2015) MOC-CFD Coupled Approach for the Analysis of the Fluid Dynamic Interaction between Water Hammer and Pump. Journal of Hydraulic Engineering 141 06015003. DOI 10.1061/(ASCE)HY.1943-7900.0001008.

Wylie, E. B., Streeter, V. L. and Suo, L. (1993) Fluid transients in systems, ISBN: 9780133221732.

Yang, S., Wu, D., Lai, Z. and Du, T. (2016) Three-dimensional computational fluid dynamics simulation of valve-induced water hammer. ARCHIVE Proceedings of the Institution of Mechanical Engineers Part C Journal of Mechanical Engineering Science 1989-1996 DOI 10.1177/0954406216631780.

Zarzycki, Z., Kudzma, S. and Urbanowicz, K. (2011) Improved Method for Simulating Transients of Turbulent Pipe Flow. Journal of Theoretical and Applied Mechanics 49 135-158.

Zielke, W. (1968) Frequency-dependent friction in transient pipe flow. Journal of basic engineering 90 DOI 10.1115/1.3605049.

Appendices

Appendix A – Valve static behaviour data

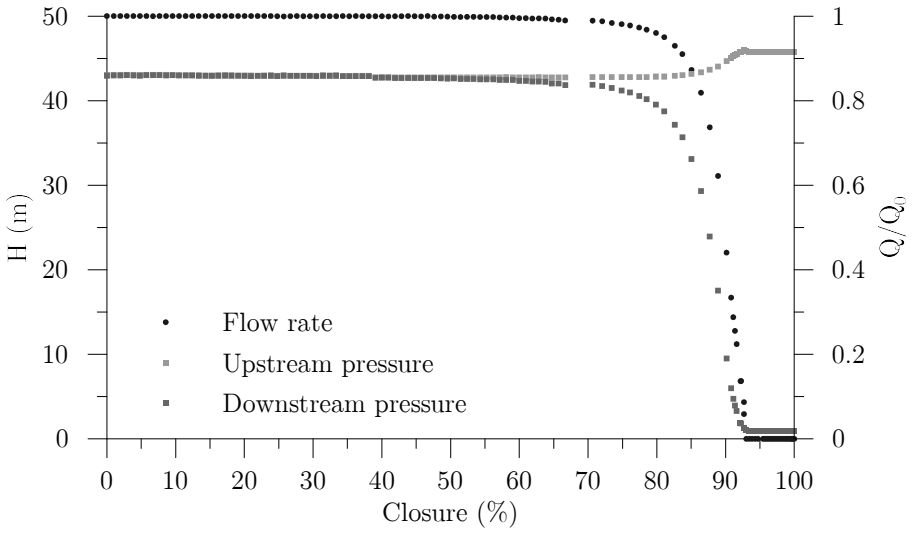

Figure A.1. Piezometric-head and flow rate variation with closure for static test S1

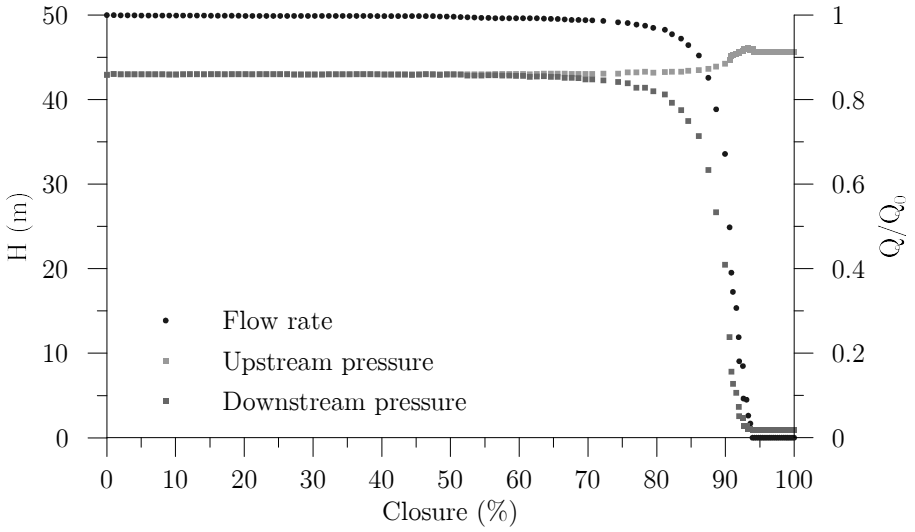

Figure A.2. Piezometric-head and flow rate variation with closure for static test S2

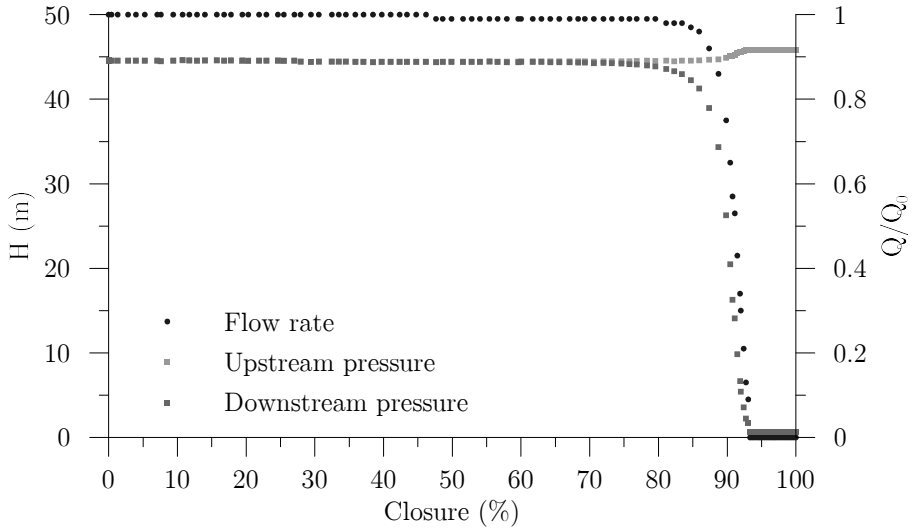

Figure A.3. Piezometric-head and flow rate variation with closure for static test S3

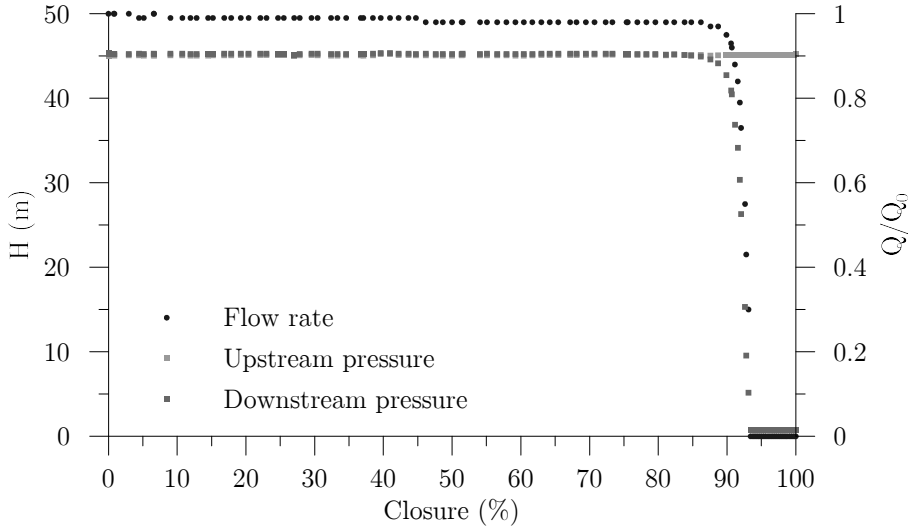

Figure A.4. Piezometric-head and flow rate variation with closure for static test S4

Appendix B – Valve dynamic behaviour data

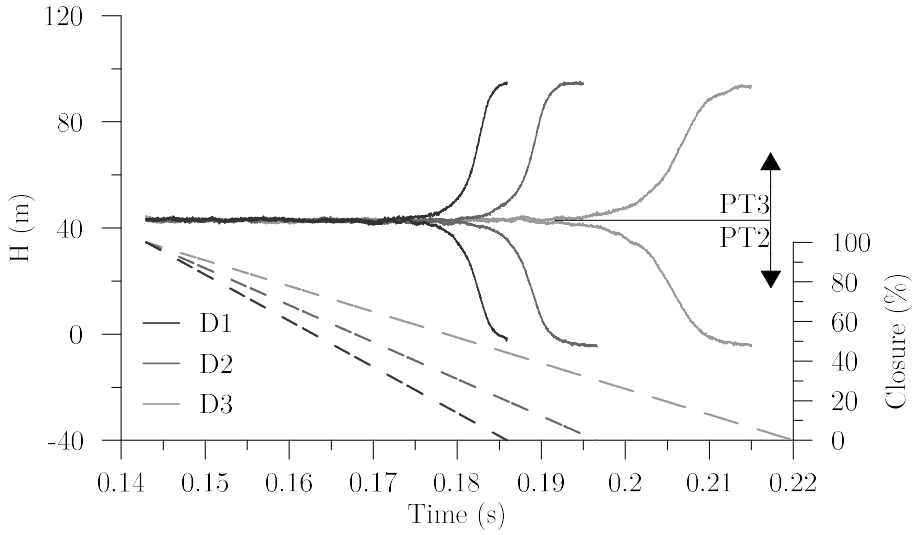

Figure B.1. Piezometric-head and flow rate variation with closure for dynamic test Q_0=450 lh^{-1}

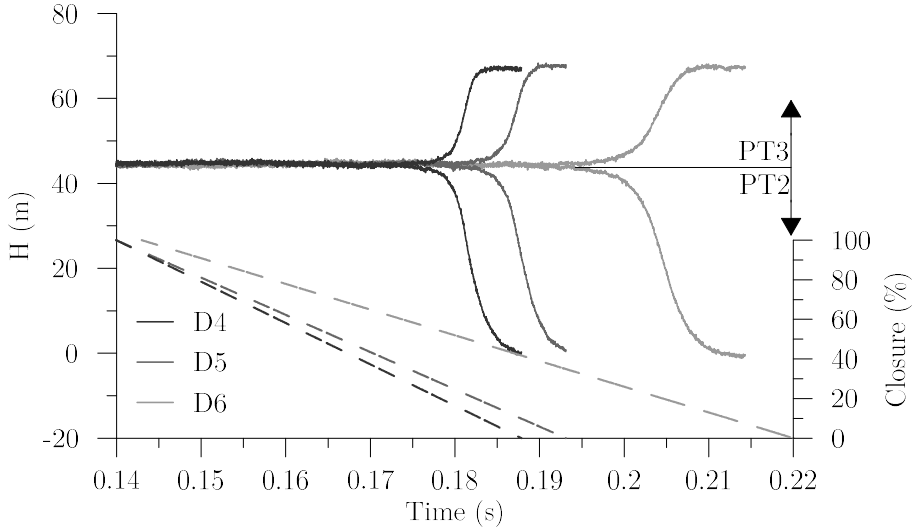

Figure B.2. Piezometric-head and flow rate variation with closure for dynamic test Q_0=200 lh^{-1}

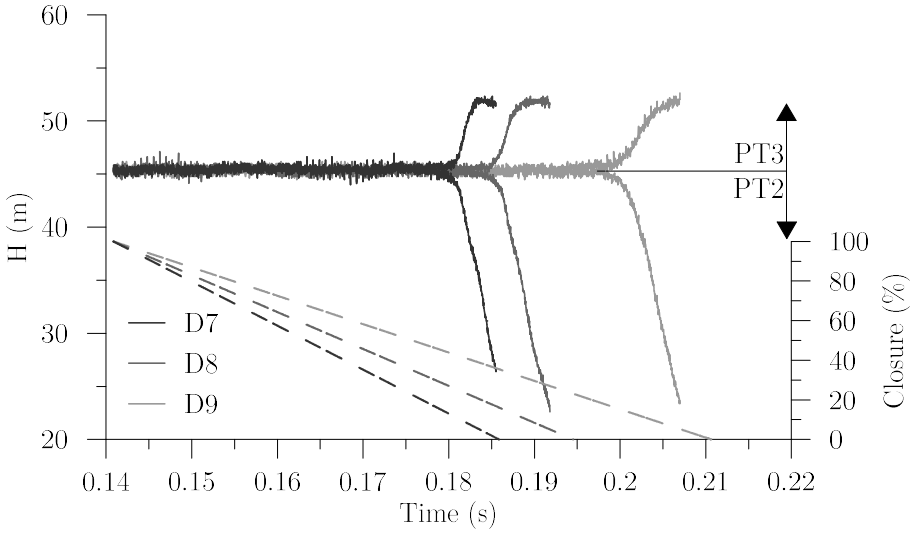

Figure B.3. Piezometric-head and flow rate variation with closure for dynamic test Q_0=56.5 lh^{-1}

Appendix C – Wall shear stress measurements

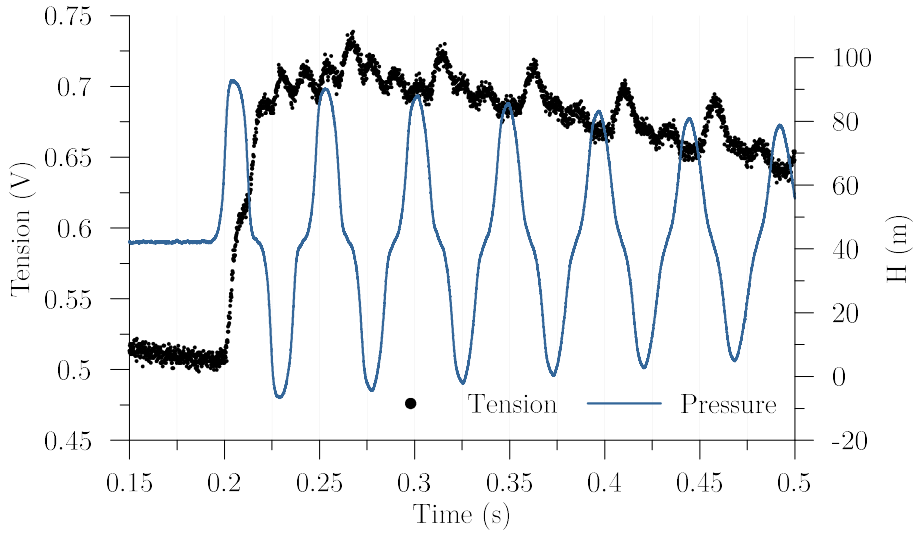

Figure C.1. Piezometric-head and MiniCTA tension variation at pipe mid-length for 450 lh^{-1} test

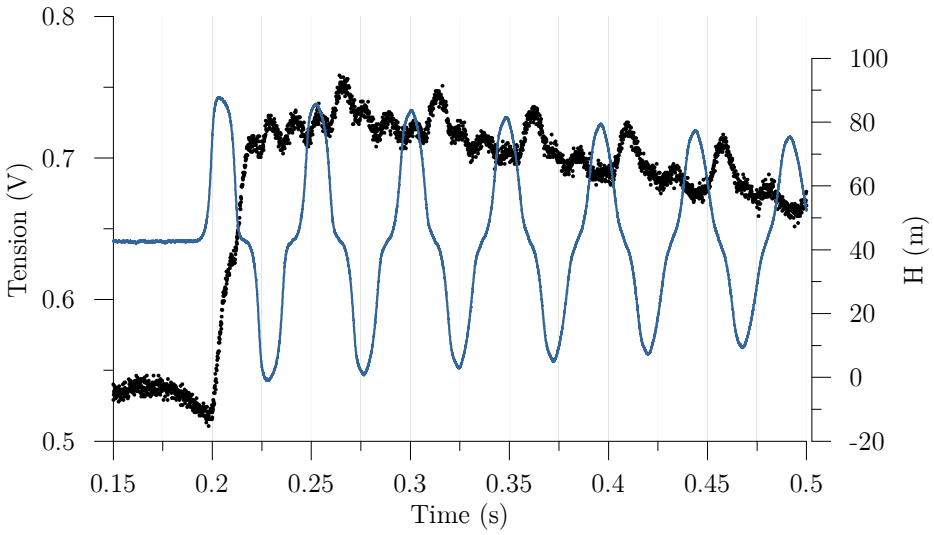

Figure C.2. Piezometric-head and MiniCTA tension variation at pipe mid-length for 400 lh^{-1} test

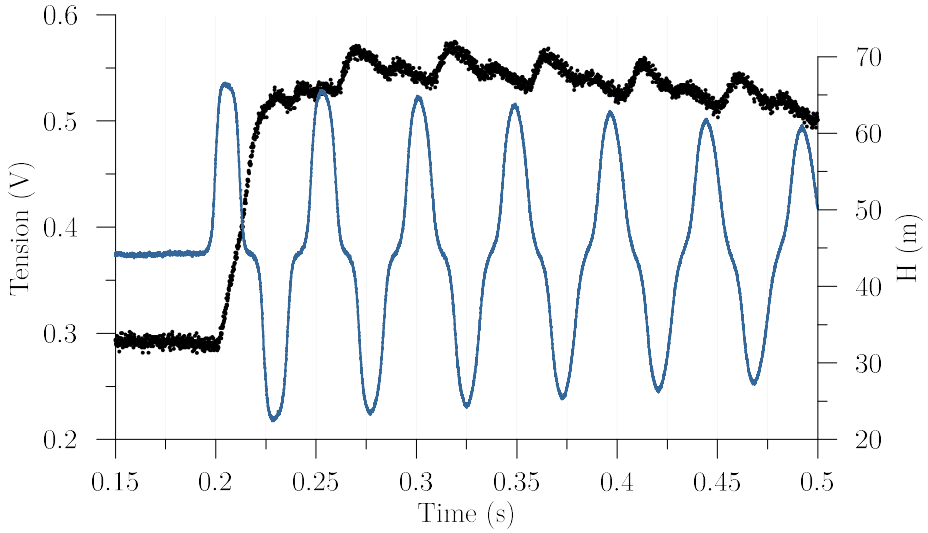

Figure C.3. Piezometric-head and MiniCTA tension variation at pipe mid-length for 200 lh^{-1} test

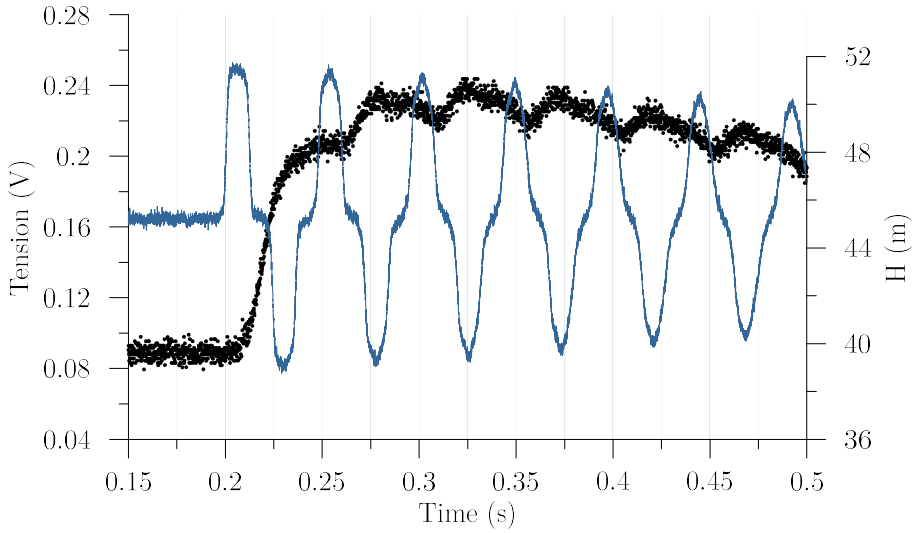

Figure C.4. Piezometric-head and MiniCTA tension variation at pipe mid-length for 56.5 lh^{-1} test